

126p

NASA CR 174676



**LARGE PERTURBATION FLOW FIELD ANALYSIS  
AND SIMULATION FOR SUPERSONIC INLETS  
FINAL REPORT**

(NASA-CR-174676) LARGE PERTURBATION FLOW  
FIELD ANALYSIS AND SIMULATION FOR SUPERSONIC  
INLETS Final Report (Sverdrup Technology,  
Inc.) 126 p CSCL 01A

N87-10835

G3/02 Unclas  
43832

by  
M. O. Varner, W. R. Martindale, W. J. Phares,  
K. R. Kneile, and J. C. Adams, Jr.

**SVERDRUP TECHNOLOGY, INC.**

Prepared for  
**NATIONAL AERONAUTICS AND SPACE ADMINISTRATION**  
Lewis Research Center

Contract NAS3-23682



Copy Number **27**



NASA CR 174676



**LARGE PERTURBATION FLOW FIELD ANALYSIS  
AND SIMULATION FOR SUPERSONIC INLETS**

**FINAL REPORT**

by  
M. O. Varner, W. R. Martindale, W. J. Phares,  
K. R. Kneile, and J. C. Adams, Jr.

**SVERDRUP TECHNOLOGY, INC.**

Prepared for  
**NATIONAL AERONAUTICS AND SPACE ADMINISTRATION**  
Lewis Research Center

Contract NAS3-23682

**LIMITED DISTRIBUTION**

This document will remain under distribution  
limitation until September 25, 1985

## FOREWORD

The Final Report contained in this document was prepared under contract NAS3-23682, "Large Perturbation Flow Field Analysis and Simulation for Supersonic Inlets." The work was conducted under the direction of Mr. Gary L. Cole who served as the NASA Project Manager and Mr. Joe F. Wasserbauer who served as the NASA Technical Advisor; Dr. John C. Adams, Jr., was the Project Manager at Sverdrup Technology, Inc.

## TABLE OF CONTENTS

Section	Page
1.0 SUMMARY . . . . .	1
2.0 INTRODUCTION . . . . .	3
3.0 ANALYSIS . . . . .	7
3.1 Governing Equations . . . . .	7
3.2 Nondimensional Governing Equations . . . . .	10
3.3 Coordinate Transformation . . . . .	12
3.4 Numerical Methods . . . . .	14
3.4.1 Beam-Warming Algorithm . . . . .	14
3.4.1.1 Implicit Solution Technique . . . . .	14
3.4.1.2 Boundary Point Technique . . . . .	16
3.4.1.3 Boundary Condition Constraints . . . . .	18
3.4.2 Beam-Warming Hybrid Algorithm . . . . .	21
3.4.3 Flux Vector Splitting Algorithm . . . . .	22
3.4.4 Split Characteristics Algorithm . . . . .	26
3.4.4.1 Characteristic Relations . . . . .	28
3.4.4.2 Explicit Split Characteristics . . . . .	29
3.4.4.3 Boundary Conditions . . . . .	32
3.4.4.4 Implicit Operator . . . . .	34
3.4.4.5 Algorithm Application . . . . .	37
3.5 Geometry . . . . .	38
3.6 Unstart Model . . . . .	40
3.7 Bleed and Bypass Model . . . . .	43
3.8 External Inviscid Flow Field . . . . .	47
3.9 Initial Conditions . . . . .	56
3.10 Computer Code (Program LAPIN) . . . . .	60
4.0 ALGORITHM VERIFICATION . . . . .	67
5.0 RESULTS AND DISCUSSION . . . . .	75
5.1 40-60 Inlet . . . . .	75
5.2 40-60 Inlet Steady-State Performance . . . . .	75
5.3 40-60 Inlet Hammershock Transient . . . . .	78
5.4 40-60 Inlet Unstart/Restart Transient . . . . .	81
5.5 40-60 Inlet Dynamic Response . . . . .	97
5.6 60-40 Inlet . . . . .	100
5.7 60-40 Inlet Steady-State Performance . . . . .	104
5.8 60-40 Inlet Transient Unstart Limits . . . . .	104
5.9 B-70 Inlet . . . . .	108
5.10 B-70 Inlet Steady-State Performance . . . . .	108
6.0 CONCLUDING REMARKS . . . . .	111

TABLE OF CONTENTS  
(concluded)

Appendix	Page
A Straight Sonic Line Correction Factor Derivation . . . .	113
B Symbols . . . . .	117

References

## 1.0 SUMMARY

An analysis technique for simulation of supersonic mixed-compression inlets with large flow field perturbations (hammershock, unstart/restart, etc.) is presented. The approach is based upon a quasi-one-dimensional inviscid unsteady formulation which includes engineering models of unstart/restart, bleed, bypass, and geometry effects. Numerical solution of the governing time-dependent equations of motion is accomplished through a shock-capturing finite-difference algorithm, of which five separate approaches are evaluated. Comparison with experimental supersonic wind tunnel data is presented to verify the present approach for a wide range of transient inlet flow conditions.

## 2.0 INTRODUCTION

The function of a supersonic inlet is to supply the airflow required by an engine at the highest possible pressure level while maintaining minimum drag. In order to minimize inlet cowl drag for sustained flight at speeds above Mach 2.0, it becomes essential that some portion of the supersonic area contraction be accomplished internally. An inlet of this type is commonly referred to as a mixed-compression inlet. For mixed-compression inlets, optimum internal performance is provided by maintaining the terminal shock at the inlet throat. This operation provides high-pressure recovery and minimizes distortion at the engine face. These inlets, however, have a discontinuous airflow characteristic known as unstart. If an airflow transient causes the terminal shock to move upstream from the throat, the shock is unstable and is abruptly expelled ahead of the cowling. This shock expulsion, or unstart, causes a sharp reduction in mass flow and pressure recovery and a large drag increase. Inlet buzz, compressor stall, and/or combustor blowout may also occur. Obviously, an inlet unstart is extremely undesirable because of the adverse effects not only on the propulsion system itself but also on the aerodynamic qualities of the aircraft. If inlet unstart does occur, complex mechanical variations to alter the inlet geometry are required to restart the inlet and stabilize the normal shock at a position downstream of the throat.

Prior modeling efforts of supersonic inlet gas-dynamic phenomena have concentrated on a control volume or lumped-parameter approach following the original work of Martin (Ref. 1). This type of simulation is basically a one-dimensional mathematical model (involving ordinary differential equations) for predicting the transient behavior (dynamic response) of the subsonic duct downstream of the terminal normal shock, with the subsonic duct divided into a number of lumped volumes. Models that treat the whole subsonic duct as a single lumped volume may be sufficiently accurate for fairly short air induction systems, but their accuracy deteriorates for inlets which are long. For such long air induction systems, it becomes necessary to divide the subsonic duct into more than one lumped volume. Although simulation accuracy increases with increasing number of volume lumps used, practical considerations limit this number to three or four.

The supersonic inlet investigation by Amin and Hall (Ref. 2) divided the subsonic duct volume into three initially equal volumes. The volume nearest to the throat had a moving upstream boundary (the normal shock) and a fixed downstream boundary; the remaining two lumped volumes had fixed boundaries. The instantaneous total temperature and total pressure within each of these volumes were obtained during a simulation run by numerically integrating the corresponding rate equations. These rate equations were derived by applying the one-dimensional unsteady continuity and energy equations in conjunction with the equation of state to each lumped volume. Complete derivation of these equations is given in Appendix 1 of Ref. 2. To calculate the rate of change of mass flow at each of the lumped volume boundaries, the rate of change of momentum within each volume due to the instantaneous net imbalanced force acting on it during transient conditions was utilized. Complete derivation of the mass flow rate equations is given in Appendix II of Ref. 2. For the case of inlet unstart, the continuity method by Moeckel (Ref. 3) was used to calculate the expelled shock position ahead of the inlet cowl and the relationship between this shock position and the resultant subsonic flow spillage over the inlet cowl.

A linearized characteristics type of analysis has been developed by Willoh (Ref. 4) for dynamic response studies of one-dimensional inviscid inlet flows. This approach combines a set of linearized equations across the normal shock with an exact solution of the linearized wave equation. In general, the Willoh analysis is more exact than conventional lumped-parameter techniques and, for many problems, is no more complicated in application. However, it is based upon a linearized treatment and hence is strictly applicable only to inlet flows with small flow-field perturbations. Results presented in Refs. 5 and 6 show reasonable agreement with experiment for mixed-compression inlet frequency response (amplitude ratio and phase angle) at a free-stream Mach number of approximately 2.5.

The work by Mays (Ref. 7) was one of the first to employ a completely numerical solution of the one-dimensional, unsteady, inviscid flow equations in a variable area duct. His numerical technique was based upon the Lax artificial viscosity explicit algorithm. Through this



approach, large amplitude transients (such as compressor surge) and their effect on mixed-compression inlet flow could be numerically simulated. The main difficulty with this approach is the use of the Lax algorithm which is well-known to introduce spurious second-order dissipative (viscous-like) terms into the governing equations. However, for the time in which this work was performed (1968), the Lax algorithm was the best numerical technique available.

The present report will document an analytical investigation into simulation of large perturbation flow field effects (such as hammer-shock, unstart/restart, etc.) in mixed-compression supersonic inlets. A quasi-one-dimensional inviscid unsteady approach will be described which includes engineering models of unstart/restart, bleed, bypass, and geometry effects. Numerical solution of the governing time-dependent equations of motion will be accomplished through a shock-capturing finite-difference algorithm, of which five separate approaches are evaluated. Comparison with experimental supersonic wind tunnel data will be presented to verify the present approach for a wide range of transient inlet flow conditions.

The following advisory panel provided high-level technical expertise and guidance during the course of the present work.

Name	Affiliation	Area
Mr. G. L. Cole	NASA/LeRC	Inlet Engineering
Mr. J. P. Hartin	Sverdrup Technology, Inc.	Inlet Engineering
Dr. W. F. Kimzey	Sverdrup Technology, Inc.	Inlet Modeling
Prof. R. W. MacCormack	Univ. of Washington	Computational Fluid Dynamics
Mr. J. F. Wasserbauer	NASA/LeRC	Inlet Engineering
Dr. D. L. Whitfield	Mississippi State Univ.	Computational Fluid Dynamics

### 3.0 ANALYSIS

An illustration of an axisymmetric mixed-compression supersonic inlet is presented in Fig. 1. Pertinent details which will be modeled by the present work include:

- cowl bleed and bypass
- ▲ centerbody bleed
- centerbody translation
- supersonic inviscid flow field between the tip and the inlet plane
- variable boundary conditions at the exit plane

The x- and y-axis will be taken as shown (along and normal to the centerline of the centerbody, respectively).

#### 3.1 GOVERNING EQUATIONS

If the cross-sectional area of a flow passage varies very slowly and the radius of curvature of the central axis of the passage is large contrasted to the passage height, the flow inside the passage is said to be a quasi-one-dimensional flow. In this case, the flow area  $\tilde{A}$  is a function of both distance  $\tilde{x}$  and time  $\tilde{t}$ . The flow properties are assumed to be uniform across all surfaces perpendicular to the mean flow direction. Figure 2 illustrates the quasi-one-dimensional flow model for unsteady inviscid flow with friction  $\tilde{F}_f$ , heat transfer  $\tilde{Q}$ , and mass bleed  $\tilde{m}_i$ .

The derivation of the appropriate governing fluid dynamic equations of motion (continuity, momentum, and energy) may be found in most compressible fluid flow textbooks, for example, Chapter 24 of Shapiro (Ref. 8) and Chapter 19 of Zucrow and Hoffmann (Ref. 9). These equations are (with reference to Fig. 2 for nomenclature):

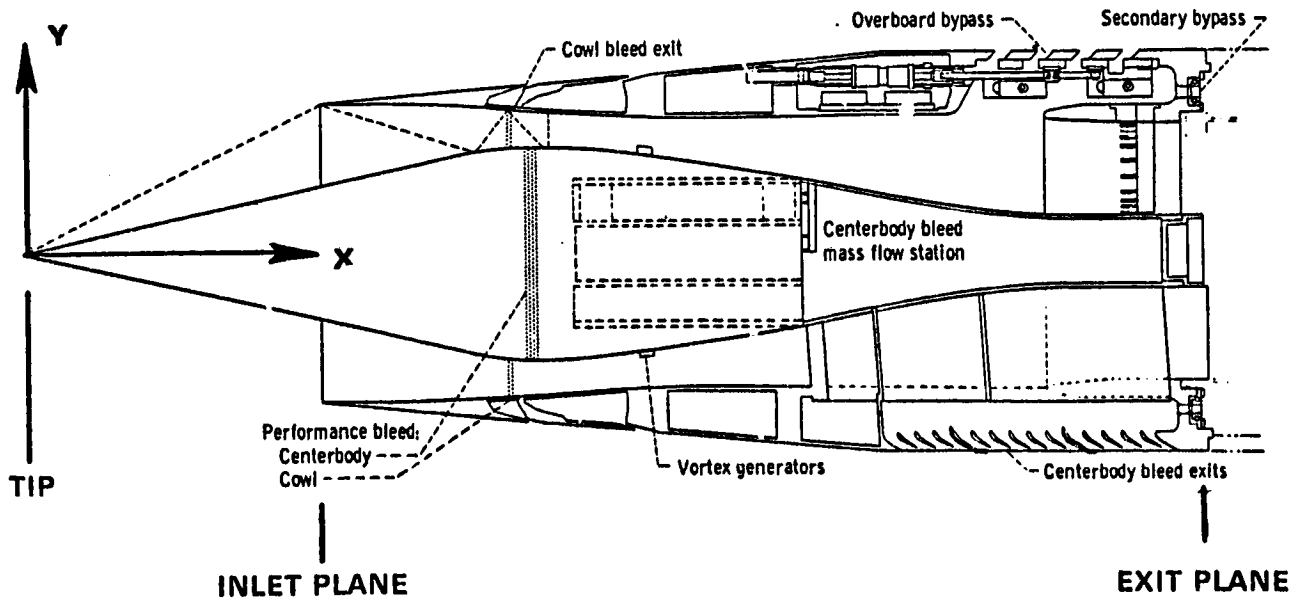
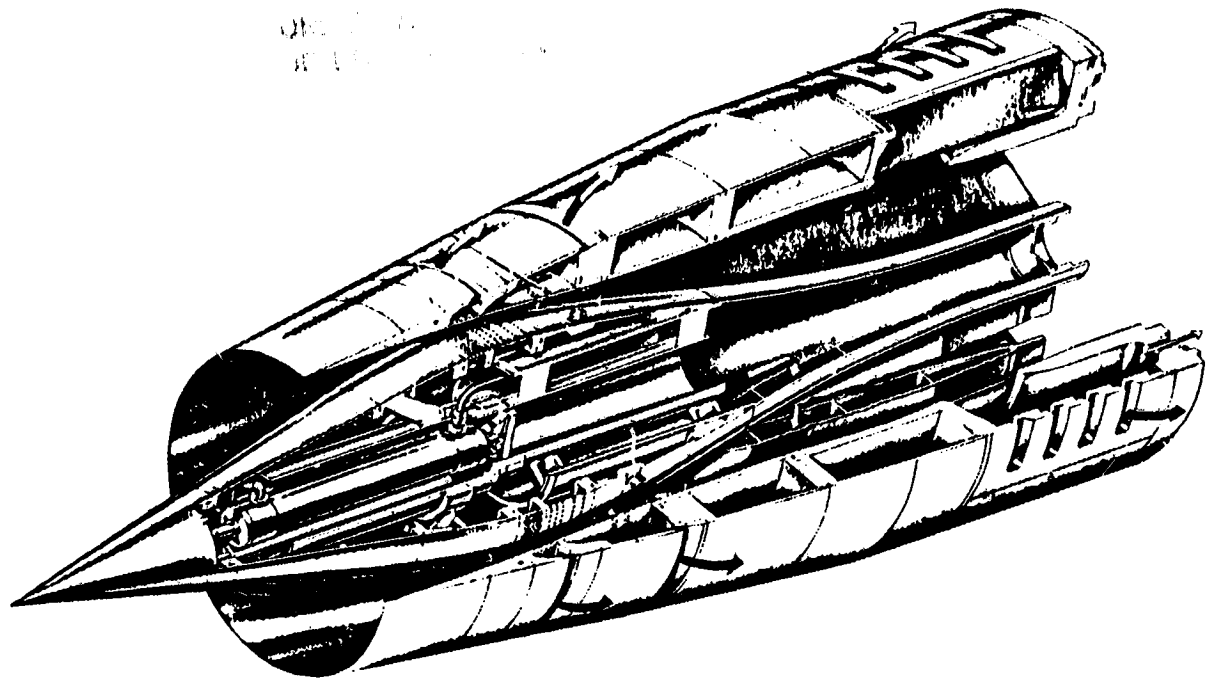


**FIGURE 1. AXISYMMETRIC MIXED-COMPRESSION SUPERSONIC INLET**

ORIGINAL COPY  
OF POOR QUALITY

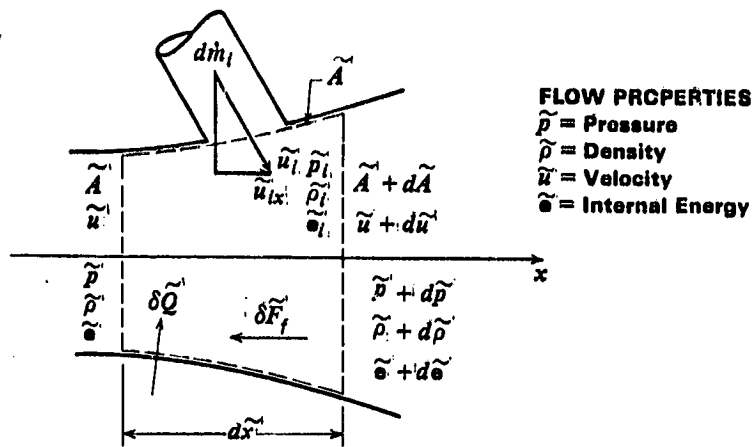


FIGURE 2. FLOW MODEL FOR UNSTEADY QUASI-ONE-DIMENSIONAL INVISCID FLOW WITH FRICTION, HEAT TRANSFER, AND MASS ADDITION

Continuity

$$\frac{\partial(\tilde{\rho}\tilde{A})}{\partial\tilde{t}} + \frac{\partial(\tilde{\rho}\tilde{u}\tilde{A})}{\partial\tilde{x}} = \tilde{M}_s \quad (1)$$

Momentum

$$\frac{\partial(\tilde{\rho}\tilde{u}\tilde{A})}{\partial\tilde{t}} + \frac{\partial[\tilde{A}(\tilde{p} + \tilde{\rho}\tilde{u}^2)]}{\partial\tilde{x}} = -\tilde{p} \frac{\partial\tilde{A}}{\partial\tilde{x}} + \tilde{F}_s \quad (2)$$

Energy

$$\frac{\partial(\tilde{E}\tilde{A})}{\partial\tilde{t}} + \frac{\partial[\tilde{A}\tilde{u}(\tilde{E} + \tilde{p})]}{\partial\tilde{x}} = -\tilde{p} \frac{\partial\tilde{A}}{\partial\tilde{x}} + \tilde{Q}_s \quad (3)$$

where

$$\tilde{E} = \tilde{\rho}(\tilde{e} + \frac{1}{2}\tilde{u}^2) = \rho(c_v\tilde{T} + \frac{1}{2}\tilde{u}^2)$$

$\tilde{M}_s$  = Mass bleed term

$\tilde{F}_s$  = Friction term + mass bleed momentum term

$\tilde{Q}_s$  = Heat transfer term + mass bleed energy term

The flow is taken to be thermally and calorically perfect air obeying the perfect gas equation of state

$$\tilde{p} = \tilde{\rho} R \tilde{T} = (\gamma - 1) [\tilde{E} - \frac{1}{2} \tilde{\rho} \tilde{u}^2] \quad (4)$$

with

ORIGINAL PAGE IS  
OF POOR QUALITY

$$\gamma = \frac{c_p}{c_v} \quad (5)$$

For the present supersonic inlet flow application, friction and heat transfer effects are not considered.

Equations (1), (2), and (3) are written in what is known as weak conservation law form, with source/sink terms on the right-hand side. When these equations are written in this form and are solved numerically for a supersonic flow, embedded shock waves and expansion waves can form and decay automatically without special treatment of any kind. The source/sink terms  $\tilde{M}_s$ ,  $\tilde{F}_s$ , and  $\tilde{Q}_s$  are used to incorporate mass bleed/bypass effects as well as inlet unstart/restart phenomena. Further observe that the area variation terms in the momentum and energy equations also play the role of source/sink-like terms.

### 3.2 NONDIMENSIONAL GOVERNING EQUATIONS

The governing equations of motion (1), (2), and (3) may be written in the following vector form

$$\frac{\partial \vec{U}}{\partial t} + \frac{\partial \vec{F}}{\partial x} = \vec{G} \quad (6)$$

where the vector components U, F, and G are given by

$$\vec{U} = \begin{pmatrix} \hat{p} \\ \hat{p} \hat{u} \\ \hat{E} \end{pmatrix} \quad (7)$$

$$\vec{F} = \begin{pmatrix} \hat{p} \hat{u} \\ \hat{p} + \hat{p} \hat{u}^2 \\ \hat{u}(\hat{E} + \hat{p}) \end{pmatrix} \quad (8)$$

$$\vec{G} = \begin{pmatrix} \hat{M}_s \\ \hat{p}\hat{A}_x/\hat{A} + \hat{F}_s \\ -\hat{p}\hat{A}_t/\hat{A} + \hat{Q}_s \end{pmatrix}$$

ORIGINAL EQUATION  
OF FOUR QUANTITIES

(9)

with the following nondimensional variables

$$t = \frac{U_{\text{ref}} \tilde{t}}{L_{\text{ref}}} \quad x = \frac{\tilde{x}}{L_{\text{ref}}} \quad \hat{Q}_s = \frac{\tilde{Q}_s L_{\text{ref}}}{\rho_{\text{ref}} U_{\text{ref}}^3 A_{\text{ref}}}$$

$$\hat{p} = \frac{\tilde{p}\tilde{A}}{\rho_{\text{ref}} A_{\text{ref}}} \quad \hat{u} = \frac{\tilde{u}}{U_{\text{ref}}}$$

$$\hat{p} = \frac{\tilde{p}\tilde{A}}{\rho_{\text{ref}} U_{\text{ref}}^2 A_{\text{ref}}} \quad \hat{E} = \frac{\tilde{E}\tilde{A}}{\rho_{\text{ref}} U_{\text{ref}}^2 A_{\text{ref}}}$$

$$\hat{A} = \frac{\tilde{A}}{A_{\text{ref}}} \quad \hat{T} = \frac{\tilde{T}}{T_{\text{ref}}}$$

$$\hat{M}_s = \frac{\tilde{M}_s L_{\text{ref}}}{\rho_{\text{ref}} U_{\text{ref}} A_{\text{ref}}} \quad \hat{F}_s = \frac{\tilde{F}_s L_{\text{ref}}}{\rho_{\text{ref}} U_{\text{ref}}^2 A_{\text{ref}}}$$

In the above, terms denoted by "ref" denote constant reference conditions, selected to be free-stream sonic conditions in the present work. In addition, the reference area is related to the reference length through

$$A_{\text{ref}} = L_{\text{ref}}^2$$

and the equation of state (4) is given by

$$\hat{p} = (\gamma - 1) \left[ \hat{E} - \frac{1}{2} \hat{u}^2 \right] \quad (10)$$

in terms of the nondimensional variables.

The remainder of this report will utilize subscript notation to denote partial differentiation. In subscript notation, Eq. (6) becomes

$$\vec{U}_t + \vec{F}_x = \vec{G} \quad (11)$$

where  $\vec{U}_t = \frac{\partial \vec{U}}{\partial t}$ ,  $\vec{F}_x = \frac{\partial \vec{F}}{\partial x}$ .

ORIGINAL PAPER IS  
OF HIGH QUALITY

### 3.3 COORDINATE TRANSFORMATION

The governing vector equation (11) is now transformed in terms of the generalized coordinates  $\tau$  and  $\xi$  where

$$\tau = t, \quad \xi = \xi(x, t) \quad (12)$$

For a function  $f = f(x, t)$

$$\begin{pmatrix} f_\xi \\ f_\tau \end{pmatrix} = \begin{bmatrix} x_\xi & t_\xi \\ x_\tau & t_\tau \end{bmatrix} \begin{pmatrix} f_x \\ f_t \end{pmatrix} \quad (13)$$

where the subscript denotes partial differentiation, i.e.,

$$f_\xi = \frac{\partial f}{\partial \xi}, \quad t_\tau = \frac{\partial t}{\partial \tau}$$

Since  $t_\xi = 0$  from the definition of  $\tau$ , the Jacobian matrix of the generalized coordinate transformation becomes

$$J = \begin{bmatrix} x_\xi & 0 \\ x_\tau & 1 \end{bmatrix} = x_\xi \quad (14)$$

In terms of the generalized  $\tau$ ,  $\xi$  coordinates, the governing vector equation (6) may be written as

$$(x_\xi \vec{U})_\tau + (\epsilon_x x_\xi \vec{F} + \epsilon_t x_\xi \vec{U})_\xi = x_\xi \vec{G} \quad (15)$$

Recalling that  $x_\xi = J$  from Eq. (14) and defining

$$\begin{aligned} U &= x_\xi \vec{U} = J \vec{U} \\ F &= x_\xi \vec{F} = J \vec{F} \\ G &= x_\xi \vec{G} = J \vec{G} \end{aligned} \quad (16)$$

the transformed governing vector equation (15) becomes

$$U_\tau + (\epsilon_x F + \epsilon_t U)_\xi = G \quad (17)$$

where the term  $\xi_x$  is known as the metric coefficient and the term  $\xi_t$  as the grid speed (see Ref. 10 for the clarification).

The above transformation of coordinates can be thought of as a real nonsingular mapping from the physical  $(x, t)$  space to a computational  $(\xi, \tau)$  space. Equation (17) will be solved by a numerical method (to be described later) in the computational  $(\xi, \tau)$  space with the resulting solution transformed back into physical  $(x, t)$  space for interpretation. For the present work, the grid speed  $\xi_t$  is taken to be zero; thus, the resulting  $\xi$  grid distribution will not be allowed to change with respect to time, i.e., the grid is nonadaptive. A good discussion of adaptive grids and the many problems involved in proper determination of the grid speed  $\xi_t$  may be found in Ref. 10.

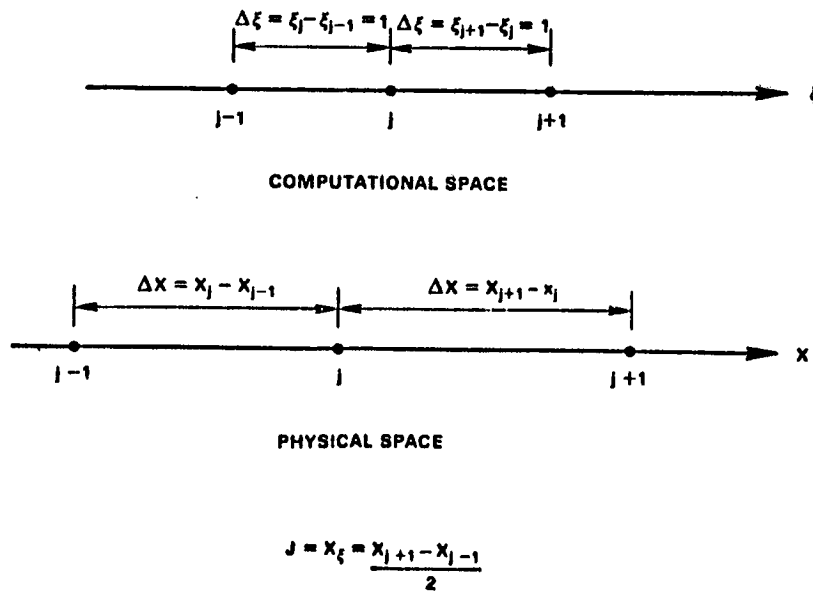
Under the restriction of zero grid speed, Eq. (17) reduces to

$$U_\tau + (\xi_x F)_\xi = G \quad (18)$$

where

$$\xi_x = \frac{1}{x_\xi} = \frac{1}{J} \quad (19)$$

is related to the Jacobian of the transformation given in Eq. (14). For implementation in the various numerical algorithms to be discussed in the next section, a grid spacing of unity ( $\Delta\xi=1$ ) is utilized in the computational space. The Jacobian  $J$  in Eq. (19) is then computed numerically per the following schematic illustration.





### 3.4 NUMERICAL METHODS

#### 3.4.1 Beam-Warming Algorithm

The Beam-Warming solution technique is based on the work of Beam and Warming (Refs. 11 and 12). The governing flow equations as given in Eq. (18) are solved using a non-iterative, implicit, first-order-time-accurate solution technique constructed in delta format (i.e., increments of the conserved variables and fluxes). The delta format is used extensively to achieve analytical simplicity and numerical efficiency in addition to the advantageous property of a steady state, when one exists, independent of the time step. Fourth order dissipation is added explicitly to the solution variables to achieve numerical stability over a wide range of Courant numbers.

The following subsections describe the Beam-Warming technique as applied to the solution of the one-dimensional flow equations as given in Eq. (18). The subsections are devoted to the definition of:

1. Implicit solution technique
2. Boundary point technique
3. Boundary condition constraints
4. Hybrid solution technique

##### 3.4.1.1 Implicit Solution Technique

Following Ref. 12, the Pade' formula is applied to the vector form of Eq. (18). The Pade' formula for implicit time differencing is

$$\frac{\partial U^N}{\partial t} = \frac{1}{\Delta\tau} \left( \frac{\Delta}{1+\Delta} \right) U^N \quad (20)$$

where the Pade' formula has been restricted to the Euler implicit temporal differencing with truncation errors  $O(\tau^2)$ . This specific form was chosen over others available from this formula (such as the Euler explicit, trapazodial, and three point backward) based on a combination of ease of implementation, relative speed, and accuracy. As used here, the superscript N denotes the time level, and  $\Delta$  is the forward time difference operator, given by

$$\Delta U = U^{N+1} - U^N \quad (21)$$

ORIGINAL DESIGN  
OF POOR QUALITY.

Applying the Pade' formula given in Eq. (20) to the governing one-dimensional flow equations, Eq. (18), there results

$$\Delta U^N + \Delta \tau (\bar{F}_\xi - G)^{N+1} = 0 \quad (22)$$

where  $\bar{F} = \xi_x F$ .

The terms F and G are locally linearized in time by using truncated Taylor series expansions

$$\begin{aligned} \bar{F}^{N+1} &= \bar{F}_U^N U^{N+1} + \bar{F}_\tau \Delta \tau + \dots = A^N U^{N+1} + \bar{F}_\tau \Delta \tau + \dots \\ G^{N+1} &= G^N + G_U^N \Delta U^N + G_\tau \Delta \tau + \dots = G^N + B^N \Delta U^N + G_\tau \Delta \tau + \dots \end{aligned} \quad (23)$$

where A is the Jacobian matrix of the governing one-dimensional equations Eq. (18). Here the homogenous property of the flux vector was used to simplify the expansion of the flux vector, F. Substitution of the expansions given by Eq. (23) into Eq. (22) and collecting terms, Eq. (22) can be approximated as

$$[I + \Delta \tau (\frac{\partial A^N}{\partial \xi} - B^N)] \Delta U^N = r^N \quad (24)$$

where  $r^N = \Delta \tau [G_\tau \Delta \tau - (A^N U^N)_\xi + G^N]$  (25)

As used here, I is the identity matrix and  $\frac{\partial A^N}{\partial \xi} - B^N$  is a matrix operator.

Equations (24) and (25) can be evaluated once the spatial derivative operators are replaced by finite-difference operators. The solution vector at the "new" time-step is obtained by casting Eqs. (24) and (25) into a block tri-diagonal structure and solving for the deltas of the dependent variables where the old and new time-step solutions are related to the deltas through Eq. (21). Applying central, second order spatial differences to Eqs. (24) and (25), Eq. (26) results

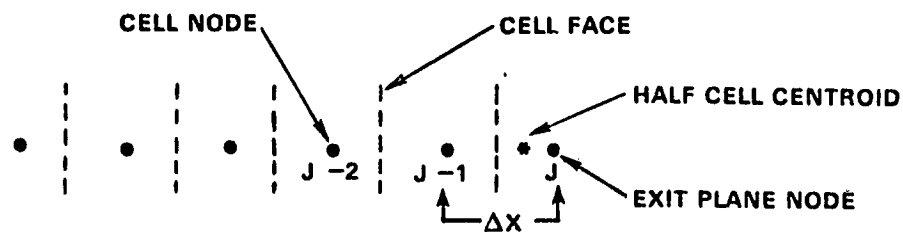
$$\bar{A} \Delta U_{j-1} + \bar{B} \Delta U_j + \bar{C} \Delta U_{j+1} = r_j \quad (26)$$

where  $\bar{A} \equiv -\frac{\Delta\tau}{2} A$ ,  $\bar{B} \equiv I - \Delta\tau B$  and  $\bar{C} \equiv \frac{\Delta\tau}{2} A$ . Here,  $j$  can take on values inside the upstream to downstream boundaries. Explicit fourth-order dissipation is added to the right hand side,  $r_j$ , terms to provide numerical stability following Ref. 12. These dissipative terms are of higher order than the difference forms used in the governing equations and consequently do not disrupt the formal accuracy of the method. Boundary point formulations similar to those for interior points will be described in the following subsection.

### 3.4.1.2 Boundary Point Technique

The boundary point-difference equations are formulated to have the same time accuracy as the interior point equations and are compatible with the latter in their spatial order of accuracy. This treatment of boundary points is patterned after that presented in Ref. 13 in that it provides a fully implicit set of equations for the boundary points. The time differencing for boundary points is the same as that for interior points. However, it is convenient to perform the spatial differencing before linearizing the equations in time. From this approach, the boundary conditions enter naturally into the difference equations.

Associated with the outflow boundary point is a half-cell where the centroid of the half-cell is indicated by the asterisk as shown below.



The exit plane node point which lies in the exit plane boundary is designated as point J. The difference form of the governing Eq. (18) at the boundary half-cell centroid is

$$\frac{\partial U^*}{\partial \tau} + \nabla F_J = G_J \quad (27)$$

where  $\nabla$  is the backward spatial difference operator. Equation (27) retains the global conservation property as pointed out in Ref. 13 if the half-cell centroid is defined by linear interpolation of data between the centroid of the last interior cell and the boundary as

$$U^* = (I - \frac{\nabla}{4}) U_J \quad (28)$$

Combining Eqs. (27), (28), and the Pade' formula, Eq. (20), and writing the result in a block tri-diagonal structure, Eq. (29) results.

$$\bar{A} \Delta U_{J-1} + \bar{B} \Delta U_J = r_J^* \quad (29)$$

with  $\bar{A} \equiv I/4 - \Delta\tau A$ ,  $\bar{B} = 3I/4 + \Delta\tau(A-B)$  and  $r_J^*$  is an interpolated value using points J and J-1.

A similar analysis for the inflow or entrance plane boundary equation results in the inflow boundary point equation given in Eq. (30).

$$\bar{B} \Delta U_1 + \bar{C} \Delta U_2 = r_1^* \quad (30)$$

Here,  $B = I/4 + \Delta\tau A$  and  $C = 3I/4 - \Delta\tau(A+B)$  and  $r_1^*$  is obtained by interpolation between points 1 and 2 at the upstream boundary.

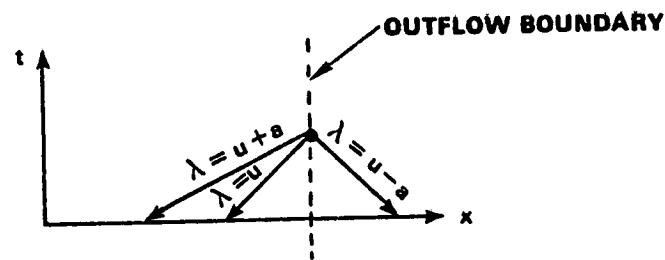
The inflow and outflow equations given by Eqs. (29) and (30) complete the block tri-diagonal equation structure for the boundary as well as interior grid points necessary to solve for the interior flow solution. The following subsections will consider the required outflow or exit plane and inflow or inlet plane boundary constraints required to close the system of solution equations.

### 3.4.1.3 Boundary Condition Constraints

For purely supersonic outflow, all characteristics ( $u \geq a$ ) have positive slope and emanate from the interior toward the boundary. The flow variables at the outflow boundary are determined by the interior flow. In this case, the full set of flow boundary conditions, Eq. (29), are used to evaluate boundary conditions at the outflow boundary.

For subsonic outflow ( $u \leq a$ ) all except one characteristic has a positive slope as shown below.

ORIGINAL PAGE IS  
OF POOR QUALITY



Information propagates upstream along the characteristics from the boundary point to the interior flow region. For the case of  $u \leq a$  at the outflow boundary, one boundary condition or constraint may be specified. In this case, Eq. (29) is modified to account for the constraint where a linearized algebraic boundary condition is used in place of one of the three equations. This algebraic relation will be referred to hereafter as a constraint.

Permissible exit plane boundary condition constraints, as used here for  $u \leq a$ , are specified pressure, Mach number, and mass flow. Corrected mass flow can be related directly to the exit plane Mach number and, thus, is treated like an exit plane Mach number constraint.

With the aid of Eq. (4) and the definition of the  $U$  vector in Eq. (7), the boundary condition with static pressure  $p$  as a constraint will be derived. Using Eq. (4) as the algebraic relation to impose the

pressure  $p$  as a constraint and writing in terms of the  $U$  vector elements, one obtains

$$p = (\gamma - 1)(U_3 - \frac{1}{2}U_2^2/U_1) \quad (31)$$

This constraint is to be satisfied at  $\tau^{N+1}$  by a function  $F$  such that

$$F^{N+1}(U, \tau) = 0 \quad (32)$$

where  $(33)$

$$F(U, \tau) = (\gamma - 1)(U_3 - \frac{1}{2}U_2^2/U_1) - p(t) = 0$$

If the constraint function  $F$  is linearized in time and the constraint defined in Eq. (32) is imposed, the linearized form of the constraint equation can be cast in a block tri-diagonal form that is compatible with the governing equation structure. The result is

$$(0)\Delta U_{j-1} + \bar{B} \Delta U_j = r_j \quad (34)$$

with  $\bar{B} \equiv \frac{\partial F^N}{\partial U}(U, \tau)$ , and  $r_j \equiv -F^N(U, \tau) - \frac{\partial F^N}{\partial p}(U, \tau) \frac{dp}{d\tau} \Delta \tau$ . This algebraic equation is used to replace the third equation (energy equation) in Eq. (29) for the exit plane boundary condition.

The outflow Mach number constraint is imposed in a manner similar to the exit pressure constraint developed in the previous paragraph. The outflow Mach number constraint is imposed through the Mach number definition as given in Eq. (35)

$$M = \frac{u}{a} = \frac{u}{\sqrt{\gamma p / \rho}} \quad (35)$$

and is written in terms of the  $U$  vector elements as

$$F(U, 2) = (U_2/U_1) / [\gamma(\gamma - 1)(U_3/U_1 - \frac{1}{2}(U_2/U_1)^2)]^{1/2} - M(t) \quad (36)$$

ORIGINAL PAPER  
OF POOR QUALITY

The constraint equation given in Eq. (34) is imposed with, however, the right hand side term,  $r_j$ , given by

$$r_j \equiv -F^N(U, \tau) - \frac{\partial F^N}{\partial M}(U, \tau) \frac{dM}{d\tau} \Delta\tau \quad (37)$$

This algebraic constraint equation for Mach number replaces the third or energy equation in Eq. (29).

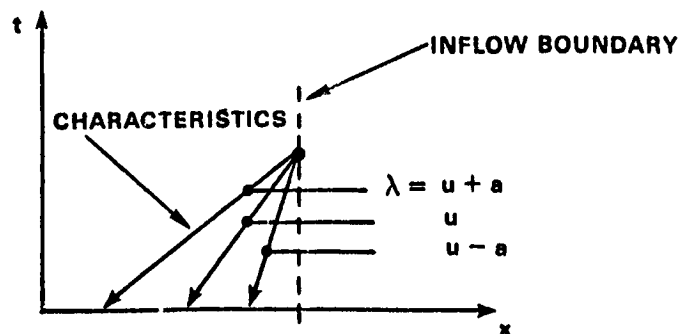
For the outflow mass flow constraint, the second equation in Eq. (29) (momentum equation) is replaced. The mass flow constraint is given in Eq. (38).

$$F^N(U, \tau) = U_2 - \dot{m}(\tau) = 0 \quad (38)$$

where the  $r_j$  term in Eq. (34) takes on the form

$$r_j = -F^N(U, \tau) - \frac{\partial F^N}{\partial \dot{m}}(U, \tau) \frac{d\dot{m}}{d\tau} \Delta\tau \quad (39)$$

The inflow boundary constraints are formulated in a manner similar to the outflow constraints as developed in the previous paragraphs. Permissible boundary conditions at the inflow boundary were developed by examining the characteristics at the inlet plane. With reference to the sketch below for supersonic inflow where  $u > a$ , all characteristics have positive slope and are directed downstream into the interior. Since no information propagates upstream across the inflow boundary, all inflow boundary variables must be specified and are not constrained by the interior flow solution.



### 3.4.2 Beam-Warming Hybrid Algorithm

Typical supersonic inlet flows are characterized by moving moderate-strength shocks. For a numerical solution scheme to be adequate and robust as applied to inlet flows, it must resolve these discontinuities accurately with minimal overshoot and remain stable as shock strengths increase. The Beam and Warming method developed in the previous subsections, even with significant fourth-order dissipation added, can become numerically unstable for moving moderate-strength shocks. This is due to the characteristic pressure undershoot in the predicted pressure just upstream of the shock in a supersonic inlet flow. Increasing the fourth order dissipation will not resolve the stability problem and will seriously degrade the shock tracking accuracy of the scheme.

In order to partially resolve this numerical resolution and stability problem, the spatial difference operators as applied in the Beam-Warming method are replaced by switching operators that convert from central to upwind (one-sided) across shock discontinuities. Basically, this modification attempts, in a heuristic manner, to replace the central difference operators in the Beam-Warming technique with operators that reflect the propagation of information based on the local characteristic directions at a point in the flow. This modification to the Beam-Warming technique, hereafter referred to as the Beam-Warming Hybrid technique, follows the development given in Ref. 11.

The central spatial difference operator used to develop Eq. (26) is replaced by a switching difference operator given in Eq. (40) where the switching or transition operators that change from central to upwind maintain strict conservation and local consistency.

$$\frac{\partial U}{\partial \xi} \approx \frac{1}{\Delta \xi} \frac{\nabla + \nabla \Delta / 2 - \nabla \epsilon \Delta / 2}{1 - \nabla \epsilon / 2} U \quad (40)$$

As used here,  $\nabla$  and  $\Delta$  are the classical backward and forward finite-difference operators, respectively, and  $\epsilon$  is a switching parameter. When  $\epsilon = 0$ , Eq. (40) reduces to a central difference operator, and when  $\epsilon = 1$ , an upwind difference operator results.



Applying the Eq. (40) difference operator to Eqs. (24) and (25) and combining terms, Eqs. (41) and (42) result

$$\begin{aligned} & [\bar{A} + \epsilon_{j-1}/2 - \Delta\tau\epsilon_{j-1} (B_{j-1}^N + A_{j-1}^N)/2] \Delta U_{j-1} \\ & + [\bar{B} - \epsilon_j/2 + \Delta\tau\epsilon_j (B_j^N + A_j^N)/2 + \Delta\tau\epsilon_{j-1} A_j/2] \Delta U_j \\ & + [\bar{C} - \epsilon_j \Delta\tau A_{j+1}/2] \Delta U_{j+1} = \bar{r}^N \end{aligned} \quad (41)$$

$$\begin{aligned} \bar{r}^N & \equiv r^N + \Delta\tau\epsilon_j [-G_j^N + (A_{j+1}^N U_{j+1} - A_j^N U_j)]/2 \\ & + \Delta\tau\epsilon_{j-1} [G_{j-1}^N - (A_j^N U_j - A_{j-1}^N U_{j-1})]/2 \end{aligned} \quad (42)$$

Here, the matrices  $\bar{A}$ ,  $\bar{B}$ , and  $\bar{C}$ , and the right hand side vector,  $r^N$ , are the Beam-Warming matrices as used in Eq. (26).

In a like manner, the fourth order dissipation difference term in the Beam-Warming scheme,  $\delta^4 U_j$ , is replaced by a conservative switching operator of the form

$$\begin{aligned} \delta^4 U_j & = [(1-\epsilon_j) - (1-\epsilon_{j-1}) E^{-1}] Q_j \\ Q_j & \equiv U_{j+2} - 3U_{j+1} + 3U_j - U_{j-1} \\ E^{-1} Q_j & \equiv Q_{j-1} \end{aligned} \quad (43)$$

The switching scheme is implemented by defining  $\epsilon = 0$  for subsonic points where a central difference is to be imposed and  $\epsilon = 1$  for supersonic points where a upwind scheme is applied. Conservation of this scheme is maintained across a shock discontinuity by redefining the switching operator for the last supersonic point upstream of the shock at  $\epsilon = 0$ .

### 3.4.3 Flux Vector Splitting Algorithm

The Beam-Warming hybrid solution technique outlined in the previous subsection provides an engineering approach to account for the propagation characteristics of flow information in flows containing

moving shock discontinuities. It will be shown in a later section that this approach yields robust solutions for flows containing moving shocks. Numerical solution oscillations still persist, however, in subsonic regions downstream of the shock that cannot be adequately damped without seriously degrading solution accuracy.

A new solution technique recently introduced by Steger and Warming (Ref. 14) and extended to a shock capturing algorithm by Reklis and Thomas (Ref. 15) provides a physically and mathematically consistent approach to include characteristic regions of influence in the solution algorithm. In this approach the flux vector of the governing one-dimensional equations is split into flux pieces corresponding to the three eigenvalues of the linear system. Contributions of the flux pieces, depending upon the signs of the eigenvalues, are employed to structure the matrix coefficients,  $\bar{A}$ ,  $\bar{B}$ , and  $\bar{C}$  (similar to those used in Eq. 26) so that spatial differences also reflect the direction of information propagation. This splitting and recombination of flux information is entirely consistent with the propagation of characteristics information. It results in a method that not only yields robust solutions for moderate strength moving shocks but also exhibits enhanced solution fidelity when compared to the Beam-Warming methods. The flux vector split technique as developed here follows the approach of Reklis and Thomas (Ref. 15).

This technique, as with the Beam-Warming approaches, is based on a local linearization of the governing flow equations, Eq. (18). Equation (18) is locally linearized by employing the Jacobian matrix,  $J = \partial \bar{F} / \partial U$ , and the homogeneous property of the flux vector  $\bar{F}$ . The Jacobian matrix  $\partial \bar{F} / \partial U$  is diagonalized by a similarity transformation (Ref. 14) as

$$\Lambda = S \frac{\partial \bar{F}}{\partial U} S^{-1} = \begin{bmatrix} u-a & & 0 \\ & u & \\ 0 & & u+a \end{bmatrix} \quad (44)$$

where the matrices  $S$  and  $J$  are defined in Ref. 14. Decomposition of the Jacobian matrix is achieved by

$$\frac{\partial \bar{F}}{\partial U} = (u-a)\psi_1 + u\psi_2 + (u+a)\psi_3 \quad (45)$$

where the  $\psi$  values are the decomposition functions (see Ref. 14).

Using the homogeneous property of the flux vector, the flux vector can be split into flux pieces,  $\bar{F}_1$ ,  $\bar{F}_2$ ,  $\bar{F}_3$  corresponding to each eigenvalue that describes the speed and direction of disturbance propagation in the fluid. These flux pieces can be written as

$$\begin{aligned}
 \bar{F}_1 &= u \frac{(\gamma-1)}{\gamma} \begin{bmatrix} \rho \\ \rho u \\ \rho u^2/2 \end{bmatrix} \\
 \bar{F}_2 &= \frac{u+a}{2\gamma} \begin{bmatrix} \rho \\ \rho(u+a) \\ \rho u^2/2 + \frac{\gamma p}{\gamma-1} + \rho u a \end{bmatrix} \\
 \bar{F}_3 &= \frac{(u-a)}{2\gamma} \begin{bmatrix} \rho \\ \rho(u-a) \\ \rho u^2/2 + \frac{\gamma p}{\gamma-1} - \rho u a \end{bmatrix}
 \end{aligned} \tag{46}$$

The spatial integration of the governing system of equations is similar to the Beam-Warming approach except that the difference equations are derived using the fluxes at the grid cell boundaries rather than at the grid nodes. Formally, the derivative  $\partial \bar{F} / \partial \xi$  is replaced by

$$\frac{\partial \bar{F}}{\partial \xi} \approx \frac{\bar{F}(a + \Delta \xi / 2) - \bar{F}(a - \Delta \xi / 2)}{\Delta \xi} \tag{47}$$

where  $a$  is a typical node coordinate and  $\Delta \xi$  is the nodal spacing. The information to form the flux vector  $\bar{F}$  at the cell boundaries is obtained by a two-point interpolation of the appropriate flux pieces, depending on the sign of the eigenvalue associated with each piece. Extrapolated  $U$  elements are used to form the flux pieces at cell faces.

Application of the implicit time differencing for the split flux scheme is similar to the Beam-Warming approach except that the homogeneous property does not hold for the flux pieces. Linearization of the flux and source terms leads to

$$\begin{aligned}
 \bar{F}^{N+1} &= \bar{F}^N + A^N \Delta U + \dots \\
 G^{N+1} &= G^N + B^N \Delta U + G_T \Delta \tau + \dots
 \end{aligned} \tag{48}$$

ORIGINAL [REDACTED]  
OF POOR QUALITY

Applying Eq. (48) to the governing Eq. (22), the difference equation written in flux split notation becomes

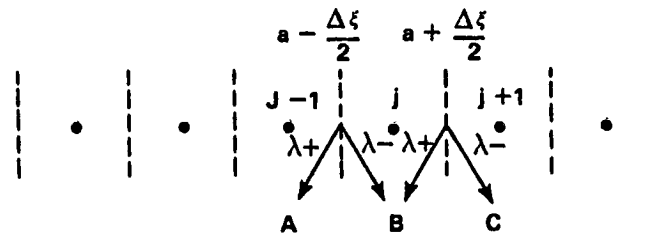
$$\left\{ I + \Delta\tau \left( \frac{\partial}{\partial U} \left[ \bar{F}_1 \left( a + \frac{\Delta\xi}{2} \right) + \bar{F}_2 \left( a + \frac{\Delta\xi}{2} \right) + \bar{F}_3 \left( a + \frac{\Delta\xi}{2} \right) \right] - \frac{\partial}{\partial U} \left[ \bar{F}_1 \left( a - \frac{\Delta\xi}{2} \right) + \bar{F}_2 \left( a - \frac{\Delta\xi}{2} \right) + \bar{F}_3 \left( a - \frac{\Delta\xi}{2} \right) \right] - B \right) \right\} \Delta U \quad (49)$$

$$= -\Delta\tau \left\{ \bar{F}_1 \left( a + \frac{\Delta\xi}{2} \right) + \bar{F}_2 \left( a + \frac{\Delta\xi}{2} \right) + \bar{F}_3 \left( a + \frac{\Delta\xi}{2} \right) \right.$$

$$\left. - \left[ \bar{F}_1 \left( a - \frac{\Delta\xi}{2} \right) + \bar{F}_2 \left( a - \frac{\Delta\xi}{2} \right) + \bar{F}_3 \left( a - \frac{\Delta\xi}{2} \right) \right] - G - G_\tau \Delta\tau \right\}$$

In this notation, the Jacobian matrices contained in Eq. (49) are operators on the vectors  $\Delta U(a)$ ,  $\Delta U(a + \Delta\xi)$ , and  $\Delta U(a - \Delta\xi)$ , thus providing the block tri-diagonal structure of the solution scheme.

The method used to form the left hand side coefficients  $\bar{A}$ ,  $\bar{B}$ , and  $\bar{C}$  for the governing equation, which is in the same form as Eq. (26), is based on the extrapolation from cell faces to nodes based on the sign of the eigenvalues. The following sketch serves to illustrate this extrapolation process.



The eigenvalues,  $\lambda^+$  and  $\lambda^-$ , as used here, denote positive and negative values, respectively. The sign of the eigenvalues,  $\lambda$ , determines, for the flux piece at the cell face  $a - \frac{\Delta}{2}\xi$  or  $a + \frac{\Delta}{2}\xi$ , whether the extrapolation fills the  $\bar{A}$  or  $\bar{B}$  matrix or  $\bar{B}$  or  $\bar{C}$  matrix, respectively. For the case where all three eigenvalues are of the same sign (positive, for example), then matrices  $\bar{A}$  and  $\bar{B}$  are filled with the  $\bar{C}$  contribution set to zero. If an eigenvalue changes signs within the three points,

$j + 1, j, j - 1$ , then the  $\bar{B}$  component is set to zero, and the  $\bar{A}$  and  $\bar{C}$  matrices are filled. The Jacobian pieces required in Eq. (49) are evaluated from the flux piece definitions given in Eq. (46).

Boundary conditions for the split flux scheme are treated in a manner similar to the Beam-Warming boundary conditions except that Eqs. (29) and (30) are altered to characteristic form. Following the diagonalization of the Jacobian matrix as given in Eq. (44), Eqs. (29) and (30) are rewritten as

$$SJ\bar{A} \Delta U_{j-1} + SJ\bar{B} \Delta U_j = SJr_j^* \quad (50)$$

$$SJ\bar{B} \Delta U_1 + SJ\bar{C} \Delta U_2 = SJr_1^* \quad (51)$$

where each equation in the above system is associated with an eigenvalue ( $u - a, u, u + a$ ). The characteristic directions are used to determine the equation to be replaced with algebraic constraints.

#### 3.4.4 Split Characteristics Algorithm

The Beam-Warming and split flux methods presented in the previous subsections utilized implicit finite-difference techniques to solve the governing flow equations. Both approaches resulted in a block tri-diagonal solution structure requiring the inversion at each time step of a system of block tri-diagonal equations to yield the flowfield solution at the node points. These implicit solvers, as shown in later sections, yield accurate solutions for complex flows including variable source terms over a wide range of Courant numbers.

The implicit algorithms have two basic problems, however, when applied to inlet flowfields. The first problem area lies in the basic solution technique which relies on the temporal linearization of the flux vector and source terms. This results in a relatively low maximum Courant number limit for complex flows. The second problem area lies in the execution time requirement of these implicit methods. Since a block tri-diagonal matrix must be inverted at each time step, solution times can become large for grids with a large number of node points.

To partially overcome these two drawbacks of the Beam-Warming and split flux algorithms, split characteristics and MacCormack algorithms are presented. These two techniques are based on a predictor-corrector solution approach (Refs. 16 and 17) that yields the same spatial accuracy as the Beam-Warming and split flux schemes, but does not require block tri-diagonal matrix inversion. This results in faster overall solution times for the predictor-corrector schemes when compared to the block tri-diagonal based algorithms. In addition, it will be shown that the split characteristics technique can be extended to higher Courant numbers (resulting in additional savings in computer solution time) than the split flux or Beam-Warming methods for a given complex flowfield.

The basic philosophy of the split characteristics approach is to use characteristic theory to determine the direction and magnitude of information propagation, which is accomplished by calculating the characteristic directions of the equations. The compatibility relationships, however, are not used in the conventional total derivative form. They are retained and used in partial derivative form. A conservative form of the governing equations is used to calculate the solution delta,  $\Delta U$ . Characteristic theory is employed to split these solution deltas which are then propagated in the appropriate direction and transformed back to original variables.

The result is a conservative, shock-capturing method using characteristic information. Boundary points are treated in a similar manner by combining the appropriate split components with known boundary conditions. This eliminates the need to arbitrarily guess which equations to keep and combine with the boundary conditions. Characteristics theory determines the information to be retained and discarded.

The following subsections contain a description of the split characteristics and MacCormack algorithms as applied to the quasi-one-dimensional flow equations. The subsections are devoted to the definition of:

1. Characteristic relations
2. Explicit split characteristics algorithms
3. Boundary conditions

4. Time integration algorithm
5. Implicit operator
6. Algorithm application

ORIGINAL PAPER IS  
OF POOR QUALITY

#### 3.4.4.1 Characteristic Relations

This subsection is devoted to the development of the characteristic equations. Compatibility equations and characteristic directions are defined corresponding to the eigenvalues of the system of equations. These relations are required in order to accurately and clearly present the split characteristics concept.

The governing system of equations defined in Eq. (18) can be written as

$$U_{\tau} + \xi_x A U_{\xi} = G^* \quad (52)$$

where  $G^* \equiv G - (\xi_x)_{\xi} F$  and  $A \equiv \partial F / \partial U$ . The characteristics are obtained by diagonalizing  $A$  (represented in Eq. 44). As used here, the diagonalizing matrix is given in Eq. (53).

$$S = \begin{bmatrix} 0 & -\rho a & 1 \\ a^2 & 0 & -1 \\ 0 & \rho a & 1 \end{bmatrix} \begin{bmatrix} 1 & 0 & 0 \\ -u/\rho & 1/\rho & 0 \\ (\gamma-1)u^2/2 & -(\gamma-1)u & \gamma-1 \end{bmatrix} \quad (53)$$

The second matrix,  $J_{cp}$  represents a transformation from conservative variables  $U$  to primitive variables  $U_p$  where

$$U = \begin{bmatrix} \rho \\ \rho u \\ E \end{bmatrix} \quad \text{and} \quad U_p = \begin{bmatrix} \rho \\ u \\ p \end{bmatrix} \quad (54)$$

The first matrix, then, transforms from primitive to characteristic form. This factored form is a convenient and efficient way to calculate the transformation. It is also needed for boundary condition calculations.

By diagonalizing the Jacobian A using Eq. (44), the governing equations can be cast into the partial differential form of the compatibility equations

$$S_i U_\tau + \epsilon_x \lambda_i S_i U_\xi = S_i G^* \quad (55)$$

where the compatibility equations hold along characteristic directions defined by

$$\frac{d\xi}{d\tau} = \epsilon_x \lambda_i \quad (56)$$

Equations (55) and (56) are the compatibility equation and characteristic direction pair corresponding to the eigenvalues  $\lambda_i$ . A typical characteristic method would finite difference the three compatibility equations along the corresponding three characteristic directions to calculate the U vector at a new time step. This requires interpolation since the characteristic directions do not necessarily align with the grid. Shocks also require special treatment in a characteristics method approach.

#### 3.4.4.2 Explicit Split Characteristics

It is the goal of split characteristics to use the characteristic information in a conservative form without requiring interpolation. In the split characteristics formulation, the partial differential form of the compatibility equation, Eq. (55), is used. The characteristic directions are applied, not as a direction for calculating total derivatives, but in determining the directions to calculate one sided partial derivatives. The following subsection separates the compatibility equations into pieces according to the characteristic directions, then transforms the resulting pieces back into conservative forms.

In order to split Eq. (55), it is convenient to define diagonal matrices  $D^+$  and  $D^-$  where the diagonal components,  $d$ , are

$$\begin{aligned} d_i^+ &= 1, \lambda_i \geq 0 \\ d_i^- &= 0, \lambda_i < 0 \end{aligned} \quad (57)$$



and  $D^- \equiv I - D^+$ . Multiplying Eq. (55) by  $D^\pm$ , Eq. (58) is obtained

$$D^\pm S U_\tau + \epsilon_x D^\pm \Lambda S U_\xi = D^\pm S G^* \quad (58)$$

where  $\Lambda = SAS^{-1}$  with  $A$  and  $S$  defined in Eq. (52) and (53), respectively. This operation splits the system into two systems. Those obtained from  $D^+$  are the partial differential form of the non-negative characteristic values, while those obtained from  $D^-$  correspond to the negative characteristic values. Each system contains a subset of the original three equations, and each equation is in one system or the other.

By defining the matrix  $I^\pm \equiv S^{-1}D^\pm S$  and noting that  $S^{-1}D^\pm \Lambda S = I^\pm A$ , the compatibility equation may be rewritten in the form given below.

$$I^\pm U_\tau + I^\pm (\epsilon_x F)_\xi = I^\pm G \quad (59)$$

Based on the form of Eq. (59), it is apparent that the operator  $I^\pm$  are splitting operators which split the original conservative equations into two parts, depending upon the characteristic directions. Equation (59) may be combined and rewritten as

$$U_\tau = (I^+ + I^-)U_\tau = I^+[G - (\epsilon_x F)_\xi] + I^-[G - (\epsilon_x F)_\xi] \quad (60)$$

The basic principle behind the split characteristic method is that for the  $I^+$  operator,  $G - (\epsilon_x F)_\xi$  is evaluated using backward derivatives, while for  $I^-$  forward derivatives are used. Actually,  $G - (\epsilon_x F)_\xi$  is evaluated only once per interval, as it is both a forward difference for the right point and a backward difference for the left point.

From Eq. (60) for each node interval (at a cell boundary), an unsplit solution delta ( $\Delta U$ ) is applied as follows

$$\Delta U = \Delta\tau [G - (\epsilon_x F)_{j+1} + (\epsilon_x F)_j] \quad (61)$$

where  $\Delta\xi = 1$  and  $j$  is the node number. To retain accurate wave speed characteristics, the pressure area term ( $\rho A_\xi/A$ ) in the source vector  $G$  is evaluated as

$$\rho A_\xi/A = (p_{j+1} + p_j) (A_{j+1} - A_j)/(A_{j+1} + A_j) \quad (62)$$

All other source terms are evaluated using averages of the interval end points.

Once the unsplit deltas, following Eq. (61), are evaluated, the deltas are then split using the  $I^\pm$  operator defined in the previous paragraphs. The  $I^\pm$  operators are evaluated using a transformed average following Roe (Ref. 18). Splitting is performed per the following matrix operation

$$\Delta U^\pm \equiv I^\pm \Delta U = S^{-1} D^\pm S \Delta U \quad (63)$$

The split  $\Delta U^\pm$  are combined at each point by summing the  $\Delta U^+$  from the interval left of the point and  $\Delta U^-$  from the interval right of the point.

Time integration of the governing equations is based on a two-step, second-order Runge-Kutta algorithm. The method applied here is identical to the MacCormack explicit algorithm (Ref. 16) except for the manner in which the spacial averages are evaluated. Application of the two step Runge-Kutta algorithm gives

$$\begin{aligned} \tilde{U} &= U^N + \Delta U \\ U^{N+1} &= 1/2(U^N + \tilde{U} + \Delta \tilde{U}) \end{aligned} \quad (64)$$

where  $U^N$  represents the old or time level  $N$  known solution, and  $\Delta U$  represents the combined split deltas obtained from Eq. (63). The superscript tilda designates predictor values. Time-dependent source terms are evaluated at the old time level and held fixed for the new level calculation. This method of treating the source terms is compatible with that used in the split flux and Beam-Warming schemes.

Application of Eq. (64) directly, with no splitting of the deltas, results in the explicit MacCormack algorithm. Fourth-order dissipation is employed for application of the explicit MacCormack method to eliminate the formation of expansion shocks.

### 3.4.4.3 Boundary Conditions

For application to supersonic inlets, the inflow boundary is assumed to be supersonic at all times. For supersonic flow at the inflow boundary plane, all three eigenvalues are positive. As a result, all of the characteristic directions point downstream. No information is passed upstream from the flow to the inflow boundary. Thus, all inflow conditions are specified from external considerations and are not part of the internal algorithms. As with the source terms, inflow boundary flow variables are needed at the old time-step and are held fixed for both the predictor and corrector steps.

The flow at the outflow boundary is assumed to be subsonic and outflowing. Under these conditions, two characteristics ( $u+a$  and  $u$ ) point downstream, while the  $(u-a)$  characteristic points upstream. The  $u-a$  characteristic information must therefore be discarded and replaced with a boundary condition constraint. As with the Beam-Warming and split flux solution schemes, boundary condition constraints implemented in the split characteristics scheme are specified static pressure, mass flow, and Mach number. A boundary condition is combined with the information from the  $u+a$  and  $u$  characteristics to obtain a  $\Delta U$  for the outflow boundary point.

For the outflow boundary, positive characteristic components are given by

$$D^+Q = \begin{bmatrix} 0 \\ Q_2 \\ Q_3 \end{bmatrix} = \begin{bmatrix} 0 & 0 & 0 \\ a^2 & 0 & -1 \\ 0 & \rho a & 1 \end{bmatrix} \begin{bmatrix} 1 & 0 & 0 \\ -u/\rho & 1/\rho & 0 \\ (\gamma-1)u^2/2 & -(\gamma-1)u & \gamma-1 \end{bmatrix} \Delta U \quad (65)$$

where the characteristic components of  $\Delta U$ , namely  $Q$ , are calculated by  $Q = S \Delta U$ . The above equation is used to calculate  $Q_2$  and  $Q_3$  from the unsplit  $\Delta U$  calculated from the last interval. The transformation matrices are evaluated using transformed averages of the last two points.

The transformation from  $\Delta U$  to  $Q_2$  and  $Q_3$  is singular. That is,  $Q_2$  and  $Q_3$  may be calculated from  $\Delta U$ , but  $\Delta U$  cannot be uniquely calculated from  $Q_2$  and  $Q_3$ . The additionally supplied boundary condition must be used to complete the system of equations and give a unique  $\Delta U$ .

Written in terms of the primitive variables  $U_p$  defined in Eq. (54), Eq. (65) becomes

$$\begin{bmatrix} 0 & 0 & 0 \\ a^2 & 0 & -1 \\ 0 & \rho a & 1 \end{bmatrix} \begin{bmatrix} \Delta \rho \\ \Delta u \\ \Delta p \end{bmatrix} = \begin{bmatrix} 0 \\ Q_2 \\ Q_3 \end{bmatrix} \quad (66)$$

The system of equations can be solved for  $\Delta U_p$  once the first equation in Eq. (66) is replaced with the outflow boundary condition or constraint equation.

The specified pressure boundary condition can be written as  $\Delta p = \Delta p^*$  where  $\Delta p^*$  is the known pressure increment. Replacing this equation with the first equation in Eq. (66) and solving for  $\Delta U_p$  results in

$$\begin{aligned} \Delta \rho &= (Q_2 + \Delta p^*)/a^2 \\ \Delta u &= (Q_3 + \Delta p^*)/\rho a \\ \Delta p &= \Delta p^* \end{aligned} \quad (67)$$

The primitive variables are related to the conservative variable,  $\Delta U$ , by

$$\Delta U = J_{cp}^{-1} \Delta U_p \quad (68)$$

where  $J_{cp}^{-1}$  is the inverse of  $J_{cp}$  as given in Eq. (53).

The specified mass flow and Mach number constraints are imposed in a manner similar to the pressure constraint except that linearized constraints equations are employed. For the mass flow boundary condition, the linearized constraint equation is

$$u\Delta\rho + \rho\Delta u = \Delta(\rho u)^* \quad (69)$$

with  $\Delta(\rho u)^*$  designating the known mass flow constraints. Utilizing Eq. (69) as the first equation in Eq. (66), the primitive variable constraints become

$$\begin{aligned} \Delta u &= (a^2\Delta(\rho u)^*/\hat{u} - Q_2 - Q_3)/(\hat{\rho}a^2/\hat{u} - \rho a) \\ \Delta p &= Q_3 - \rho a\Delta u \\ \Delta\rho &= (Q_2 + \Delta p)/a^2 \end{aligned} \quad (70)$$

The  $\hat{u}$  and  $\hat{\rho}$  variables are evaluated at the outflow point and not averaged as with the other elements of the transformation matrix.

For the specified Mach number constraint, the isentropic Mach number relation is used where

$$\gamma M^2 = \rho u^2/p \quad (71)$$

Equation (71) is linearized and substituted in Eq. (66) leading to the primitive variable constraints given in Eq. (72)

$$\begin{aligned} \Delta p &= [\gamma\hat{\rho}(\Delta M^2)^* - \hat{\rho}\hat{u}^2\hat{a}^2Q_2/a^2 - 2\hat{\rho}\hat{u}\hat{a}^2Q_3/\rho a]/ \\ &\quad (\hat{\rho}\hat{u}^2\hat{a}^2/a^2 - 2\hat{\rho}^2\hat{u}\hat{a}^2/\rho a - \gamma\hat{\rho}\hat{u}^2) \\ \Delta\rho &= (Q_2 + \Delta p)/a^2 \\ \Delta u &= (Q_3 - \Delta p)/\rho a \end{aligned} \quad (72)$$

The conservative form of the variables is obtained by applying Eq. (68) as before.

#### 3.4.4.4 Implicit Operator

The implicit operator used in the split characteristic scheme is an artifice used to raise the Courant number limit of the explicit algorithm while maintaining the original order of accuracy. It can be thought of as a smoother of the explicit calculations. It redistributes the explicit

deltas using the convective behavior of the original quasi-one-dimensional equations. It is equivalent to an implicit method where only selected terms are evaluated implicitly. This partial implicit concept results in considerable computational savings over a fully implicit method.

The operator used here is similar to MacCormack (Ref. 17) except that modifications are made to include split characteristic considerations. These modifications are easily made since the MacCormack algorithm already uses characteristic logic.

Following the MacCormack concept, the governing equations, Eq. (18), are differentiated in time leading to

$$U_{\tau\tau} + (\epsilon_X F)_{\xi\tau} = G_\tau \quad (73)$$

Reversing the order of differentiation and expanding the second term for a stationary grid gives

$$U_{\tau\tau} + (\epsilon_X A U_\tau)_\xi = G_\tau \quad (74)$$

Following the work of White (Ref. 19) the  $G_\tau$  term in Eq. (74) is discarded, which is equivalent to treating the source term explicitly. The inclusion of these source terms in the implicit algorithm would require knowledge of the partial derivative of the terms with respect to the dependent variables resulting in an increase in the computational effort.

Applying temporal differencing to the first term gives

$$(U_\tau^\beta - U_\tau^\alpha) + \Delta\tau(\epsilon_X A U_\tau^\beta)_\xi = 0 \quad (75)$$

where  $\alpha$  and  $\beta$  represent old and new time levels, respectively. Splitting the Jacobian matrix,  $A$ , results in

$$U_\tau^\beta + \Delta\tau[(\epsilon_X A^+ U_\tau^\beta)_\xi + (\epsilon_X A^- U_\tau^\beta)_\xi] = U_\tau^\alpha \quad (76)$$

Using spacial differences of  $\xi$  over their domain of influence and replacing  $U_t^\alpha$  and  $U_t^\beta$  with finite difference forms, Eq. (76) can be rewritten as

$$-\Delta\tau\xi_x A^+ \delta U_{j-1} + [I + \Delta\tau\xi_x (A^+ - A^-)] \delta U_j + \Delta\tau\xi_x A^- \delta U_{j+1} = \Delta U_j \quad (77)$$

where  $U_t^\alpha = \Delta U / \Delta\tau$  and  $U_t^\beta = \delta U / \Delta\tau$  has been used. Here  $j$  designates the centered node point and  $\xi_x$  and  $A^\pm$  are considered operators on  $\delta U$ . Equation (77) can be cast in a more symmetric form as given below

$$-\Delta\tau\xi_x |A^+| \delta U_{j-1} + (I + \Delta\tau\xi_x |A|) \delta U_j - \Delta\tau\xi_x |A^-| \delta U_{j+1} = \Delta U_j \quad (78)$$

which is, in form, the same as the tri-diagonal system developed for the implicit Beam-Warming method.

To further simplify algorithm solution requirements, the tri-diagonal implicit operator is factored into two bi-diagonal operators. The bi-diagonal systems, in addition to being simpler than a tri-diagonal system, easily convert to scalar equations employing the characteristic transformation used for splitting. The factorization is written as

$$(I + \Delta\tau\xi_x |A^+|) \hat{\delta U}_j = \Delta U_j + \Delta\tau\xi_x |A^+| \hat{\delta U}_{j-1} \quad (79)$$

$$(I + \Delta\tau\xi_x |A^-|) \delta U_j = \hat{\delta U}_j + \Delta\tau\xi_x |A^-| \delta U_{j+1} \quad (80)$$

The factorization is considered approximate as a higher order  $(\Delta\tau)^2$  term is dropped.

The characteristic transformation used to split the implicit operator is used to simplify the solution of the bi-diagonal systems. As applied here, these operators are actually block bi-diagonal systems with 3x3 blocks. The characteristic transformation provides for a solution to this system.

It is convenient to describe the algorithm assuming the right hand side (RHS) of the operators is already calculated. The algorithm then has two steps:

1. Solve for the  $\hat{\delta U}_j$  and  $\delta U_j$  following Eq. (79) and (80).
2. Propagate the appropriate terms to the RHS of the next spacial point.

One of the advantages of the MacCormack algorithm (Ref. 17) is its ability to be implicit where needed and to be explicit otherwise. This is accomplished by shifting the diagonal values of the implicit operator. The same principle can be used with the split characteristics scheme presented here. Denoting  $|\lambda_i^\pm|$  as the diagonal values of  $|\Lambda^\pm|$ , the parameter  $\hat{\lambda}_i^\pm$  can be defined as

$$\hat{\lambda}_i^\pm = \max (0, |\lambda_i^\pm| - CF/\epsilon_\chi \Delta\tau) \quad (81)$$

The split characteristics algorithm uses the magnitude and sign of  $\lambda$  for defining  $|\Lambda^\pm|$  instead of the magnitude of the eigenvalue as used in the MacCormack method.

The Courant Factor (CF) is the Courant number level at which the implicit operator is applied. Since the present explicit split algorithm appears stable to Courant number values slightly above 1, the CF was set at 1. The result is an algorithm that is explicit at points with a local Courant number less than 1, while smoothly transitioning to an implicit node at points where the Courant number is greater than 1.

#### 3.4.4.5 Algorithm Application

With the typical tri-diagonal methods, the boundary conditions and the tri-diagonal operator are combined into one system to be solved together. For the split characteristics scheme presented here, the bi-diagonal systems and the boundary conditions can be completely separated. However, there is an implied order of calculation. It is important to emphasize here, that a supersonic upstream boundary is a critical part of the factored algorithms. This supersonic condition separates the upstream boundary condition from the flow. Characteristic theory shows that the internal flow cannot influence the upstream boundary point. It is this fact that breaks the implicit coupling of the implicit operators and allows a starting point.



Application of the factored implicit algorithm can be described in the following four steps.

1. The explicit split deltas are calculated following Eq. (63).
2. The first implicit operator as given in Eq. (79) is applied by starting with the first interior point and ending with the outflow boundary point. This operator passes information downstream and is called the forward implicit operator. Since the upstream boundary condition is externally determined, the  $\delta U$  can be calculated in order, each point using values from the previous point.
3. The forward implicit operator also operates upon the partial  $\Delta U$  calculated at the outflow boundary point. The outflow boundary routine is identical to the external routine except that it uses  $\delta U$  instead of  $\Delta U$ .
4. After applying the appropriate outflow boundary condition, the backward operation as given in Eq. (80) is used. This operator starts at the last interior point and ends with the first interior point. Since  $|B|$  is null where flow is supersonic, the operator is a trivial identity operator for the leading supersonic points. The results of the outflow boundary algorithm are used to start the backward operator.
5. The variables are updated with the same second order Runge Kutta algorithm using  $\delta U$  instead of  $\Delta U$  as implied in Eq. (64).

### 3.5 GEOMETRY

Capabilities are provided for three types of axisymmetric or two-dimensional inlet geometries. The first geometry type is a simple duct with no centerbody. This geometry is useful primarily for comparison with other numerical solutions.

The second geometry type adds a fixed contour translating centerbody which may have one or two straight segments upstream of the cowl lip in the axisymmetric case or up to three in the two-dimensional case. The centerbody translates forward from a specified point to provide restart capability. A sketch illustrating this geometry is shown in Fig. 3.

The third geometry type has a variable diameter (or height) centerbody with a slot for bleed. Two straight segments upstream of the cowl lip are specified. The second segment is allowed to effectively rotate about the point joining the first two segments. A slot follows the second segment. The section downstream of the slot is also allowed

ORIGINAL PAGE IS  
OF POOR QUALITY

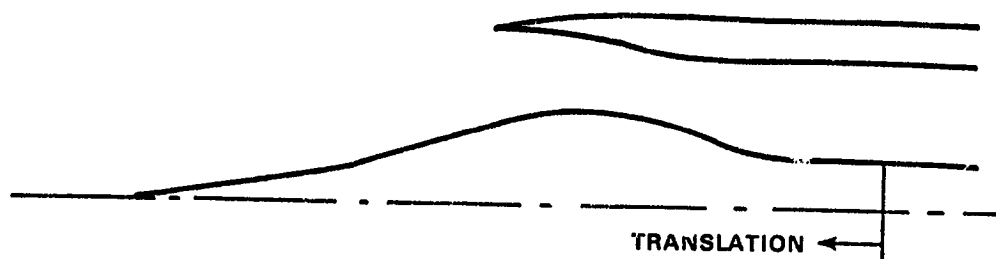


FIGURE 3. FIXED CONTOUR CENTERBODY GEOMETRY

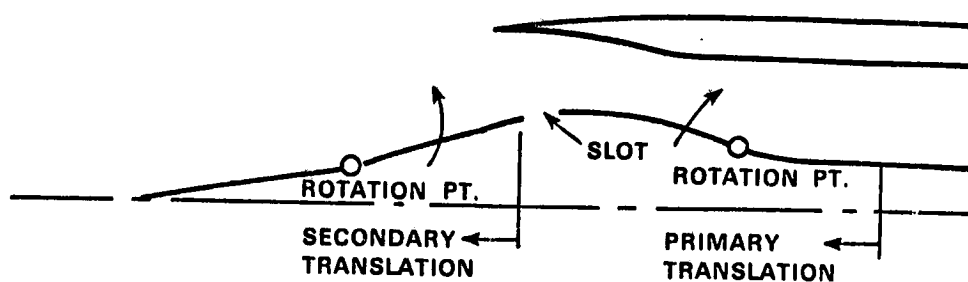


FIGURE 4. VARIABLE DIAMETER CENTERBODY GEOMETRY

to effectively rotate. In addition to the primary centerbody translation, a secondary translation of the first two segments is provided. A sketch illustrating this geometry is shown in Fig. 4.

The inlet cowl, centerbody, and in the two-dimensional case, width contours, are defined by up to 20 segments. The segments may be linear, parabolic, or cubic except for the centerbody segments upstream of the cowl lip which must be linear. The segments are defined by specifying end points and, in the case of parabolic or cubic segments, intermediate points or slopes at the end points.

### 3.6 UNSTART MODEL

When a supersonic inlet unstarts, the normal shock wave is expelled from the inlet and moves upstream toward the vertex of the centerbody as illustrated schematically in Fig. 5. Behind the normal shock wave the flow is subsonic, and, because the normal shock wave is detached from the inlet lip, there is spillage of the incoming air over the inlet housing. The operation of the inlet diffuser under this condition is said to be subcritical.

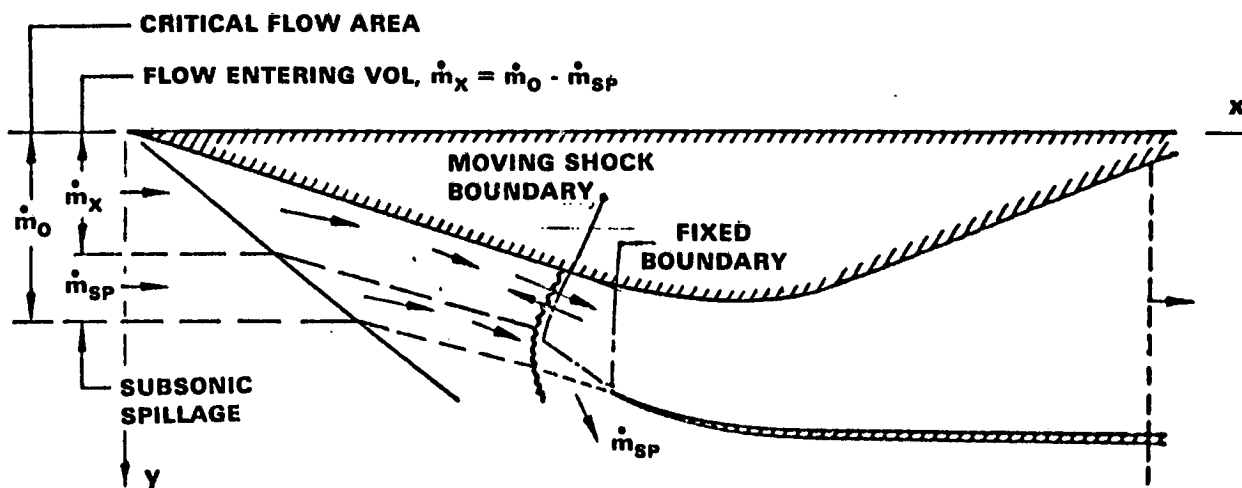
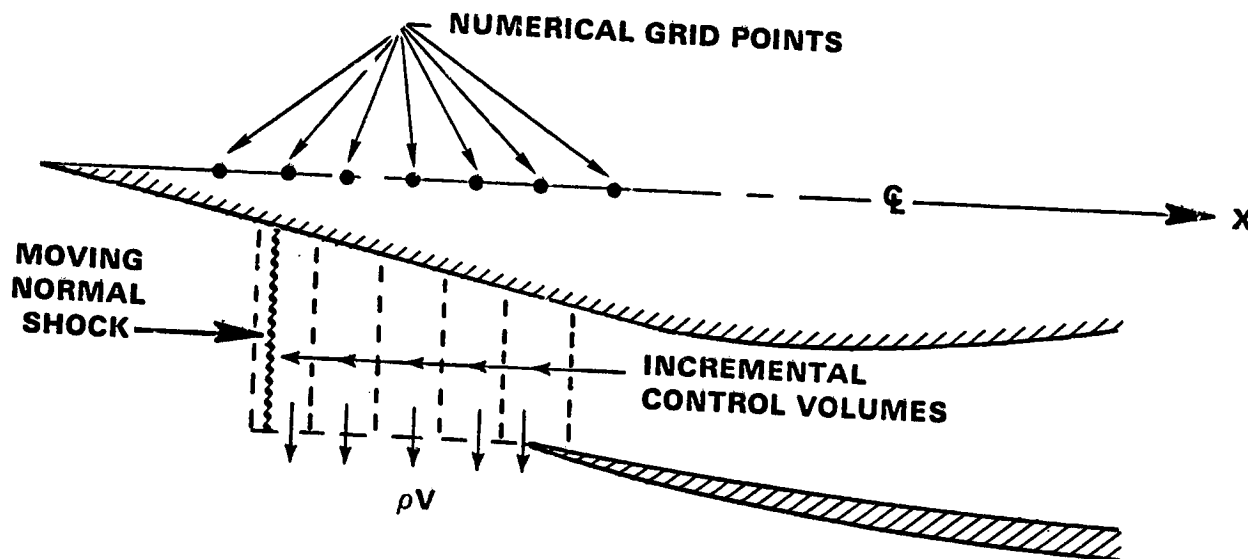


FIGURE 5. INLET UNSTART SCHEMATIC

ORIGINAL PAGE IS  
OF POOR QUALITY

Modeling of the above discussed inlet unstart phenomena is herein accomplished through adaptation of an incremental control volume approach. The Moeckel continuity method (Ref. 3) is used to relate the expelled normal shock position ahead of the inlet cowl to the amount of spilled mass flow over the inlet housing. Details of this approach are explained below.

Appendix A presents a methodology whereby the actual spilled mass flux can be determined in terms of the straight sonic line mass flux and a correction factor  $F$  which is a function of free-stream Mach number only following Moeckel (Ref. 3). This approach is implemented as illustrated in Fig. 6 where the incremental control volumes are formed by the x-direction one-dimensional numerical grid mesh.



**FIGURE 6. ONE-DIMENSIONAL INCREMENTAL CONTROL VOLUME UNSTART MODEL**

The actual spilled mass flux  $\rho^*V$  from each local control volume is determined via a modified form of Eq. (A-3) in Appendix A as

$$\rho^*V = F_c \rho^*V^* \quad (82)$$

with the sonic mass flux  $\rho^*V^*$  given by an isentropic expansion from the local control volume stagnation (total) pressure and stagnation (total) temperature to the local sonic(\*) conditions. The correction

factor  $F_c$  is a modified form of the straight sonic line correction factor  $F$  derived in Appendix A and accounts for inlet unstart variable area effects;  $F_c$  is given by

$$F_c = F \left\{ \left( \frac{2\gamma_c - a_L}{\gamma_c} \right)^j \left( \frac{a_L}{a_I} \right) \left[ \frac{1 - \frac{\rho_I U_I}{\rho_L U_L} \left( \frac{2\gamma_c - a_I}{2\gamma_c - a_L} \right)^j \left( \frac{a_I}{a_L} \right)}{1 - \frac{\rho_I U_I}{\rho_L U_L}} \right] \right\} \quad (83)$$

where  $j=0$  for two-dimensional geometries and  $j=1$  for axisymmetric geometries. The geometry parameters  $\gamma_c$ ,  $a_L$ , and  $a_I$  are defined in Fig. 7 where it is noted that for the special condition  $\gamma_c = a_I/a_L$ , Eq. (83) reduces to  $F_c = F$  which is consistent with the derivation of the straight sonic line correction factor  $F$  per Appendix A.

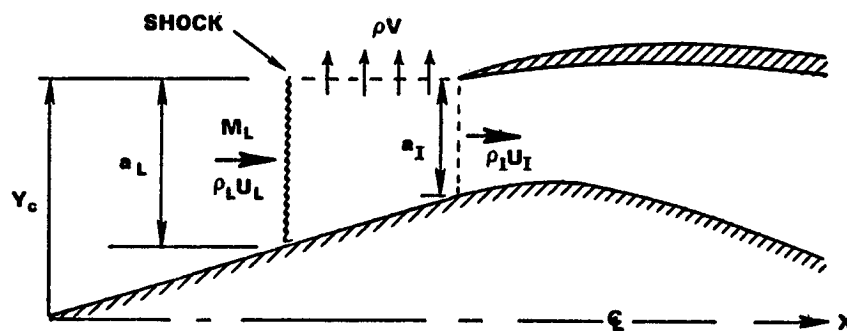


FIGURE 7. MODIFIED CORRECTION FACTOR GEOMETRY PARAMETER DEFINITION

Numerical implementation of the above discussed incremental control volume approach is accomplished by appendage of additional grid points in front of the inlet cowl upon expulsion of the normal shock. The moving normal shock location is determined by monitoring the computed Mach number distribution and interpolating for the Mach one location in the shock jump from supersonic to subsonic. Note that in this one-dimensional approximation, the moving normal shock is assumed normal to the centerbody  $x$ -axis coordinate. Determination of the straight sonic line correction factor  $F$  for use in Eq. (83) is per Fig. (A-1) in Appendix A, with the free-stream Mach number taken to be the local average Mach number in the centerbody inviscid flow field immediately upstream of the normal shock, i.e.,  $M_L$  in Fig. 7. The mass flux  $\rho V$  in Fig. 7 is determined in the exact same manner.  $F$  and  $F_c$  are assumed constant for all control volumes at the values determined above.

Also considered in the incremental control volume analysis are both the momentum flux and energy flux spillage in a manner exactly analogous to the mass flux spillage presented above. Even though the momentum flux is, in reality, transferred out of the system in a normal direction, one-dimensional gas-dynamic theory requires that the momentum be accounted for as if the transfer were accomplished in the tangential direction. This is necessary in order to satisfy the Second Law of Thermodynamics and is discussed on page 234 of Shapiro's book (Ref. 8). Basically, normal mass extraction generates an entropy decrease due to an ambiguity in the quasi-one-dimensional inviscid flow equations.

With the mass, momentum, and energy flux spillage for each individual control volume determined as discussed above, unstart phenomena are modeled through the governing equations of motion (1-3) source/sink terms  $M_s$ ,  $F_s$ , and  $Q_s$ . For example, mass spillage due to inlet unstart is treated locally as a mass sink and incorporated into the continuity equation (1) source/sink term  $M_s$ . In this manner all of the fluid dynamic effects of inlet unstart are properly incorporated into the numerical solution procedure in a totally consistent manner which reflects the local conditions of the flow field. It should be noted that this quasi-steady approach also properly treats combined phenomena which may occur locally, such as mass loss due to spillage and mass loss due to centerbody bleed in the same control volume. In this case the continuity equation (1) source/sink term  $M_s$  would be the sum of the separate spillage and bleed within the control volume. Similar comments apply to the momentum and energy equation source/sink terms  $F_s$  and  $Q_s$ , respectively.

### 3.7 BLEED AND BYPASS MODEL

Inlet bleed and bypass flow rates are computed using the local stagnation (total) pressure and stagnation (total) temperature of the inlet duct flow in conjunction with bleed and bypass flow coefficients from experimental data. For cases where the bleed or bypass flow is not choked, the bleed or bypass plenum conditions (pressure and temperature) are required to determine the flow coefficients. These unchoked plenum conditions are computed by assuming the plenum to be

a single lumped volume with negligible flow velocity and numerically solving two ordinary differential equations for the time-dependent plenum density and temperature; plenum pressure is then determined through the equation of state. The plenum discharge conditions are assumed to be choked flow. A schematic of an inlet bleed system is shown in Fig. 8; an exactly analogous situation applies for an inlet bypass system with bleed flow replaced by bypass flow.

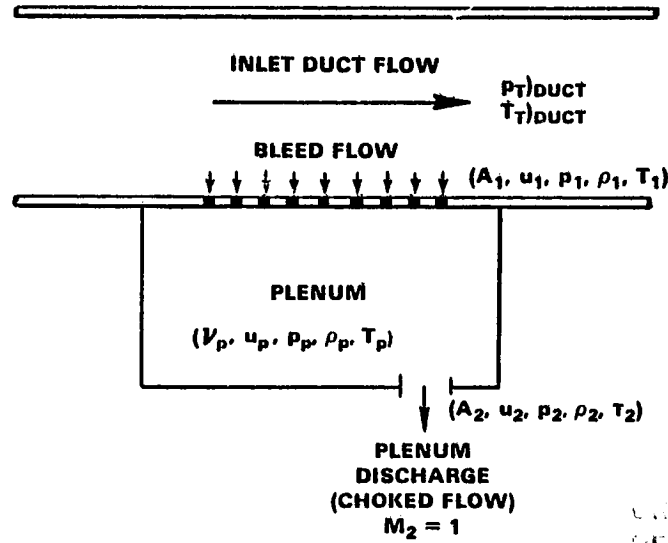


FIGURE 8. INLET BLEED SYSTEM SCHEMATIC

The governing differential equations for the bleed and bypass model are taken from Chapter 2 in the textbook by Zucrow and Hoffman (Ref. 9). Assuming uniform properties inside the constant volume plenum, continuity of mass requires

$$\frac{d\rho_p}{dt} = \frac{1}{V_p} (\rho_1 u_1 A_1 - \rho_2 u_2 A_2) \quad (84)$$

while conservation of energy requires

$$\frac{d}{dt} \left[ \rho_p \left( c_v T_p + \frac{u_p^2}{2} \right) \right] = \frac{1}{V_p} (\rho_1 u_1 A_1 H_1 - \rho_2 u_2 A_2 H_2) \quad (85)$$

ORIGINAL FACILITY  
OF POOR QUALITY

Under the assumption of negligible flow velocity within the plenum ( $u_p = 0$ ) as well as conservation of total enthalpy across flow boundaries, i.e.,

$$\begin{aligned} H_1 &= C_p T_{T_1} = C_p (T_T)_{\text{Duct}} \\ H_2 &= C_p T_{T_2} = C_p T_{T_p} = C_p T_p \end{aligned} \quad (86)$$

Eq. (85) can be written as

$$\frac{dT_p}{dt} = \frac{1}{v_p \rho_p} \left[ (\gamma T_{T_1} - T_p) \rho_1 u_1 A_1 - (\gamma - 1) T_p \rho_2 u_2 A_2 \right] \quad (87)$$

with the substitution of Eq. (84). Given the plenum density and temperature determined via numerical integration (trapezoidal rule) of Eqs. (84) and (87), the plenum pressure is calculated from the equation of state (4) as

$$P_p = \rho_p R T_p \quad (88)$$

Experimental data from Dennard (Ref. 20) and Syberg and Hickcox (Ref. 21) are used to determine the bleed flow coefficients as a function of bleed hole geometry parameters and local inlet duct flow conditions. Unpublished flow coefficient data are used for the bypass flow coefficients. The bleed or bypass flow is determined from the flow coefficient relation

$$\rho_1 u_1 A_1 = K_1 \frac{P_{T_1} A_1}{\sqrt{\gamma R T_{T_1}}} \text{Fun}(\gamma) \quad (89)$$

where it is assumed that

$$\begin{aligned} P_{T_1} &= (P_T)_{\text{Duct}} \\ T_{T_1} &= (T_T)_{\text{Duct}} \end{aligned} \quad (90)$$

and  $\text{Fun}(\gamma)$  is a function of the specific heat ratio only.



The flow coefficient  $K_1$  is the ratio of the actual mass flow through the porous bleed section (or bypass) to the maximum theoretical value for choked flow. It is a function of the following flow and geometry variables:

- Hole length/diameter
- Boundary-layer thickness to hole diameter
- Hole angle
- Hole area to total area (porosity)
- Local Mach number
- Pressure ratio across hole

The present work, limited to inviscid flow considerations, utilizes a table of values for  $K_1$  as a function of hole geometry with local Mach number and pressure ratio as parameters. For the choked flow plenum discharge, the mass flow is given by

$$\rho_2 u_2 A_2 = K_2 \frac{p_{T_2} A_2}{\sqrt{\gamma R T_{T_2}}} \text{Fun}(\gamma) \quad (91)$$

where it is assumed that

$$\begin{aligned} p_{T_2} &= p_p \\ T_{T_2} &= T_{T_p} = T_p \end{aligned} \quad (92)$$

where recall that the flow velocity within the plenum volume is assumed negligible. The flow coefficient  $K_2$  is the choked mass flow coefficient for the plenum exhaust valve which has a typical constant value between 0.9 and 1.0. For the present work,  $K_2$  is taken as constant at the value 0.9.

Initial conditions from which to start the numerical integration of Eqs. (84) and (87) are based upon the condition of steady-state flow through the plenum. Under this restriction, the governing equations become

$$\rho_1 u_1 A_1 = \rho_2 u_2 A_2 \quad (93)$$

$$(T_T)_{\text{Duct}} = T_{T_1} = T_p = T_{T_2} \quad (94)$$

in conjunction with the flow coefficient relations discussed above. This set of algebraic equations is solved iteratively using the secant method. Note that Eq. (94) above simply reflects constancy of total enthalpy under steady-state conditions with negligible flow velocity within the plenum.

### 3.8 EXTERNAL INVISCID FLOW FIELD

The supersonic external inviscid flow field in front of the cowl lip on a mixed compression axisymmetric inlet with a conical centerbody can be analytically treated in an approximate manner using classical aerodynamic analysis techniques. With reference to Fig. 9 for nomenclature, the present work utilizes the following iterative approximation approach to completely determine the supersonic inviscid conical flow field on the sharp cone centerbody:

1. First approximation on the conical shock angle  $\psi_s$  following the hypersonic small disturbance theory of Rasmussen (Ref. 22).

$$\frac{\sin \psi_s}{\sin \delta_c} = \left[ \frac{\gamma+1}{2} + \frac{1}{M_\infty^2 \sin^2 \delta_c} \right]^{\frac{1}{2}} \quad (95)$$

2. Sharp cone surface pressure  $p_c$  specified through the curve fit relation developed by Wittliff (Ref. 23).

$$\frac{p_c - p_\infty}{\frac{1}{2} \rho_\infty V_\infty^2 \sin^2 \delta_c} = 2.10 \left[ 1 + \left( \frac{1.2}{\sqrt{M_\infty^2 - 1} \sin \delta_c} \right)^{2.52} \right]^{0.14} \quad (96)$$

3. Inviscid flow field distributions of static pressure  $p$  and total velocity  $V$  between the cone surface and the shock based on the constant density approximation following Maslen (Ref. 24) which is, in turn, based on Chapter 4 in the book by Hayes and Probstein (Ref. 25).

$$\frac{p - p_c}{p_s - p_c} = \left( \frac{\psi - \psi_c}{\psi_s - \psi_c} \right)^2 \quad (97)$$

$$\frac{V - V_c}{V_s - V_c} = \left( \frac{\psi - \psi_c}{\psi_s - \psi_c} \right)^2 \quad (98)$$

4. Using known conditions at the cone surface and the shock, approximate the local flow angle  $\theta$  distribution through a cubic fit

$$\theta = \psi - \cos^{-1} \left( \frac{u}{V} \right) \quad (99)$$

$$u = a_1 + a_2(\psi - \psi_c)^2 + a_3(\psi - \psi_c)^3 \quad (100)$$

$$a_1 = V_c \quad (101)$$

$$a_2 = \frac{V_s}{2(\psi_s - \psi_c)} - \frac{3a_3(\psi_s - \psi_c)}{2} \quad (102)$$

$$a_3 = \frac{V_s}{(\psi_s - \psi_c)^2} + \frac{2V_c}{(\psi_s - \psi_c)^3} - \frac{2V_\infty \cos \psi_s}{(\psi_s - \psi_c)^3} \quad (103)$$

5. Compare the integrated mass flow between the cone surface and the shock with the corresponding free-stream capture mass flow. Iterate to convergence using the secant method to determine the updated shock angle  $\psi_s$ .

OF 10 21

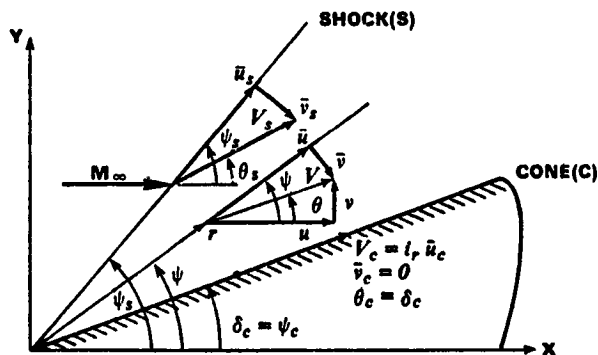


FIGURE 9. INVISCID CONICAL FLOW FIELD NOMENCLATURE

Figure 10 represents a comparison of the present approximate technique relative to exact results from the inviscid conical method, Zucrow and Hoffman (Ref. 9). Here the flow field is for a 10.0 degree semi-vertex angle sharp cone in a Mach 2.50 free-stream flow which is representative of an actual mixed-compression inlet centerbody. Agreement between the approximate and exact techniques is excellent for all flow field variables and shock location.

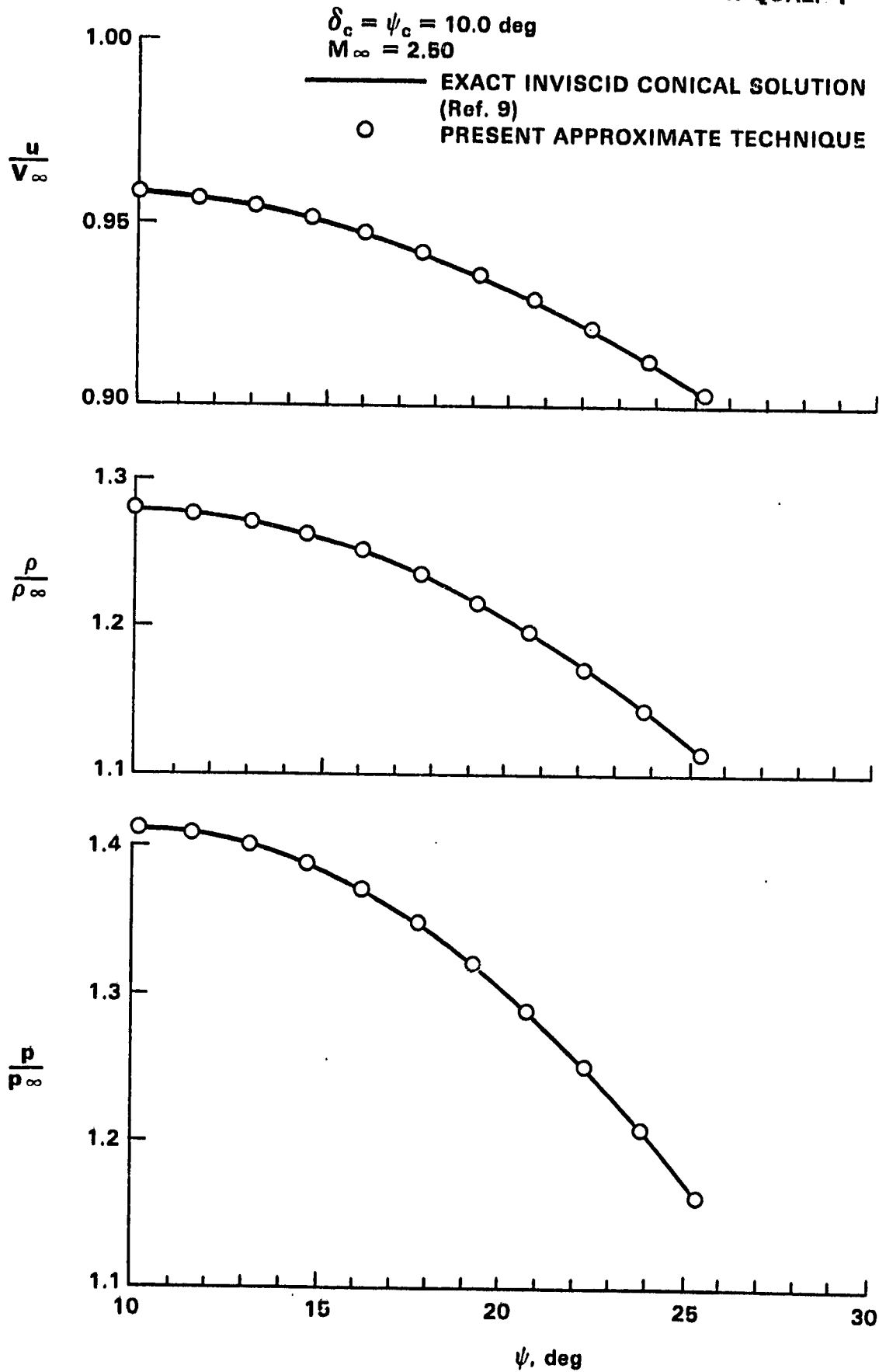


FIGURE 10. INVISCID SHARP CONE FLOW FIELD PROFILES

For the case of a mixed compression axisymmetric inlet with a biconic (fore-aft cone) centerbody, the supersonic external inviscid flow field contains an embedded shock, and the above discussed approximate flow field technique must be modified to reflect this phenomena. With reference to Fig. 11, the following procedure is utilized in the present work to incorporate an embedded shock capability into the approximate conical flow technique:

1. The initial embedded shock angle is determined from classical oblique shock theory based upon the fore cone surface Mach number and the compression angle  $\psi_2 - \psi_c$ . This shock angle is used to determine the shock point "1."
2. Based upon examination of numerous inviscid method of characteristics solutions (using Ref. 26) for various biconic configurations in supersonic flow, it is assumed that the total pressure loss across the embedded oblique shock is the same (i.e., constant) for all embedded shock points. This total pressure loss is determined via the initial shock angle discussed above.
3. With embedded shock point "1" known, determine embedded shock point "2" from the known (constant) total pressure loss and the local upstream flow conditions on the corresponding conical ray.
4. Repeat this formal procedure to "march" the embedded shock points out to point "s" where the embedded shock intersects with the conical shock from the fore cone.
5. Assume the inviscid flow field behind the embedded shock is conical with respect to the virtual origin of the aft cone.
6. "Correct" the local flow field pressures behind the embedded shock by multiplying by the ratio of the aft cone surface pressure (based on inviscid conical flow theory) to the two-dimensional surface pressure (based on oblique shock theory).
7. Compute the remainder of the aft cone inviscid flow field variables using the assumed conical flow field condition in conjunction with an isentropic expansion from conditions immediately behind the embedded shock to the local "corrected" pressure on an aft-cone conical ray.

Figures 12 and 13 show comparisons of the present approximate technique relative to exact results from the inviscid method of characteristics program of Inouye, Rakich, and Lomax (Ref. 26). Here the flow field is for a biconic configuration with a 10.0 degree semi-vertex angle fore cone and a 18.5 degree aft cone in a Mach 2.50 free-stream

OF THE  
OF FLOW

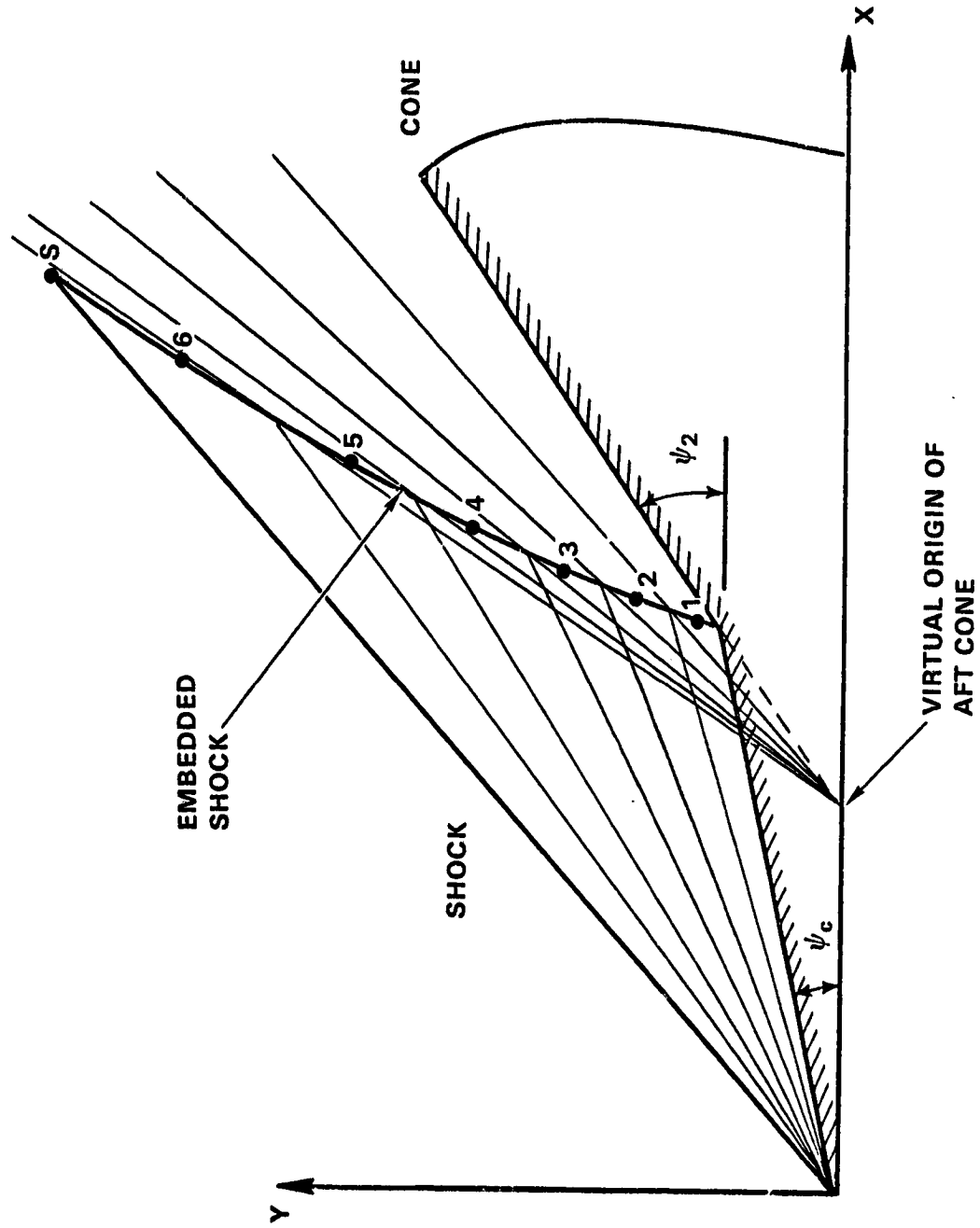


FIGURE 11. INVISCID BICONIC FLOW FIELD NOMENCLATURE

$$M_\infty = 2.50$$

$$\psi_0 = 10.0 \text{ deg}$$

$$\psi_2 = 18.5 \text{ deg}$$

— INVISCID MÉTHOD OF CHARACTERISTICS  
(Ref. 26)

○ PRESENT APPROXIMATE TECHNIQUE

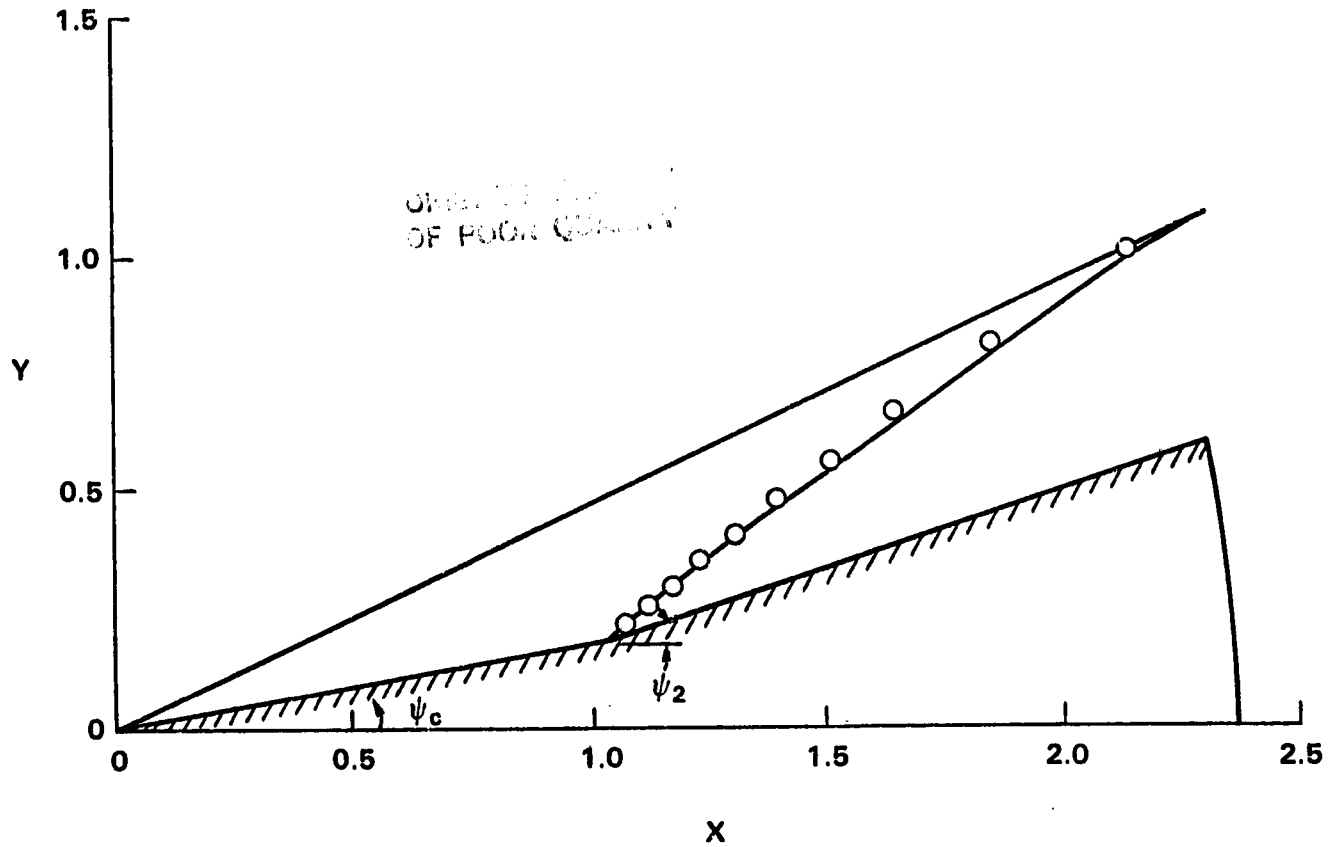


FIGURE 12. INVISCID BICONIC SHOCK WAVE LOCATIONS

ON THE FLOW  
OF POOR QUALITY

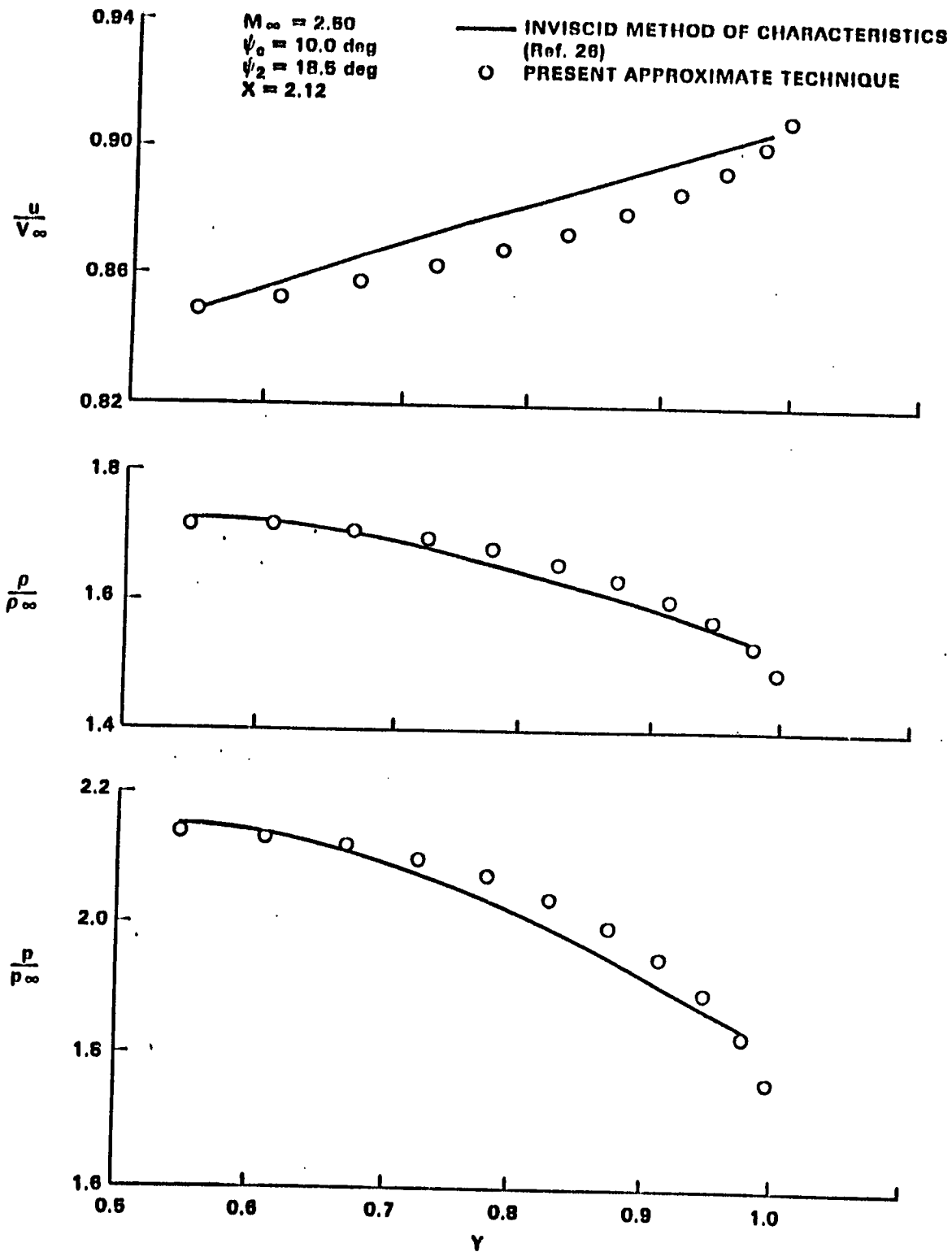


FIGURE 13. INVISCID BICONIC FLOW FIELD PROFILES



flow which is representative of an actual mixed-compression inlet centerbody. As can be seen from Fig. 12, location of the aft-cone-generated embedded shock is reasonably well determined by the approximate technique with the largest discrepancy near the intersection with the fore-cone shock. The comparison of flow field profiles (velocity, density, and static pressure) across the embedded shock layer at x-location of 2.12 is given in Fig. 13, where 10 conical ray intervals have been used across the aft-cone shock layer. Agreement between the approximate technique and the exact method of characteristics solution is good across the entire shock layer, both in distribution and magnitude.

With the profile distribution of flow field properties (velocity, density, and static pressure) across the inviscid shock layer available from the above discussed approximate techniques, it remains to determine equivalent one-dimensional quantities for use as upstream boundary conditions at any plane (see Fig. 14).

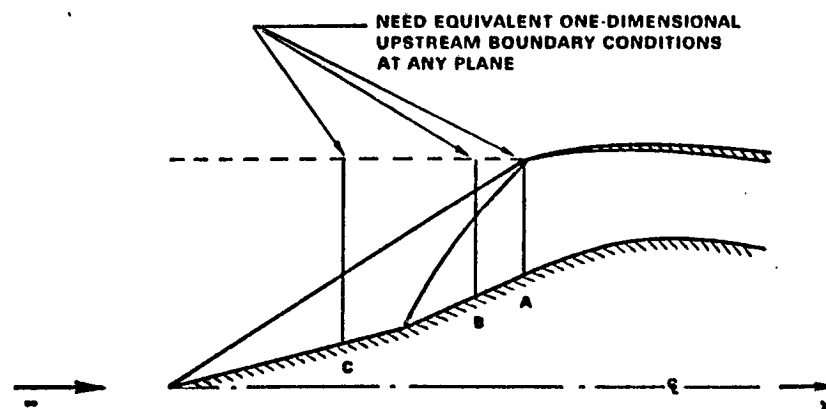


FIGURE 14. UPSTREAM BOUNDARY CONDITIONS

Plane "A" is the appropriate upstream boundary condition for a started inlet while plane "B" and "C" apply to unstarted inlets with an expelled normal shock following the unstart model presented in Section 3.6. Formal integration across any plane normal to the x-axis yields

$$Q_1 = \int_A \rho u dA \quad \text{Mass} \quad (104)$$

$$Q_2 = \int_A (p + \rho uV) dA \quad \text{Momentum} \quad (105)$$

$$Q_3 = \int_A (E + p) u dA \quad \text{Energy} \quad (106)$$

where  $V$  is the total velocity along a streamline and  $u$  is the corresponding velocity component parallel to the  $x$ -axis. In terms of the basic flow variables  $U_1$ ,  $U_2$ , and  $U_3$

$$\hat{Q}_1 = \epsilon_x U_2 \quad (107)$$

$$\hat{Q}_2 = [(\gamma + 1)U_3 + \frac{3 - \gamma}{2} \frac{U_2^2}{U_1}] \epsilon_x \quad (108)$$

$$\hat{Q}_3 = [\gamma U_3 - \frac{\gamma - 1}{2} \frac{U_2^2}{U_1}] \frac{U_2}{U_1} \epsilon_x \quad (109)$$

where  $Q = x_\xi \hat{Q}$ . Solving Eqs. (107), (108), and (109) for  $U_1$ ,  $U_2$ , and  $U_3$  yields

$$U_2 = \frac{\hat{Q}_1}{\epsilon_x} \quad (110)$$

$$\frac{U_1}{U_2} = \frac{-B \pm \sqrt{B^2 - 4AC}}{2A} \quad (111)$$

$$U_3 = \frac{1}{\gamma} \left[ \frac{\hat{Q}_3}{\epsilon_x} \frac{U_1}{U_2} + \frac{\gamma - 1}{2} \frac{U_2^2}{U_1} \right] \quad (112)$$

with

$$A = \frac{\gamma - 1}{\gamma} \frac{\hat{Q}_3}{\epsilon_x} \quad (113)$$

$$B = \frac{-\hat{Q}_2}{\epsilon_x} \quad (114)$$

$$C = \left[ \frac{(\gamma - 1)^2}{2\gamma} + \frac{3 - \gamma}{2} \right] \hat{Q}_2 \quad (115)$$

The choice of sign in the quadratic root of Eq. (111) must be negative (-) in order for the resulting flow to be supersonic; a positive (+) sign results in subsonic flow.

In the case of a two-dimensional multiple ramp external flow, calculation of the flow field is much simpler since straight shocks are generated with uniform flows behind them. The classical inviscid, two-dimensional, oblique shock relations are applied using the secant method to converge an iterative solution process. By using an initial guess to the solution based on small disturbance theory (Ref. 25), convergence is generally obtained in two to four iterations.

The flow field over a downstream ramp is computed using the flow over the preceding ramp as an upstream condition. Up to three straight ramps upstream of the cowl lip are allowed in the formulation.

### 3.9 INITIAL CONDITIONS

In order to provide a consistent flow field from which transient solutions may evolve, initial conditions are required within the inlet and upstream of the inlet for unstarted flow models that are compatible with the governing one-dimensional equations presented in earlier sections and with the engineering flow models that describe the engineering characteristics of the inlet configuration, both in the unstarted and started mode. The initial conditions must include normal shocks within the inlet and normal shocks for the unstarted inlet and also include the double-shock case for the unstarted inlet. Since most flow fields are established based on downstream boundary condition constraints, the initial conditions must use this downstream or exit plane boundary condition information to define the flow field within the inlet for both the unstarted and started inlet cases. Boundary condition constraints as indicated earlier, may be qualified as either pressure, Mach number, or mass flow constraints.

The initial conditions are established within the inlet based on the steady-state one-dimensional isentropic and normal shock compressible flow relations. Using various combinations of these equations in a direct or iterative fashion as required by the boundary condition constraints provides for a number of capabilities. These capabilities

include the steady-state flow field definition for both started and unstarted inlets which are coupled with the external flow field calculations. The unstarted inlet model used in the steady-state initial condition definition is consistent with the unstart model discussed previously. Consistent with the governing equation and engineering model formulations presented in earlier sections, the initial condition routines are generalized to include both two-dimensional or axisymmetric configurations. The initial condition capabilities provide the range of steady-state boundary conditions that define the allowable input bounds for the exit plane boundary conditions and other initial conditions. This range of boundary conditions is an especially important feature of the initial condition routine because the maximum and minimum input bounds are not always obvious. The initial condition routine does not include bleed or bypass modeling. This is not a serious drawback, however, since a given inlet configuration can be started in a mode without bleed or bypass. Bleed or bypass can then be "turned on" and a new steady-state solution can be evolved in time.

As stated in the previous paragraph, both started and unstarted inlet flow fields can be defined using the initial conditions steady-state routines based on the one-dimensional isentropic and normal shock compressible flow relations. Inlets that can be considered are both variable or constant area in configuration. For the started inlet configuration, exit plane constraints such as exit plane pressure, Mach number, or mass flow rate can be imposed or the shock location within a started inlet duct can be defined. All conditions assume, of course, that the flow field at the inlet plane for the started configuration is supersonic. The only restriction on the started inlet configuration is that the shock location must be downstream of the throat.

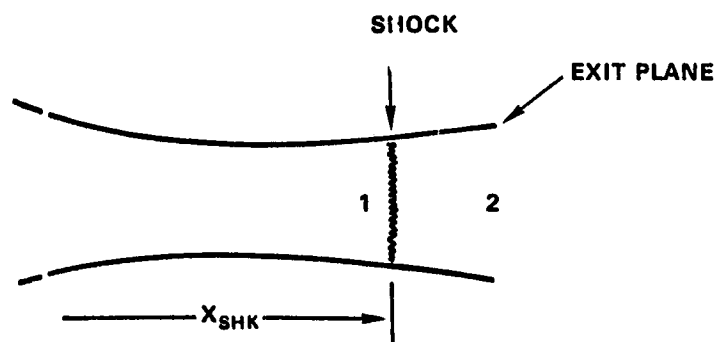
For the unstarted inlet configuration, the freestream flow field must be supersonic in form with exit plane inlet constraints based on exit plane pressure, Mach number, and mass flow rate. As an added capability, the unstarted inlet configuration can be also specified by the

shock location upstream of the inlet plane for the single-shock case and the upstream shock location and the shock location downstream of the throat within the inlet for the double-shock case. The only restriction for the inlet flow field for the unstarted double shock inlet configuration is that subsonic flow must be present at the inlet plane.

The flow field for started inlets with the shock located downstream of the throat is based on the approach given in the textbook by Hall (Ref. 27). In this approach, the exit pressure,  $p_2$ , divided by the upstream stagnation pressure,  $p_{T1}$ , is defined as the exit plane boundary condition constraint. The exit plane Mach number,  $M_2$ , can be determined by application of the equation given below.

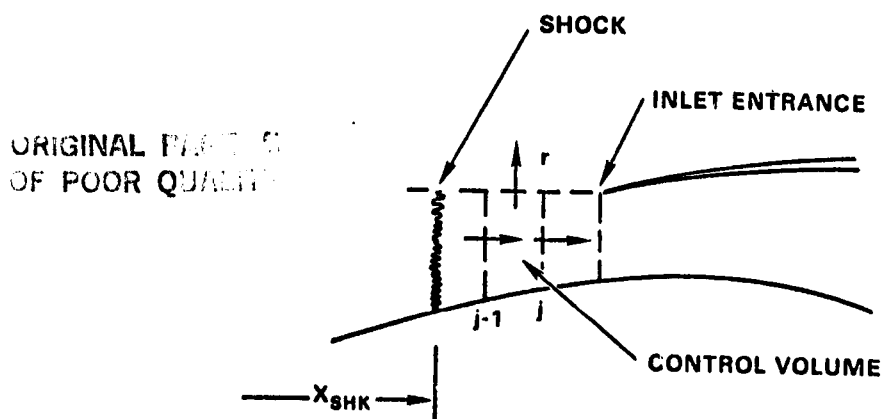
$$\frac{p_2}{p_{T1}} \frac{A_2}{A^*} = \frac{1}{M_2} \left( \frac{2}{\gamma+1} \right)^{\frac{\gamma+1}{2(\gamma-1)}} \left( 1 + \frac{\gamma-1}{2} M_2^2 \right) \quad (116)$$

This equation is derived by eliminating the entropy between the equations for the stagnation pressure for the upstream flow field divided by the exit plane pressure as a function of the exit plane Mach number and the exit plane area,  $A_2$ , as a function of the sonic area,  $A^*$ , and exit plane Mach number,  $M_2$ . The sketch given below shows a schematic of the region 1 and region 2 points for reference.



Once the exit plane Mach number has been defined, isentropic expansion is used to relate the exit plane pressure to the local stagnation pressure in region 2. The Mach number just ahead of the shock front in region 1 is then defined by relating the region 1 Mach number to the ratio of the stagnation pressure in region 2 divided by the stagnation pressure in region 1. Once the Mach number in region 1 is determined, isentropic area expansion can be used to define the cross-sectional area at the shock location as a function of the sonic area. Using the shock location as an internal constraint, the shock location is iterated using the method of steepest descent to satisfy the exit plane boundary conditions whether they be pressure, Mach number, or mass flow rate.

Unstarted inlet initial conditions are handled in much the same way as the started inlet flow field conditions except that the inlet entrance Mach number for unstarted inlets is subsonic. The flow field ahead of the inlet entrance and behind the upstream normal shock is modeled following the unstart modeling concepts presented in previous sections. The grid cells in the region upstream of the inlet entrance are modeled using conservation of mass, momentum, and energy applied in a control volume sense. This leads to relationships describing the pressure and temperature jump across a control volume as shown in the sketch below between nodes  $j-1$  and  $j$ .



The mass flow rate crossing the control volume boundary denoted here as  $r$  is related to the mass flow rate crossing a fictitious boundary whose properties are at the local sonic conditions defined by the Moeckel relationship as given earlier. Equations (117) and (118) describe the temperature pressure relationships for this control volume model which includes a mass bleed across the boundary (denoted with subscript  $r$ ).

$$T_j = T_{j-1} + \frac{(\gamma-1)}{2} u_{j-1}^2 (1-\beta^2) \quad (117)$$

$$p_j = p_{j-1} + \frac{u_{j-1} \dot{m}_{j-1}}{A} (1-\beta) + \frac{\dot{m}_r}{A} u_{j-1} \beta \quad (118)$$

where  $\beta = \frac{u_j}{u_{j-1}}$ .

In a manner similar to the started inlet case, the upstream normal shock location is iterated using the method of steepest descent to satisfy an imposed exit boundary condition whether it be pressure, Mach number, or mass flow rate. The double shock initial condition is established by iterating the shock upstream of the inlet plane until the inlet throat Mach number is exactly unity ( $M = 1.0$ ). A shock downstream of the sonic throat is then allowed to form to satisfy the exit plane boundary condition constraints.

### 3.10 COMPUTER CODE (PROGRAM LAPIN)

A schematic of the computer code (Program LAPIN - Large Perturbation Inlet) is shown in Fig. 15. The program itself is written in FORTRAN IV for execution on a Digital Equipment Corporation VAX-11/780 and contains approximately 6,100 lines of source code. All input is through NAMELIST with an example for the NASA LeRC 40-60 inlet geometry given in Fig. 16. Output from Program LAPIN for a Mach 2.50 free-stream flow and a corrected mass flow exit plane boundary condition is reproduced in Figures 17 through 19. The initial (steady-state) distribution for an unstarted inlet is shown in Fig. 17 while Fig. 18 gives the transient distribution at a time of 0.0240 seconds. Note in Fig. 18 the internal embedded shock at  $x$ -location between 4.8625 and 5.0052 as well as the expelled shock at a  $x$ -location between 1.8649 and 2.0090. These calculations were performed using

ORIGINAL FIGURE  
OF POOR QUALITY

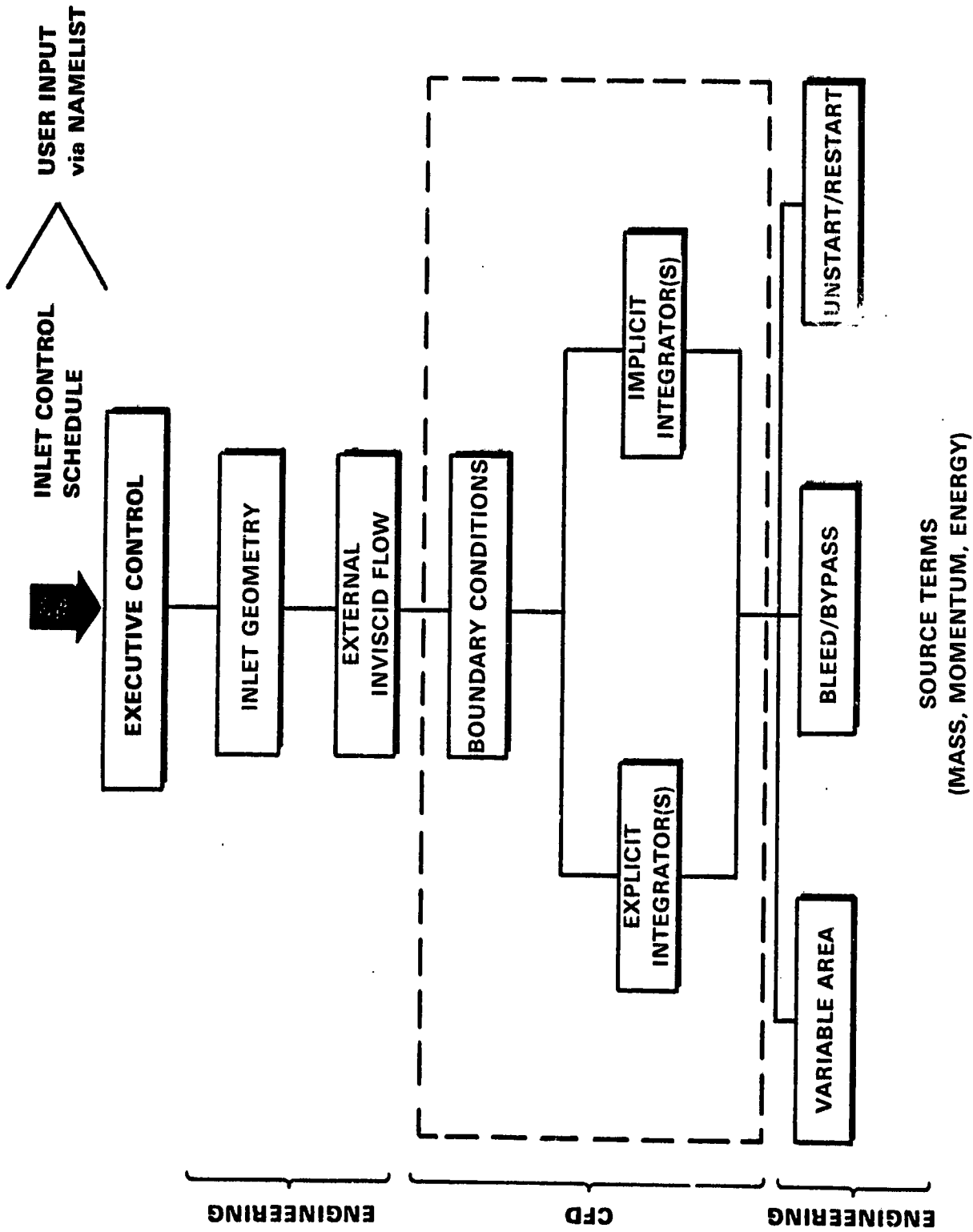


FIGURE 15. SCHEMATIC OF PROGRAM LAPIN (Large Perturbation Inlet)



ORIGINAL  
OF P...

```
***** INPUT DATA MIRROR *****
***** 40-60 INLET ***** UNSTARTED WITH HIGH BYPASS FLOW *****
***** UNSTARTED WITH HIGH BYPASS FLOW *****
SCONTRL SCMC=.TRUE.,NMAX=200,NC=20,TIMAX=.2,OPTPRI=.TRUE.,
TIMOTC=0.0,.2,DTIME=.0002,.0002,NOTC=2, SEND
S8C MHUSIC=2.5,CMOSBC=.TRUE.,CMOSIC=1.374,CHARBC=.TRUE.,
PRUSIC=110.9,THUSIC=253.6,
TIMDS=0.0,.005,100.0,
CMASDS=1.0,1.0,1.0,
START=.FALSE.,OPCOND=.FALSE. SEND
SGEOM XC=0.0,2.009,2.512,3.350,4.384,5.093,5.761,6.235,6.845,7.661,7.946,
YC=1.0,1.0,1.0,960.903,904.918,918.887,862.862,
XC11(3)=2.860,3.650,4.505,5.361,,7.161,
YC11(3)=969.939,902.910,,.879,
XC12(3)=3.178,4.093,4.868,YC12(3)=.972,.913,.903,
DYDXCU(7)=0.00001,DYDXCU(10)=0.00001,
XS=0.0,2.885,3.178,3.435,3.466,3.596,4.294,5.261,5.961,7.061,7.946,
YS=0.0,.640,.691,.708,.708,.697,.623,.481,.357,.239,.23899,
XS11(2)=3.017,3.237,3.543,3.865,4.563,5.461,6.461,
YS11(2)=.667,.700,.702,.670,.588,.444,.285,
YS12(6)=4.120,4.724,5.761,YS12(6)=.644,.566,.396,
DYDXSD(2)=.221695,DYDXSU(4)=0.00001,DYDXSD(5)=0.00001,DYDXSU(10)=0.00001,
XSTRUT=5.261,5.456,5.060,6.260,6.666,6.670,7.274,7.661,7.8,
7.9,8.1,
ASTRUT=0.0,.09,.19,.24,.24,.25,.28,.28,
.28,.28,.28,.19,.06,0.0,0.0,0.0,0.0,
TWOD=.FALSE.,INTYPE=1,
XUSLIM=1.0,XINLET=2.009,XEXIT=7.716,JMAX=41,JINL=8,
IPTRAN=2,TRTIME=0.0,200.,XPTAN=0.0104,0.0104,
COWLR=.7763 SEND
S8YBL NBY=1,8YX=6.235,8YL=0.61,8YPERP=.925,8YPVOL=1.878,8BYTBL=2,
NBL=6,8LX=3.2233,3.68329,3.78329,3.36329,3.59329,3.69329,
8LL=.03092,.013419,.013419,.06591,.013419,.013419,
IBLLOC=1,1,1,2,2,2,
IBLCMK=1,1,1,1,1,1,
IBLTBL=1,1,1,1,1,1,
BLPERP=1.0,1.0,1.0,1.0,1.0,1.0,1.0,
BLPORS=.455,.262,.262,.374,.262,.262,
BLPVOL=3.0,3.0,3.0,3.0,3.0,3.0,
PEBYBC=.TRUE.,PEBLBC=.TRUE.,
TIMBY=0.0,.01,100.0,
PEARBY=.4,.4,.4,
TIMBL=0.0,.1,.2,100.0,
PEARBL=1.0,1.0,1.0,1.0 SEND
***** END DATA INPUT *****
```

FIGURE 16. PROGRAM LAPIN NAMELIST INPUT

ORIGINAL PAGE IS  
OF POOR QUALITY

\*\*\*\*\* UNSTARTED WITH HIGH BYPASS FLOW \*\*\*\*\*

IMPLICIT SPLIT CHARACTERISTICS  
 AXISYMMETRIC - VARIABLES NORMALIZED BY INITIAL UPSTREAM STATIC OR TOTAL CONDITIONS  
 UPSTREAM MACH NUMBER BOUNDARY CONDITION, MMUSIC = 2.500000  
 DOWNSTREAM COR. MASS BOUNDARY CONDITION, CMOSIC = 1.374000  
 N= 0 TIME= 0.0000 SEC

X	RMO	U	T	P	M	CFL	MASS	AREA	PT	TT	CMASS
1.0000	1.2540	0.9601	1.0978	1.3766	2.2909	4.8110	1.0017	0.8320	0.9932	1.0000	1.0086
1.1481	1.2540	0.9601	1.0978	1.3766	2.2909	4.8110	1.0017	0.8320	0.9932	1.0000	1.0086
1.2883	1.2540	0.9601	1.0978	1.3766	2.2909	4.8110	1.0017	0.8320	0.9932	1.0000	1.0086
1.4324	1.2540	0.9601	1.0978	1.3766	2.2909	4.8110	1.0017	0.8320	0.9932	1.0000	1.0086
1.5766	1.2540	0.9601	1.0978	1.3766	2.2909	4.8110	1.0017	0.8320	0.9932	1.0000	1.0086
1.7207	1.2540	0.9601	1.0978	1.3766	2.2909	4.8110	1.0017	0.8320	0.9932	1.0000	1.0086
1.8649	3.9456	0.2853	2.1482	8.4760	0.4867	3.0404	0.9310	0.8269	0.5833	1.0000	1.5960
2.0090	4.2538	0.1688	2.2144	9.4197	0.2836	2.6788	0.5739	0.7993	0.5830	1.0000	0.9844
2.1517	4.2393	0.1758	2.2114	9.3746	0.2956	2.7159	0.5739	0.7700	0.5830	1.0000	0.9844
2.2943	4.2216	0.1841	2.2077	9.3198	0.3097	2.7432	0.5739	0.7386	0.5830	1.0000	0.9844
2.4370	4.1997	0.1938	2.2031	9.2521	0.3264	2.7752	0.5739	0.7052	0.5830	1.0000	0.9844
2.5797	4.1696	0.2064	2.1967	9.1595	0.3482	2.8168	0.5739	0.6668	0.5830	1.0000	0.9844
2.7224	4.1248	0.2240	2.1873	9.0221	0.3787	2.8743	0.5739	0.6211	0.5830	1.0000	0.9844
2.8650	4.0593	0.2477	2.1733	8.8222	0.4200	2.9511	0.5739	0.5708	0.5830	1.0000	0.9844
3.0077	3.9639	0.2789	2.1527	8.5333	0.4753	3.0514	0.5739	0.5190	0.5830	1.0000	0.9844
3.1504	3.8390	0.3158	2.1253	8.1593	0.5415	3.1680	0.5739	0.4734	0.5830	1.0000	0.9844
3.2931	3.6609	0.3629	2.0853	7.6343	0.6283	3.3147	0.5739	0.4319	0.5830	1.0000	0.9844
3.4357	3.5053	0.4006	2.0494	7.1837	0.6996	3.4298	0.5739	0.4087	0.5830	1.0000	0.9844
3.5784	3.4693	0.4089	2.0410	7.0806	0.7156	3.4551	0.5739	0.4045	0.5830	1.0000	0.9844
3.7211	3.4847	0.4054	2.0446	7.1249	0.7087	3.4443	0.5739	0.4063	0.5830	1.0000	0.9844
3.8638	3.5028	0.4012	2.0488	7.1768	0.7006	3.4315	0.5739	0.4084	0.5830	1.0000	0.9844
4.0064	3.5345	0.3937	2.0562	7.2678	0.6864	3.4089	0.5739	0.4124	0.5830	1.0000	0.9844
4.1491	3.5887	0.3807	2.0688	7.4244	0.6618	3.3694	0.5739	0.4200	0.5830	1.0000	0.9844
4.2918	3.6660	0.3617	2.0865	7.6490	0.6260	3.3108	0.5739	0.4328	0.5830	1.0000	0.9844
4.4345	3.7507	0.3398	2.1056	7.8976	0.5855	3.2432	0.5739	0.4503	0.5830	1.0000	0.9844
4.5771	3.8331	0.3174	2.1240	8.1417	0.5445	3.1732	0.5739	0.4716	0.5830	1.0000	0.9844
4.7198	3.9037	0.2972	2.1396	8.3524	0.5079	3.1093	0.5739	0.4947	0.5830	1.0000	0.9844
4.8625	3.9635	0.2791	2.1527	8.5321	0.4755	3.0517	0.5739	0.5189	0.5830	1.0000	0.9844
5.0052	4.0137	0.2630	2.1635	8.6837	0.4471	3.0005	0.5739	0.5436	0.5830	1.0000	0.9844
5.1478	4.0574	0.2484	2.1729	8.8163	0.4212	2.9532	0.5739	0.5695	0.5830	1.0000	0.9844
5.2905	4.0907	0.2366	2.1800	8.9177	0.4007	2.9153	0.5739	0.5929	0.5830	1.0000	0.9844
5.4332	4.0956	0.2348	2.1811	8.9328	0.3975	2.9095	0.5739	0.5967	0.5830	1.0000	0.9844
5.5759	4.1008	0.2329	2.1822	8.9487	0.3942	2.9033	0.5739	0.6008	0.5830	1.0000	0.9844
5.7185	4.1122	0.2288	2.1846	8.9834	0.3869	2.8897	0.5739	0.6101	0.5830	1.0000	0.9844
5.8612	4.1275	0.2230	2.1879	9.0304	0.3769	2.8709	0.5739	0.6236	0.5830	1.0000	0.9844
6.0039	4.1478	0.2151	2.1921	9.0927	0.3633	2.8453	0.5739	0.6431	0.5830	1.0000	0.9844
6.1466	4.1592	0.2106	2.1945	9.1276	0.3554	2.8305	0.5739	0.6551	0.5830	1.0000	0.9844
6.2892	4.1622	0.2094	2.1952	9.1367	0.3534	2.8266	0.5739	0.6584	0.5830	1.0000	0.9844
6.4319	4.1562	0.2118	2.1939	9.1183	0.3575	2.8345	0.5739	0.6519	0.5830	1.0000	0.9844
6.5746	4.1533	0.2130	2.1933	9.1095	0.3595	2.8382	0.5739	0.6488	0.5830	1.0000	0.9844
6.7173	4.1484	0.2149	2.1923	9.0943	0.3629	2.8446	0.5739	0.6437	0.5830	1.0000	0.9844
6.8599	4.1423	0.2173	2.1910	9.0757	0.3670	2.8524	0.5739	0.6376	0.5830	1.0000	0.9844
7.0026	4.1412	0.2177	2.1907	9.0722	0.3678	2.8538	0.5739	0.6365	0.5830	1.0000	0.9844
7.1453	4.1319	0.2213	2.1888	9.0438	0.3740	2.8655	0.5739	0.6276	0.5830	1.0000	0.9844
7.2880	4.1332	0.2208	2.1890	9.0477	0.3731	2.8639	0.5739	0.6288	0.5830	1.0000	0.9844
7.4306	4.1452	0.2162	2.1916	9.0844	0.3651	2.8487	0.5739	0.6404	0.5830	1.0000	0.9844
7.5733	4.1661	0.2079	2.1960	9.1487	0.3507	2.8215	0.5739	0.6628	0.5830	1.0000	0.9844
7.7160	4.1853	0.1999	2.2000	9.2078	0.3369	2.7954	0.5739	0.6859	0.5830	1.0000	0.9844

FIGURE 17. PROGRAM LAPIN INITIAL CONDITIONS OUTPUT

ORIGINAL FILED  
OF POOR QUALITY

N	X	TIME=	0.0240 SEC	U	T	P	M	CFL	MASS	AREA	PT	TT	CHASS
1.0000	1.2799		0.9569	1.1065	1.4162	2.2743	4.8057	1.0016	0.8178	0.9955	1.0005	1.0064	
1.1441	1.2799		0.9569	1.1065	1.4162	2.2743	4.8057	1.0016	0.8178	0.9955	1.0005	1.0064	
1.2883	1.2799		0.9569	1.1065	1.4162	2.2743	4.8057	1.0016	0.8178	0.9955	1.0005	1.0064	
1.4324	1.2799		0.9569	1.1065	1.4162	2.2743	4.8057	1.0016	0.8178	0.9955	1.0005	1.0064	
1.5766	1.2799		0.9569	1.1065	1.4162	2.2743	4.8057	1.0016	0.8178	0.9955	1.0005	1.0064	
1.7207	1.2799		0.9569	1.1065	1.4162	2.2743	4.8057	1.0016	0.8178	0.9955	1.0005	1.0064	
1.8649	2.1190		0.6565	1.6375	3.4697	1.2826	4.0755	1.1377	0.8178	0.5495	1.0005	1.0064	
2.0090	4.1990		0.2514	2.1721	9.1208	0.4264	2.9483	0.8037	0.7993	0.6049	1.0005	2.0360	
2.1517	4.3470		0.2049	2.1986	9.5574	0.3454	2.8123	0.6857	0.7700	0.6075	1.0005	1.3951	
2.2943	4.3511		0.2149	2.1934	9.4780	0.3627	2.8449	0.6857	0.7386	0.6075	1.0005	1.1290	
2.4370	4.2890		0.2267	2.1869	9.3795	0.3833	2.8836	0.6857	0.7052	0.6075	1.0005	1.1290	
2.5797	4.2444		0.2423	2.1777	9.2831	0.4105	2.9341	0.6857	0.6668	0.6075	1.0005	1.1290	
2.7224	4.1767		0.2643	2.1638	9.0374	0.4493	3.0052	0.6857	0.6211	0.6075	1.0005	1.1290	
2.8650	4.0747		0.2948	2.1425	8.7298	0.5036	3.1024	0.6857	0.5708	0.6075	1.0005	1.1290	
3.0077	3.9175		0.3372	2.1089	8.2617	0.5826	3.2357	0.6857	0.5190	0.6076	1.0005	1.1289	
3.1504	3.6863		0.3930	2.0581	7.5867	0.6848	3.4072	0.6857	0.4734	0.6077	1.0005	1.1287	
3.2931	3.3171		0.4713	1.9735	6.5462	0.8387	3.6412	0.6752	0.4319	0.6073	1.0005	1.1121	
3.4357	2.9519		0.5426	1.8631	5.5387	0.9885	3.8466	0.6546	0.4087	0.6077	1.0005	1.0775	
3.5784	2.6786		0.5937	1.8105	4.8495	1.1031	3.9892	0.6433	0.4045	0.6084	1.0005	1.0577	
3.7211	2.5426		0.6183	1.7732	4.5086	1.1608	4.0562	0.6387	0.4063	0.6083	1.0005	1.0503	
3.8638	2.4430		0.6363	1.7450	4.2629	1.2043	4.1047	0.6349	0.4084	0.6084	1.0005	1.0438	
4.0064	2.3672		0.6499	1.7231	4.0789	1.2378	4.1409	0.6345	0.4124	0.6084	1.0005	1.0431	
4.1491	2.2939		0.6702	1.6896	3.8083	1.2890	4.1943	0.6345	0.4200	0.6084	1.0005	1.0431	
4.2918	2.1915		0.6975	1.6429	3.4526	1.3605	4.2651	0.6345	0.4328	0.6085	1.0005	1.0430	
4.4345	1.9388		0.7268	1.5908	3.0842	1.4407	4.3394	0.6345	0.4503	0.6085	1.0005	1.0430	
4.5771	1.7403		0.7556	1.5374	2.7371	1.5235	4.4108	0.6345	0.4716	0.6085	1.0005	1.0429	
4.7198	1.6420		0.7811	1.4885	2.4441	1.6066	4.4726	0.6345	0.4947	0.6086	1.0005	1.0429	
4.8625	1.5216		0.8037	1.4438	2.1969	1.6721	4.5261	0.6345	0.5189	0.6086	1.0005	1.0428	
5.0052	1.4247		0.8341	1.3925	1.9694	1.7704	4.5148	0.6737	0.5436	0.4907	0.9858	1.3631	
5.1478	1.3262		0.8358	1.3485	1.7013	1.8781	3.2304	0.6361	0.5695	0.5148	0.9998	1.2355	
5.2905	1.2375		0.8168	1.2929	1.5046	1.9435	3.1709	0.6363	0.5929	0.5147	0.9996	1.2355	
5.4332	1.1491		0.8141	1.2459	1.2195	2.0385	3.1622	0.6364	0.5967	0.5147	0.9996	1.2362	
5.5759	1.0550		0.8112	1.2080	0.9258	2.1533	3.1530	0.6366	0.6008	0.5146	0.9996	1.2366	
5.7185	0.9249		0.8047	1.1328	0.6304	2.3216	3.1326	0.6367	0.6101	0.5146	0.9995	1.2369	
5.8612	0.8516		0.7959	1.0392	0.3838	2.5058	3.1046	0.6364	0.6236	0.5146	0.9994	1.2372	
6.0039	0.8063		0.7841	0.9476	0.1476	2.7047	3.0671	0.6370	0.6431	0.5146	0.9993	1.2375	
6.1466	0.8053		0.7775	0.8521	0.0429	2.929	3.0458	0.6372	0.6551	0.5146	0.9992	1.2378	
6.2892	0.8050		0.7682	0.7582	0.0456	3.1664	3.0160	0.6236	0.6584	0.5146	0.9991	1.2113	
6.4319	0.8051		0.7558	0.6661	0.4344	3.4344	2.9761	0.5944	0.6519	0.5146	0.9991	1.1546	
6.5746	0.8028		0.7411	0.5887	0.4087	3.7632	2.9286	0.5636	0.6488	0.5145	0.9990	1.0948	
6.7173	0.8033		0.7278	0.5278	0.3855	4.0855	2.8854	0.5330	0.6437	0.5145	0.9989	1.0354	
6.8599	0.8040		0.7197	0.4793	0.3714	4.429	2.8590	0.5119	0.6376	0.5145	0.9988	0.9944	
7.0026	0.8057		0.7172	0.4371	0.3671	4.785	2.8509	0.5060	0.6365	0.5144	0.9988	0.9830	
7.1453	0.8051		0.7209	0.3924	0.3735	5.151	2.8626	0.5062	0.6276	0.5144	0.9987	0.9836	
7.2880	0.8052		0.7205	0.3481	0.3727	5.526	2.8612	0.5063	0.6288	0.5144	0.9986	0.9836	
7.4306	0.8034		0.7159	0.3048	0.3648	5.911	2.8461	0.5065	0.6404	0.5144	0.9985	0.9839	
7.5733	0.8022		0.7076	0.2624	0.3505	6.305	2.8189	0.5066	0.6628	0.5144	0.9984	0.9841	
7.7160	0.8098		0.1997	2.1960	6.1248	6.3369	2.7928	0.5069	0.6859	0.5144	0.9982	0.9844	

FIGURE 18. PROGRAM LAPIN TRANSIENT OUTPUT

the implicit split characteristics algorithm with 41 grid points within the inlet ( $2.0090 \leq X \leq 7.7160$ ) and 7 grid points on the unstarted centerbody ( $1.0000 \leq x \leq 2.0090$ ). The corresponding bypass plenum summary output for this case is given in Fig. 19.

BYPASS PLENUM SUMMARY - VARIABLES NORMALIZED BY INITIAL UPSTREAM TOTAL OR CAPTURE CONDITIONS

N	NBY	PP	TP	PTAVE	TTAVE	AREAEX	MACHAVE	MASSIN	MASSOUT	DISFAC
1	1	0.5441	0.9998	0.5830	1.0000	0.4000	0.3593	0.1611	0.1604	0.1023
20	1	0.4646	0.9569	0.5278	0.9718	0.4000	0.4199	0.1245	0.1435	0.0861
40	1	0.4674	0.9645	0.5370	0.9647	0.4000	0.4262	0.1362	0.1438	0.0922
60	1	0.4605	0.9673	0.5270	0.9889	0.4000	0.4139	0.1364	0.1415	0.0952
80	1	0.4525	0.9767	0.5207	0.9963	0.4000	0.4193	0.1378	0.1384	0.0978
100	1	0.4491	0.9842	0.5168	0.9958	0.4000	0.4204	0.1383	0.1368	0.0988
120	1	0.4473	0.9904	0.5147	0.9990	0.4000	0.4214	0.1332	0.1358	0.0957
140	1	0.4459	0.9940	0.5125	0.9988	0.4000	0.4230	0.1256	0.1351	0.0906
160	1	0.4439	0.9956	0.5111	0.9992	0.4000	0.4235	0.1359	0.1344	0.0983
180	1	0.4440	0.9976	0.5109	1.0000	0.4000	0.4232	0.1295	0.1343	0.0938
200	1	0.4435	0.9987	0.5107	1.0004	0.4000	0.4234	0.1374	0.1341	0.0996

U.S. GOVERNMENT PRINTING OFFICE: 1964 O 344-000

FIGURE 19. PROGRAM LAPIN BYPASS PLENUM SUMMARY OUTPUT

#### 4.0 ALGORITHM VERIFICATION

In order to assess the relative accuracy and solution fidelity of each of the algorithms discussed in the previous sections, an analysis is presented for the unsteady normal shock wave in a constant area duct. The five algorithms examined are the Beam-Warming, Hybrid Beam-Warming, split flux, split characteristic, and the explicit MacCormack solution scheme. The moving normal shock in a constant area duct problem was chosen as the basis for algorithm verification because exact analytical closed-form solutions are available for shock speed, as well as flow properties downstream of the shock front.

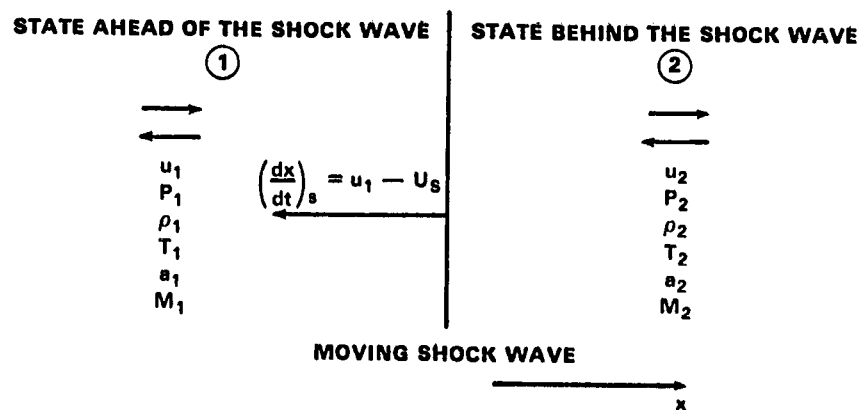
By following Chapter 8 in the textbook by Owczarek (Ref. 28), it can be shown that the speed of the moving shock wave relative to the gas into which it is moving is given by

$$\frac{U_s}{a_1} = \frac{1}{2} \left[ \frac{\gamma+1}{2} \beta M_1 + \sqrt{\left(\frac{\gamma+1}{2}\right)^2 \beta^2 M_1^2 + 4} \right] \quad (119)$$

with

$$\beta = 1 - \frac{u_2}{u_1} = 1 - \frac{\rho_2 u_2}{\rho_1 u_1} \quad (120)$$

where subscript "1" denotes upstream conditions into which the shock is moving, and subscript "2" denotes downstream conditions behind the shock per the following sketch.



Auxiliary relations include

$$\frac{u_2 - u_1}{a_1} = \frac{2}{\gamma+1} \left( \frac{-U_s}{a_1} + \frac{a_1}{U_s} \right) \quad (121)$$

$$\frac{p_2}{p_1} = 1 + \frac{2\gamma}{\gamma+1} \left[ \left( \frac{U_s}{a_1} \right)^2 - 1 \right] \quad (122)$$

ORIGINAL SOURCE IS  
OF POOR QUALITY

$$\frac{T_2}{T_1} = \frac{\frac{p_2}{p_1} + \frac{\gamma+1}{\gamma-1}}{\frac{\gamma+1}{\gamma-1} + \frac{p_2}{p_1}} \quad (123)$$

$$\frac{\rho_2}{\rho_1} = \frac{\gamma+1}{\gamma-1 + 2 \left( \frac{a_1}{U_s} \right)^2} \quad (124)$$

$$M_2 = \frac{M_1 + \frac{2}{\gamma+1} \left[ \frac{a_1}{U_s} - \frac{U_s}{a_1} \right]}{\sqrt{\frac{T_2}{T_1}}} \quad (125)$$

$$\frac{T_{O2}}{T_{O1}} = \left( \frac{T_2}{T_1} \right) \left[ \frac{1 + \frac{\gamma-1}{2} M_2^2}{1 + \frac{\gamma-1}{2} M_1^2} \right] \quad (126)$$

$$\frac{P_{O2}}{P_{O1}} = \left( \frac{p_2}{p_1} \right) \left[ \frac{\left( \frac{T_{O2}}{T_{O1}} \right)}{\left( \frac{T_2}{T_1} \right)} \right] \left( \frac{\gamma}{\gamma-1} \right) \quad (127)$$

with the shock speed given by

$$\left( \frac{dx}{dt} \right)_s = u_1 - U_s \quad (128)$$

and thus

$$M_s = \frac{\left( \frac{dx}{dt} \right)}{a_1} s \quad (129)$$

For a given ratio of downstream to upstream mass flux  $\left( \frac{\rho_2 u_2}{\rho_1 u_1} \right)$ , the above equations can be solved iteratively to yield the moving shock speed as well as all downstream shock parameters. This provides an excellent test case for any one-dimensional unsteady inviscid numerical technique in that the moving normal shock in a constant area duct can be generated by a step-jump reduction in mass flow rate.

Presented in Table 1 are calculated flow parameters from the above equations for the case of a Mach 2.0 upstream condition with a 20 percent reduction in mass flow. Shown enclosed in ( ) are the corresponding stationary normal shock values for a Mach 2.0 flow. As is obvious from the table, the moving shock wave causes substantial changes in shock-jump conditions, including an almost seven percent increase in total temperature.

Presented in Figs. 20 and 21 are the computed results for a Courant number of 0.7 at a time of 0.0050 seconds after flow initiation with a step jump reduction in mass flow at time zero as a prescribed downstream boundary condition. The upstream static temperature was taken to be 300°K (540°R) which results in the moving shock being located at a distance of 0.7365 based upon the shock Mach number given by Eq. (129). This distance location should be used by the reader to access shock speed performance of the various algorithms. As can be seen by comparing the results for the five different methods as described in the numerical algorithms section given earlier, all methods give relatively good shock speed results based on the analytical shock location of 0.7365 as indicated in the previous paragraph. Referring to these figures, it is difficult to determine the exact shock location for each method because of shock smearing.

Some general conclusions can be drawn from these figures, however, to highlight the important features of the methods. Comparing the smoothness of each of the calculations, the split characteristics solution



**TABLE 1. UNSTEADY NORMAL SHOCK WAVE IN A CONSTANT AREA DUCT**

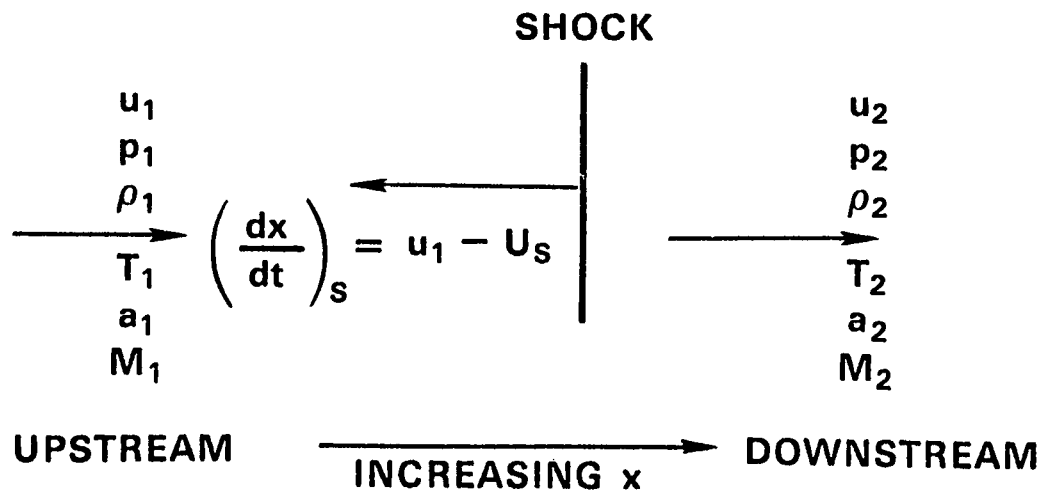
$$M_1 = 2.0 \qquad \frac{\dot{m}_2}{\dot{m}_1} = \frac{\rho_2 u_2}{\rho_1 u_1} = 0.80 \quad (1.0)$$

$$\frac{p_2}{p_1} = 5.5022 \quad (4.500) \qquad \frac{T_2}{T_1} = 1.8607 \quad (1.688)$$

$$\frac{\rho_2}{\rho_1} = 2.9571 \quad (2.667) \qquad \frac{u_2}{u_1} = 0.2705 \quad (0.375)$$

$$M_2 = 0.3967 \quad (0.5774) \qquad M_s = -0.2043 \quad (0.0)$$

$$\frac{P_{02}}{P_{01}} = 0.7838 \quad (0.7209) \qquad \frac{T_{02}}{T_{01}} = 1.0662 \quad (1.0)$$



ORIGINAL INTENT  
OF POOR QUALITY

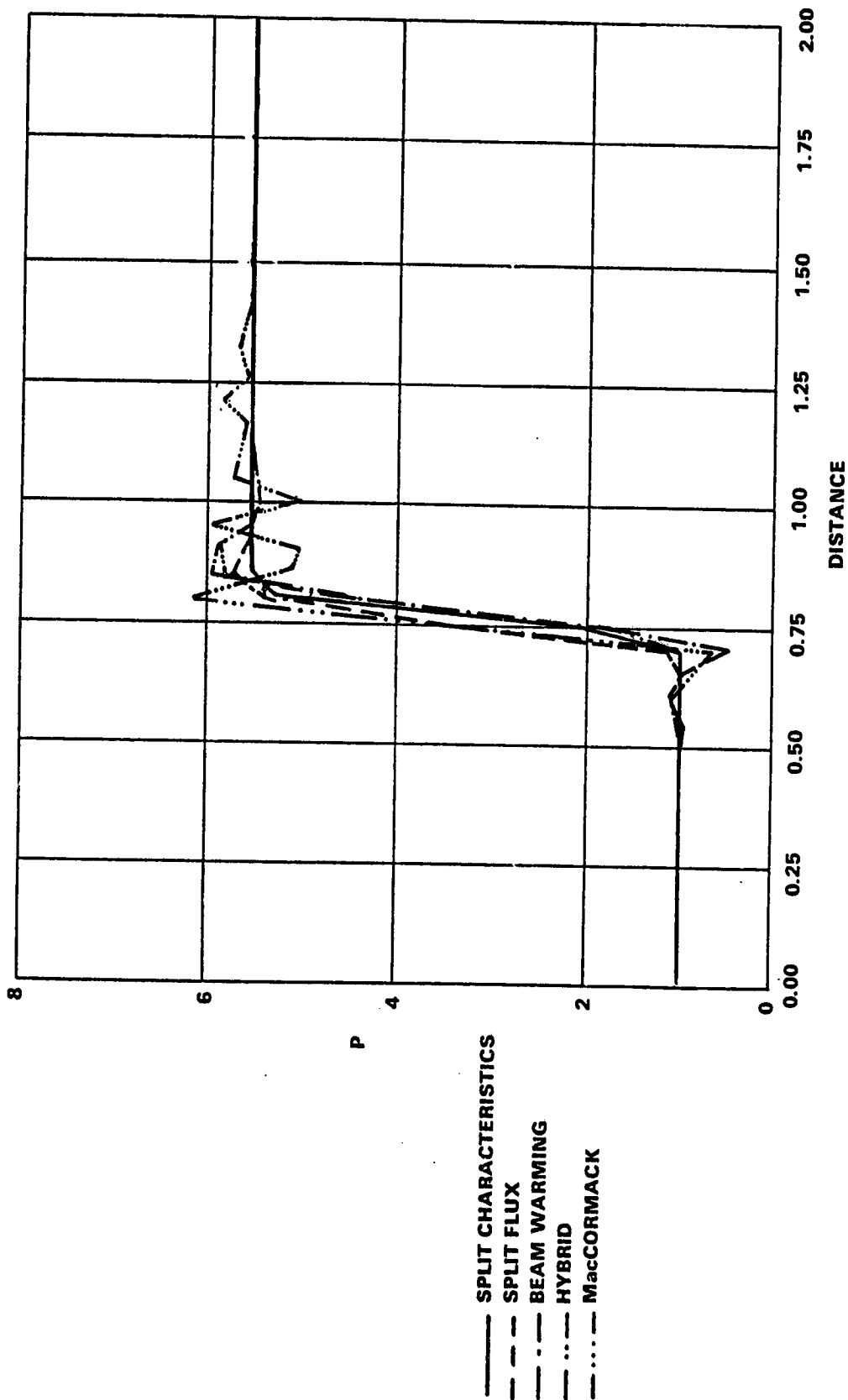


FIGURE 20. PRESSURE-DISTANCE HISTORY AT TIME=0.005 SEC  
FOR AN UNSTEADY SHOCK IN A CONSTANT AREA DUCT

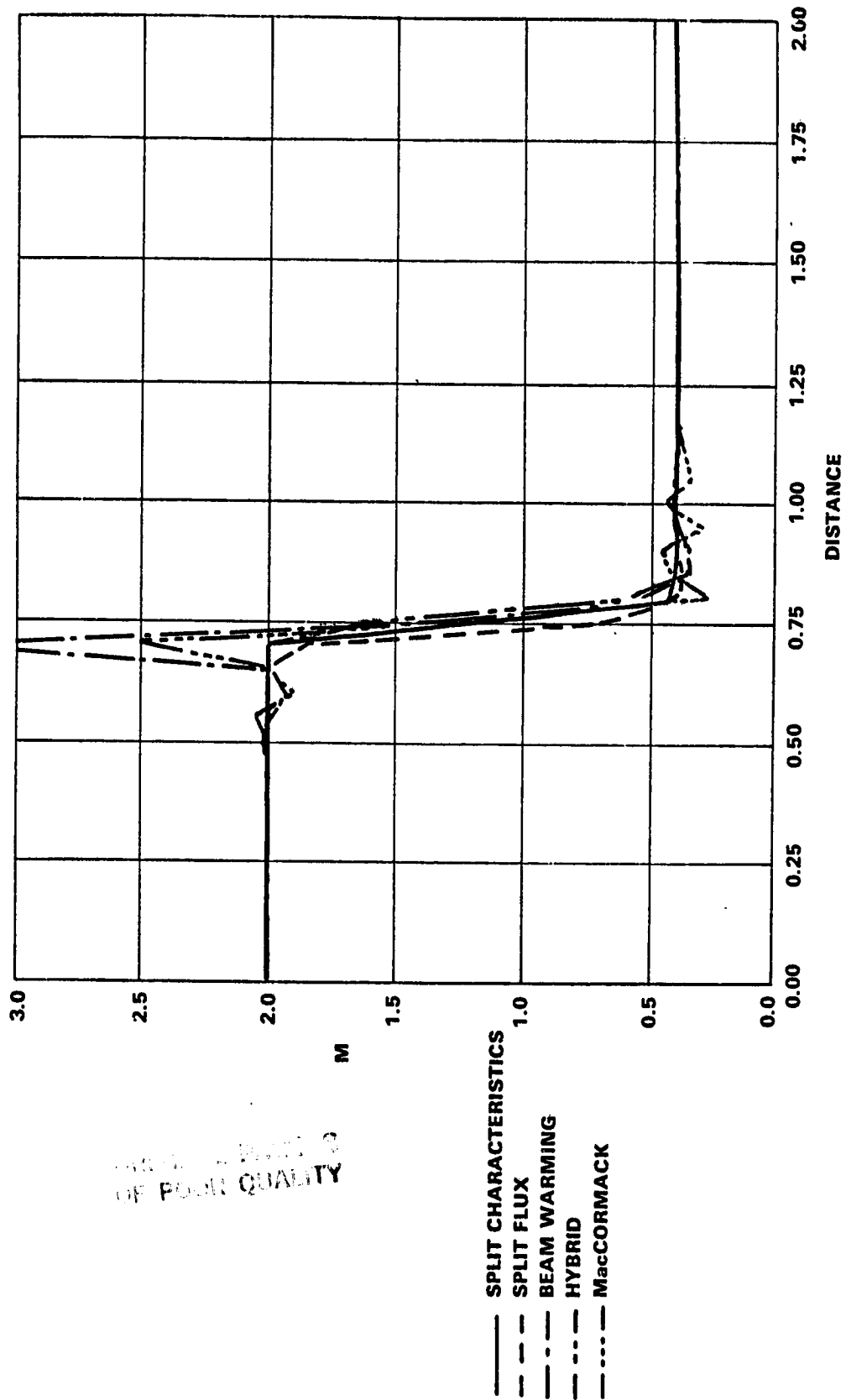


FIGURE 21. MACH NUMBER-DISTANCE HISTORY AT TIME=0.005 SEC  
 FOR AN UNSTEADY SHOCK IN A CONSTANT AREA DUCT

NOT TO BE USED  
 OF POOR QUALITY

scheme is shown to provide the cleanest or highest fidelity numerical solution for this shock tube problem. This solution exhibits no numerical or solution noise in contrast to the other four methods which do exhibit some form of numerical noise. The split flux algorithm solution, when compared to the split characteristic technique, gives nominally good results with some overshoot in pressure just downstream of the shock location. The hybrid scheme as compared to the split flux scheme gives nominally the same result except that the overshoot downstream of the shock is somewhat greater. It must be remembered that the hybrid scheme results include a conservative fourth-order dissipation which must be adjusted based upon a local Courant number condition. The Beam-Warming and MacCormack schemes display significant solution noise, both upstream and downstream of the shock location when compared to the split characteristic, split flux, or Beam-Warming hybrid schemes. The upstream undershoot in the pressure for both the Beam-Warming and MacCormack schemes generally result in algorithm failure for stronger shock calculations.

Similar sets of calculations have been performed for a parabolic 2-1-2 nozzle configuration with an inlet Mach number of 2 and Courant number of 0.8 with comparable results for the shock tracking capability of each of the schemes. Calculations have also been made for the 2-1-2 nozzle to assess Courant number effects on shock tracking and fidelity capabilities of each of the numerical schemes for a hammershock case. These studies show that the split flux and hybrid schemes give little solution deterioration for Courant numbers as high as 6. The split characteristics scheme could be pushed, however, to Courant number values as high as 10 for the hammershock case. For reference purposes, the hammershock was moving at approximately one grid cell per time step at a Courant number of 12. Thus, both the split flux and split characteristics schemes can be utilized with confidence under hammershock transient conditions as long as the Courant number constraint is imposed providing at least two time-step calculations per grid cell movement of the shock.

## 5.0 RESULTS AND DISCUSSION

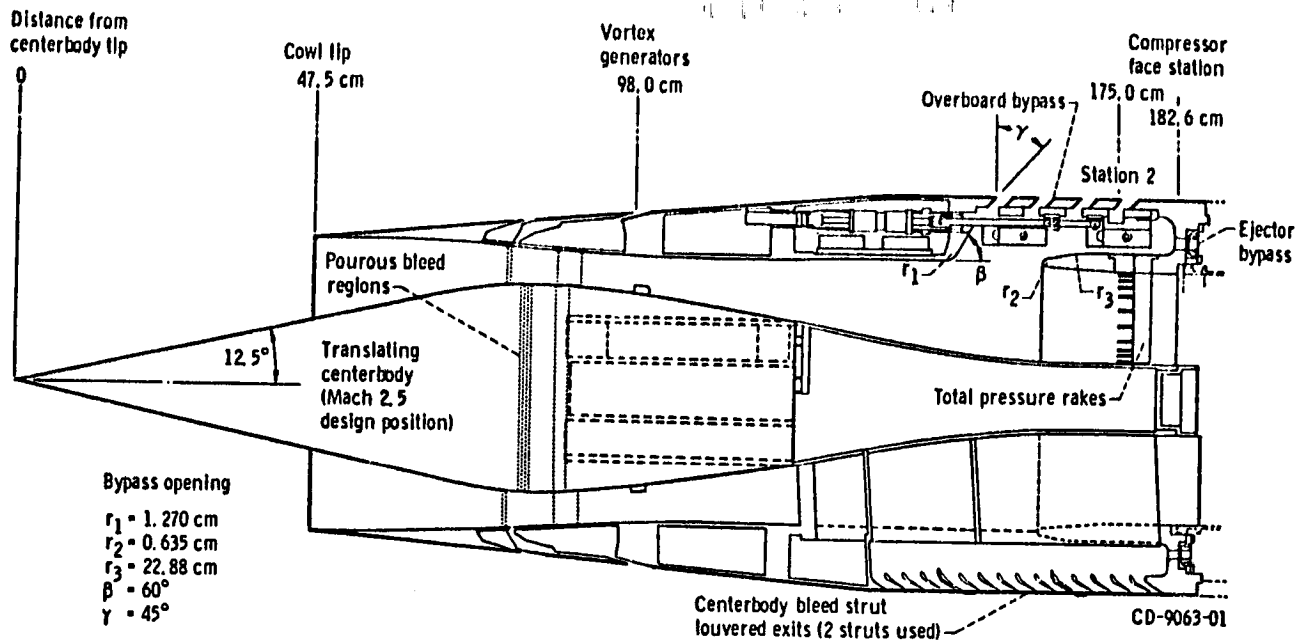
### 5.1 40-60 INLET

The NASA LeRC 40-60 inlet is an axisymmetric mixed-compression inlet with 40 percent of the effective supersonic area contraction occurring externally and 60 percent supersonic area contraction occurring internally at the design free-stream Mach number of 2.50. Details of the 40-60 inlet configuration and dynamic pressure transducer locations are given in Fig. 22. The inlet was equipped with a translating centerbody, high-response sliding plate overboard bypass doors, and an ejector bypass used for engine cooling. Pertinent details concerning experimental investigations of this inlet conducted in the NASA LeRC 10- by 10-foot supersonic wind tunnel are contained in Refs. 29 through 34.

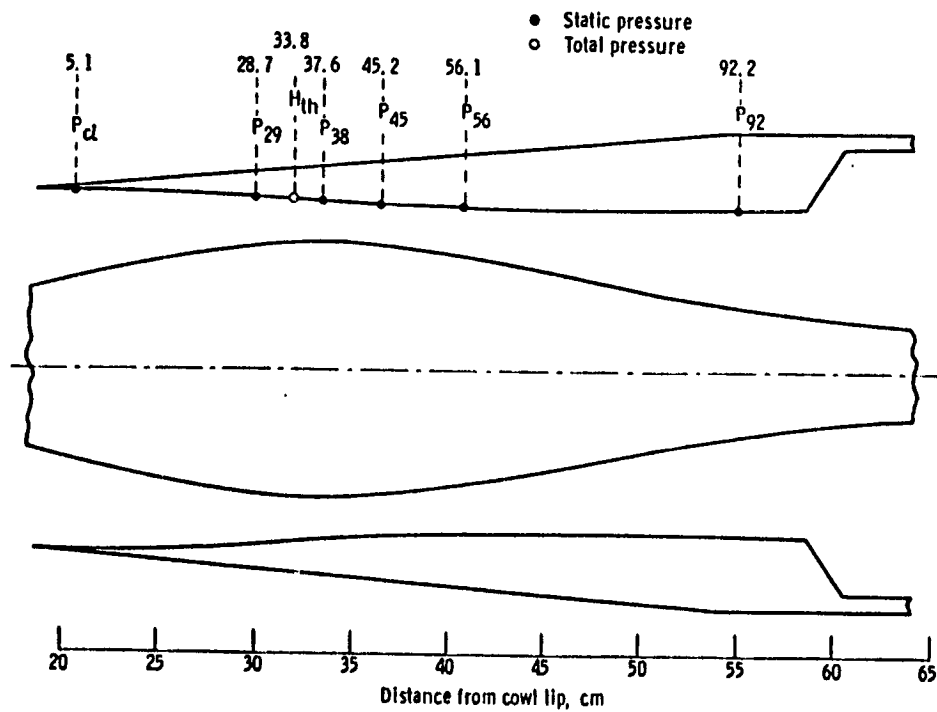
### 5.2 40-60 INLET STEADY-STATE PERFORMANCE

The present section will computationally examine the steady-state operation of the 40-60 axisymmetric mixed-compression inlet at a free-stream Mach number of 2.50. Experimental data reported in Ref. 31 will be used for comparison with calculated results. Details of the 40-60 inlet configuration and dynamic pressure transducer locations have been previously given in Fig. 22.

Overall inlet performance in terms of total pressure recovery as a function of engine-corrected mass flow variation is shown in Fig. 23. The calculated total pressure recovery is in good agreement with the experimental data and even predicts a flow oscillation at low mass flow which was experimentally observed at approximately the same value of mass flow. It is to be noted that the Program LAPIN momentum source term is based upon bleed and bypass extraction of momentum as if the transfer were accomplished in the tangential direction, even though the momentum flux is, in reality, transferred out of the inlet flow in a normal direction (see the discussion of this point in Section 3.6). If the momentum source term is not treated in this manner, erroneously high-pressure recovery (in some cases larger than unity) is predicted by the present approach.



(A) CONFIGURATION



(B) DYNAMIC PRESSURE TRANSDUCER LOCATIONS

FIGURE 22. 40-60 INLET DETAILS

ORIGINAL PAGE IS  
OF POOR QUALITY

MACH NO. 2.5  
COWL-LIP-POSITION 26.6°

- DATA - ENGINE CORRECTED MASS FLOW VARIATION (Ref. 31)
- + PROGRAM LAPIN - ENGINE CORRECTED MASS FLOW VARIATION
- DATA - VARYING BYPASS AT ENGINE CORRECTED MASS FLOW = 15.8 Kg/SEC (Ref. 31)
- X PROGRAM LAPIN - VARYING BYPASS AT ENGINE CORRECTED MASS FLOW = 15.8 Kg/SEC

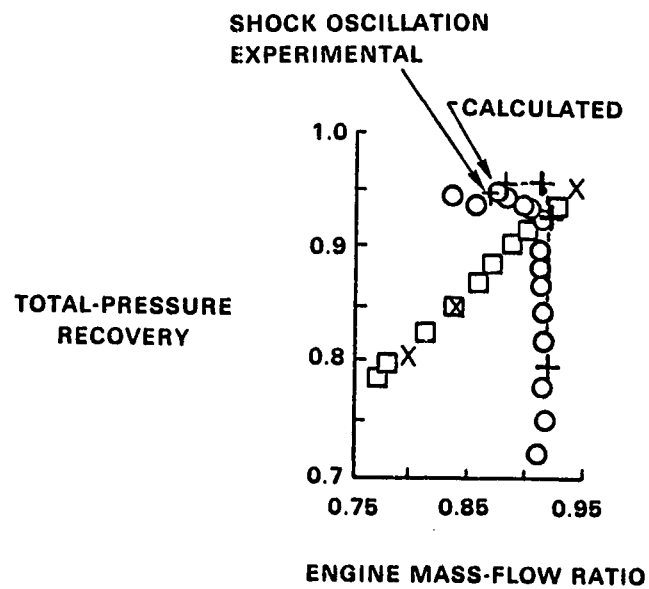


FIGURE 23. OVERALL PERFORMANCE OF THE 40-60 INLET WITH "DOWNSTREAM"  
BLEED AND BYPASS FLOW

Inlet static pressure distributions shown in Fig. 24 for the cowl surface and centerbody show that the calculated terminal normal shock location is significantly downstream of the experimentally indicated location. This discrepancy can be traced to the inviscid treatment of mass bleed effects without any allowance for viscous (boundary layer) interaction. Downstream of the throat region, the terminal normal shock and the boundary layer interact with possible flow separation and reattachment. Viscous-inviscid interaction is obviously dominant in establishing the resulting location of the terminal shock. Irrespective of this, the calculated static pressure distribution is in excellent agreement with experiment in regions upstream of the bleed locations and downstream of the calculated terminal shock.

### 5.3 40-60 INLET HAMMERSHOCK TRANSIENT

Hammershock transients are one of the most potentially dangerous situations which can occur in a supersonic inlet due to the large overpressure levels involved. The present section will computationally examine a hammershock transient in the 40-60 axisymmetric mixed-compression inlet at a free-stream Mach number of 2.50. Experimental data reported in Ref. 33 will be used for comparison with calculated results. Details of the 40-60 inlet configuration have been previously given in Fig. 22.

The experimental investigation of Ref. 33 generated a hammershock transient via engine compressor stall which resulted in a strong pressure disturbance, propagated upstream through the inlet. For purposes of performing the Program LAPIN calculation, the experimentally determined exit plane static pressure distribution was input as a prescribed downstream boundary condition. The results of this calculation are shown in Fig. 25, where station "2" represents the exit plane location. Inlet bypass setting was determined in order to match the experimentally determined total pressure recovery. The calculated upstream results are in reasonable agreement with the experimental data considering the fact that the present inviscid model positioned the steady-state terminal normal shock too far downstream due to neglect of viscous effects as noted earlier.



NASA LeRC 40 - 60 INLET

ORIGINAL COPY  
OF POOR QUALITY

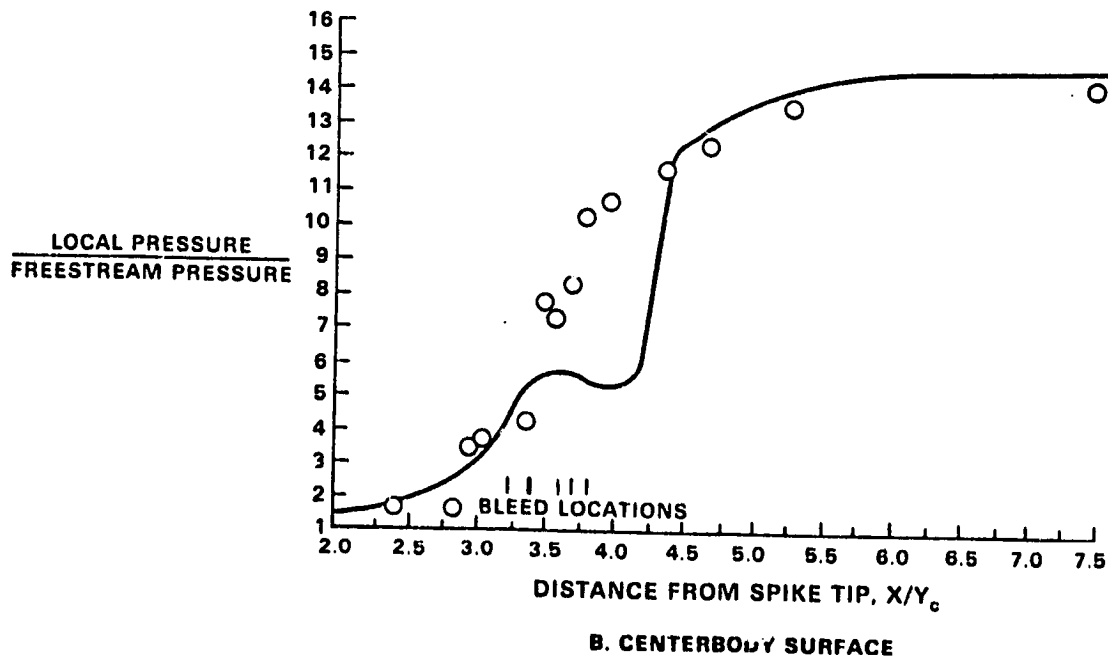
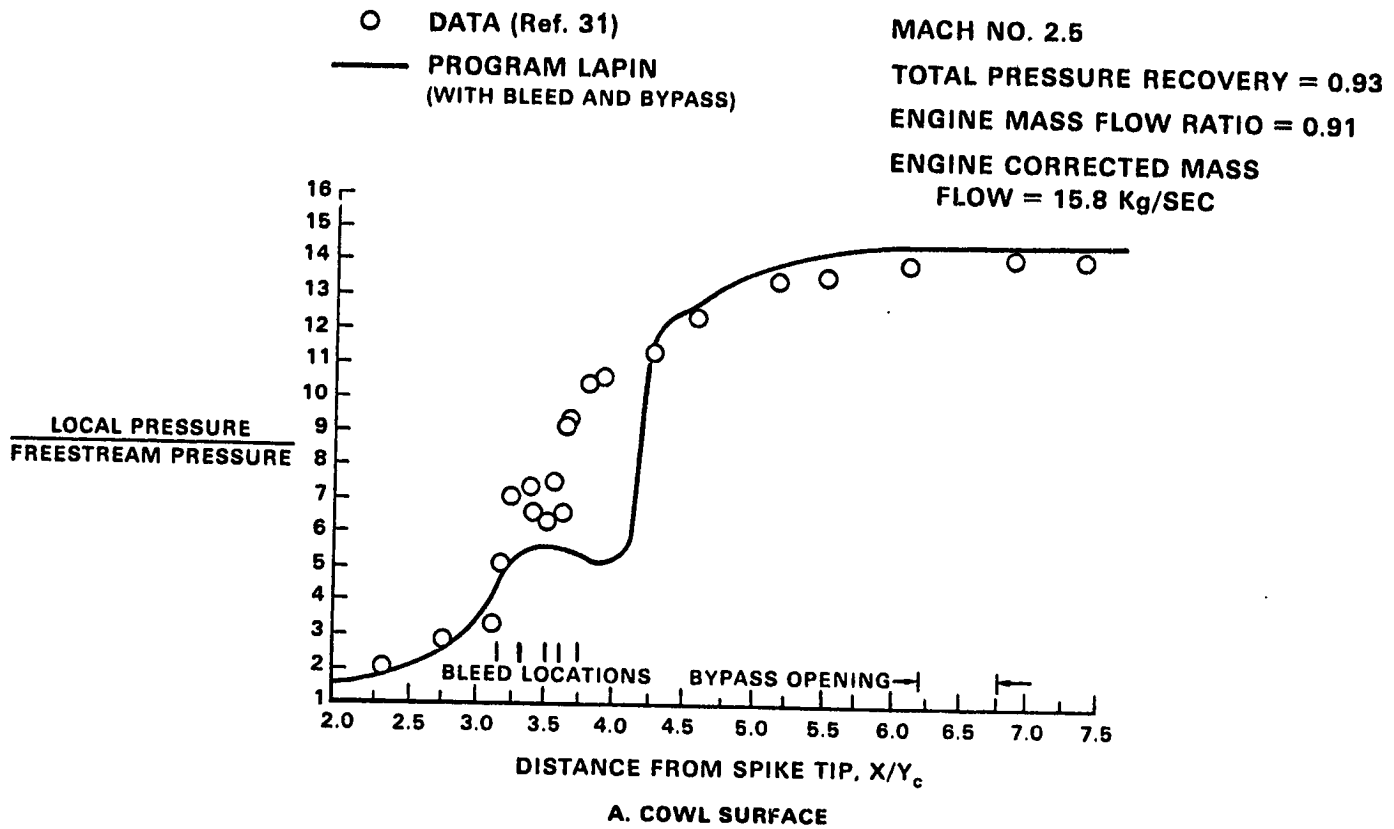


FIGURE 24. STATIC PRESSURE DISTRIBUTIONS

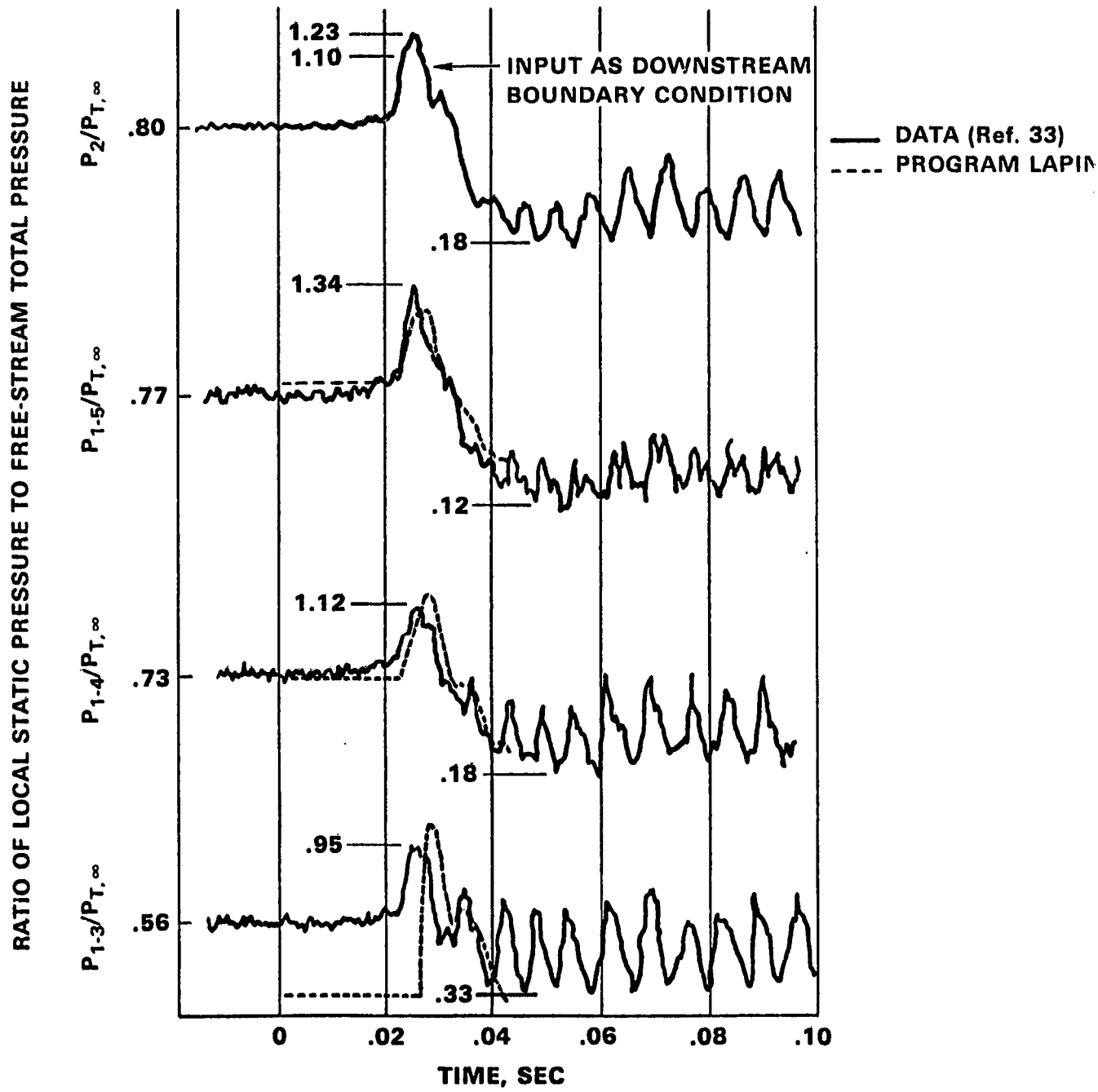
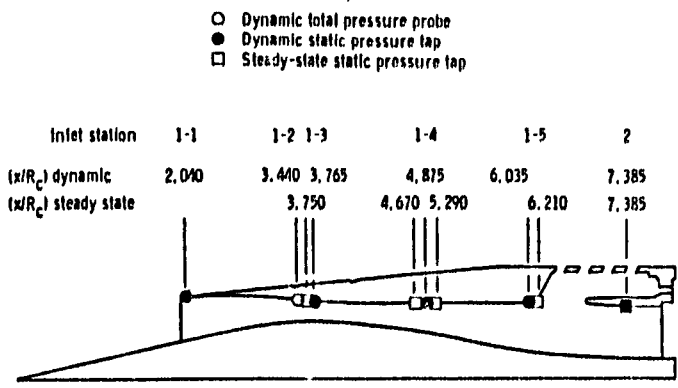


FIGURE 25. TIME HISTORY OF INLET PRESSURES AFTER COMPRESSOR STALL

It is of interest to computationally follow the development and movement of the above discussed hammershock transient through the inlet. Figure 26 gives the cross-sectional area distribution of the 40-60 inlet where it should be noted that the throat is located at a  $x$ -value of approximately 3.5. Figure 27 shows the corrected mass flow distribution and corresponding mass flow distribution; associated flow-field distributions of pressure, density, velocity, total internal energy, Mach number, total pressure, and total temperature are presented in Figs. 28 and 29. The key point to observe is the manner in which the terminal normal shock moves forward and amplifies in strength due to its movement. This is especially dramatic in the total pressure results of Fig. 29, where the total pressure behind the moving normal shock reaches a level of 1.2 times the free-stream total pressure; in a similar manner the total temperature of Fig. 29 reaches a value of 1.2 times the free-stream total temperature.

Another characteristic of inlet hammershock flow fields is the low subsonic Mach number (on the order of 0.2) behind the moving shock, as can be seen from Fig. 29; for comparison, the aftershock Mach number for a stationary normal shock at a Mach number of 2.50 is 0.5130 and at an infinite Mach number is the limiting value 0.378.

The hammershock calculation was performed using the implicit split characteristics solution algorithm with 41 grid points. Fig. 30 shows the Courant number distribution as a function of time. The inlet plane Courant number was reduced from a value slightly over 5 to 0.9 when the moving shock reached a  $x$ -location of approximately 3 in order to accurately track the moving shock upstream of the throat.

#### 5.4 40-60 INLET UNSTART/RESTART TRANSIENT

During normal, started operation of mixed-compression inlets, variations in engine airflow are generally compensated for by the overboard bypass system. In this manner, the terminal shock can be positioned such that optimum inlet performance is maintained. If the bypass doors are scheduled to open upon unstart, the scheduled area must be large enough to compensate for the maximum reduction in engine airflow that could occur as a result of the unstart. However,

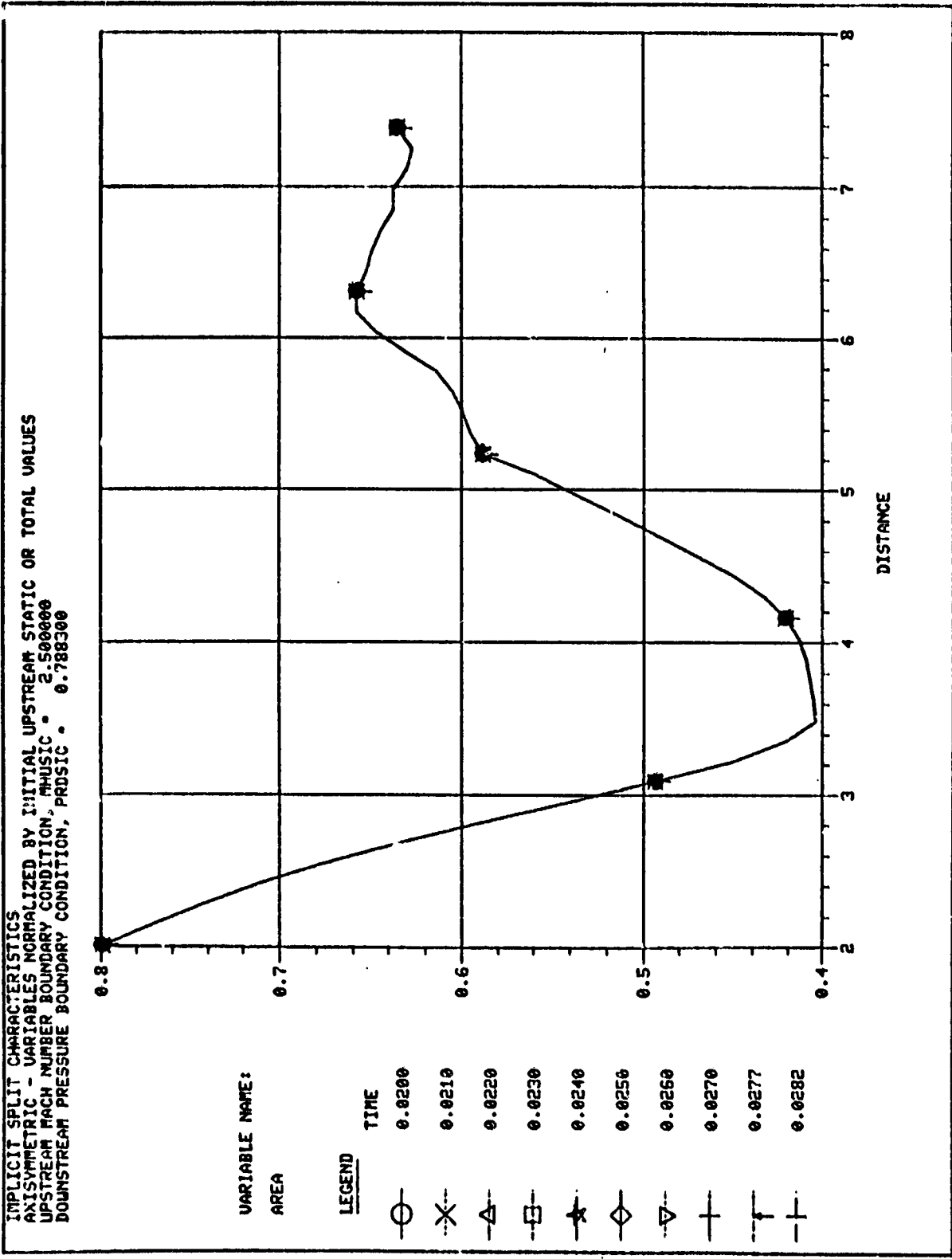
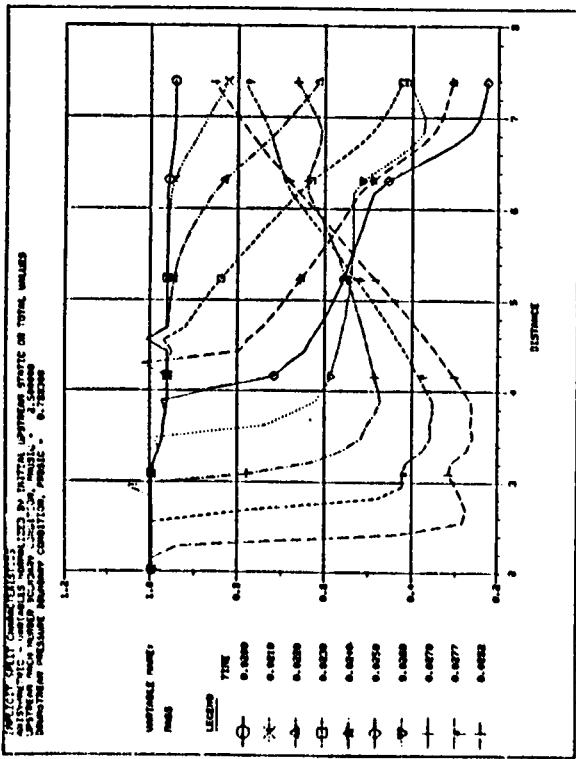
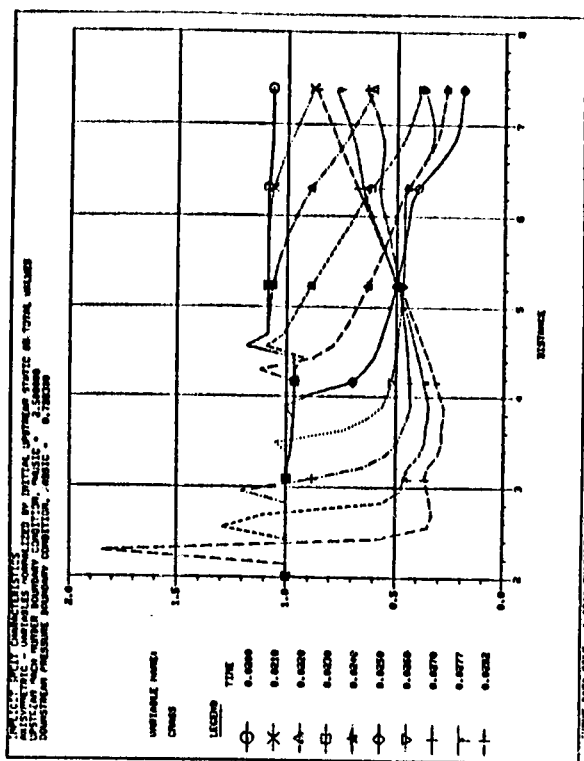


FIGURE 26. INLET AREA DISTRIBUTION

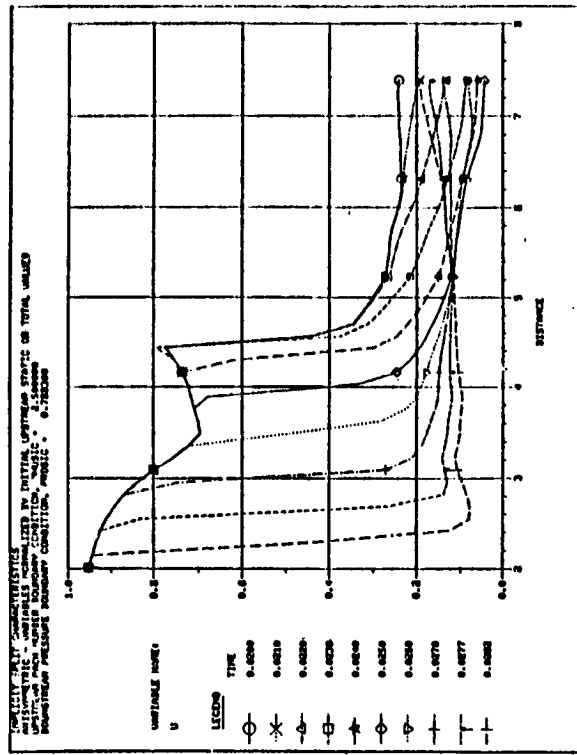


A. MASS FLOW RATIO,  $\dot{m}/\dot{m}_{CAPTURE}$

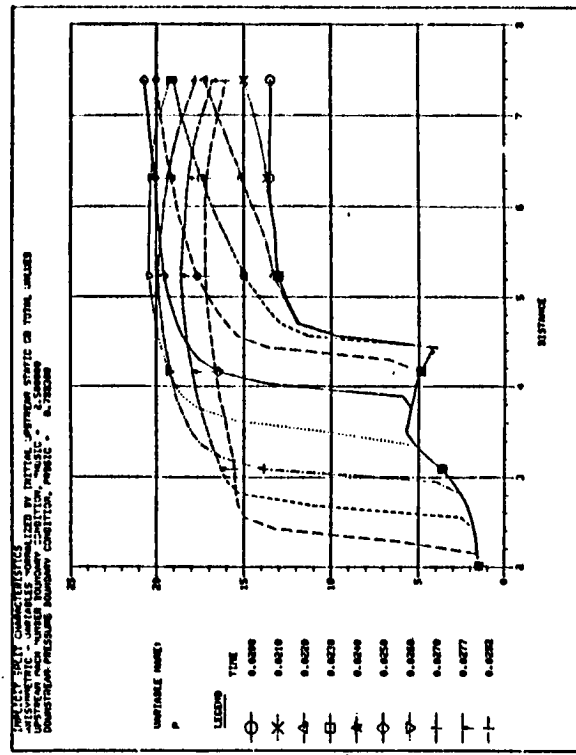


B. CORRECTED MASS FLOW RATIO

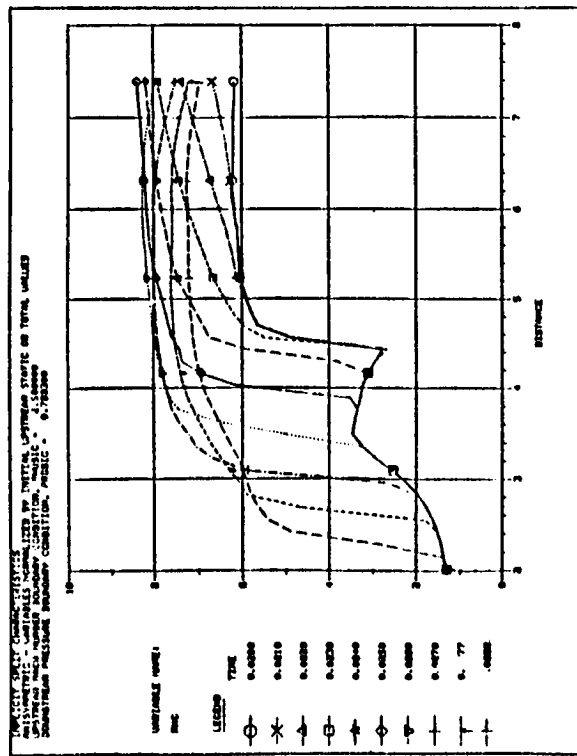
FIGURE 27. MASS FLOW DISTRIBUTION DURING HAMMERSHOCK TRANSIENT



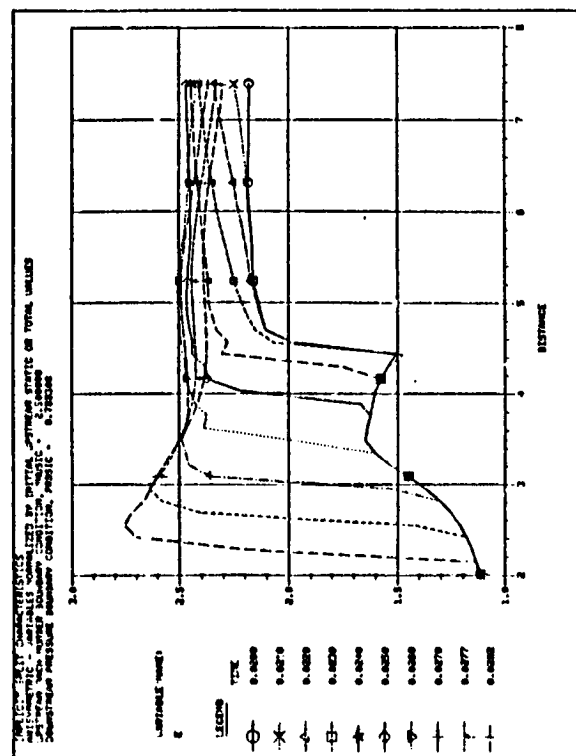
B. VELOCITY RATIO,  $u/V_{\infty}$



D. PRESSURE RATIO,  $p/p_{\infty}$

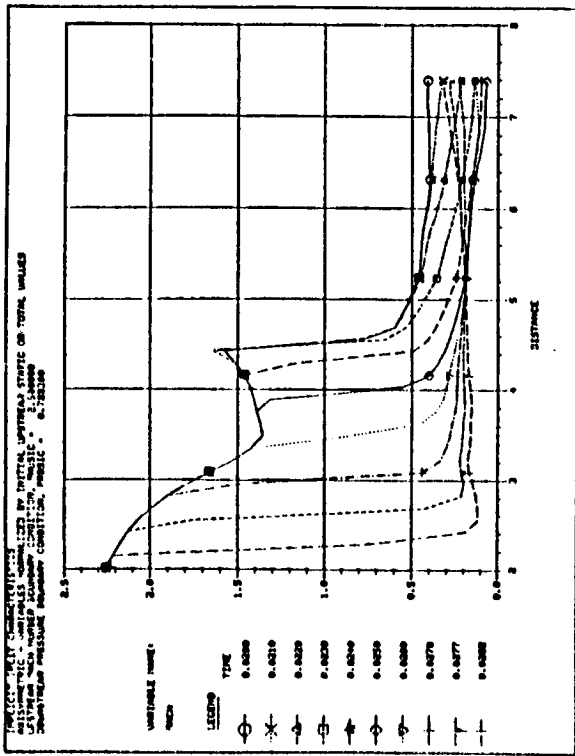


A. DENSITY RATIO,  $\rho/\rho_{\infty}$

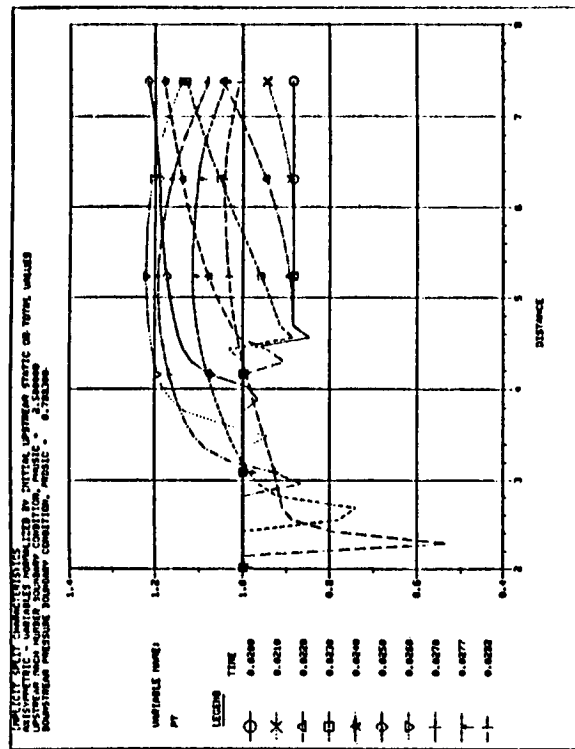


C. ENERGY RATIO,  $E/E_{\infty}$

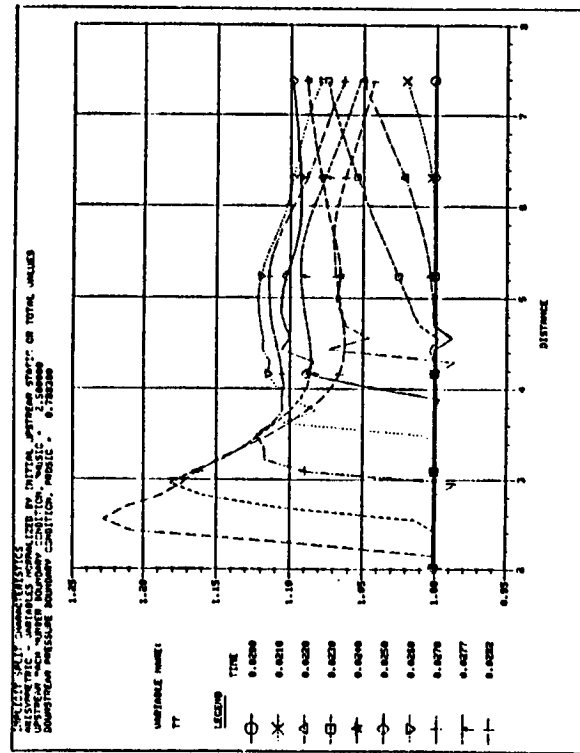
FIGURE 28. FLOW VARIABLES DURING HAMMERSHOCK TRANSIENT



A. MACH NUMBER



B. TOTAL PRESSURE RATIO,  $P_T/P_{T_\infty}$



C. TOTAL TEMPERATURE RATIO,  $T_T/T_{T_\infty}$

UNCLASSIFIED CONFIDENTIALS  
 UNCLASSIFIED UNLESS INDICATED OTHERWISE BY INITIALS, POSTERIOR STATE, OR TOTAL VALUE  
 AUTHORITY: CONTROLLED BY INITIALS, POSTERIOR STATE, OR TOTAL VALUE  
 DISSEMINATION RESTRICTIONS: UNCLASSIFIED, PUBLIC \* 6-782338

FIGURE 29. FLOW QUANTITIES DURING HAMMERSHOCK TRANSIENT

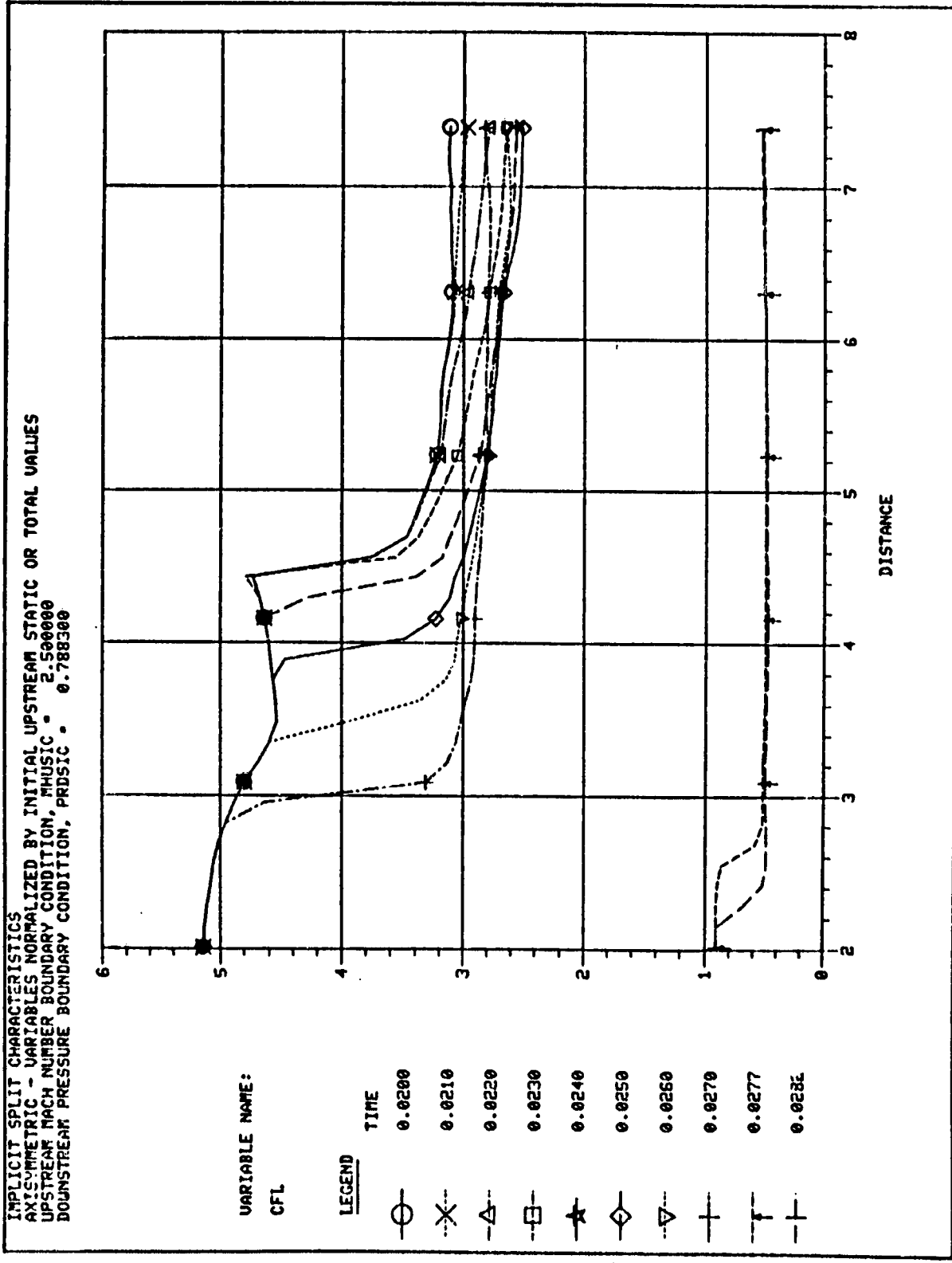


**FIGURE 30. COURANT NUMBER DISTRIBUTION DURING HAMMERSHOCK TRANSIENT**



scheduling bypass area for a bypass flow greater than that required would result in higher distortion and lower pressure recovery. If the engine continues to operate normally after the unstart transient, the increase in distortion could initiate a compressor stall.

The present section will computationally examine the unstart/restart transient operating characteristics of the 40-60 axisymmetric mixed-compression inlet with a cold pipe extension at a free-stream Mach number of 2.50. Experimental data reported in Ref. 29 will be used for comparison with calculated results. Details of the 40-60 inlet configuration and dynamic pressure transducer locations have been previously given in Fig. 22.

Inlet unstart followed by controlled restart is shown in Fig. 31 where the top two curves (disturbance door area and control door area) give the bypass door schedule in time, and the third curve from the top (centerbody position) represents centerbody translation in time from the fully retracted position. For purposes of the present one-dimensional computation, the disturbance door and control door area schedules were lumped together to provide a composite bypass door area schedule. The following is a description of the major events that occurred during the unstart/restart transient shown in Fig. 31:

1. The terminal normal shock was initially placed on the verge of unstart, i.e., located immediately downstream of the inlet throat.
2. A pulse decrease in disturbance door area caused the terminal normal shock to move upstream.
3. The control doors are opened (increased area) to restore shock position in order to prevent inlet unstart.
4. Despite the terminal shock control action, a net decrease in bypass mass flow was created and the inlet unstated.
5. The bypass doors were fully opened and the centerbody was translated forward to restart the inlet.
6. Upon inlet restart, the centerbody was retracted to its original position, and the control door area was decreased to move the terminal normal shock to a stable location downstream of the inlet throat.

ORIGINAL FACSIMILE  
OF POOR QUALITY

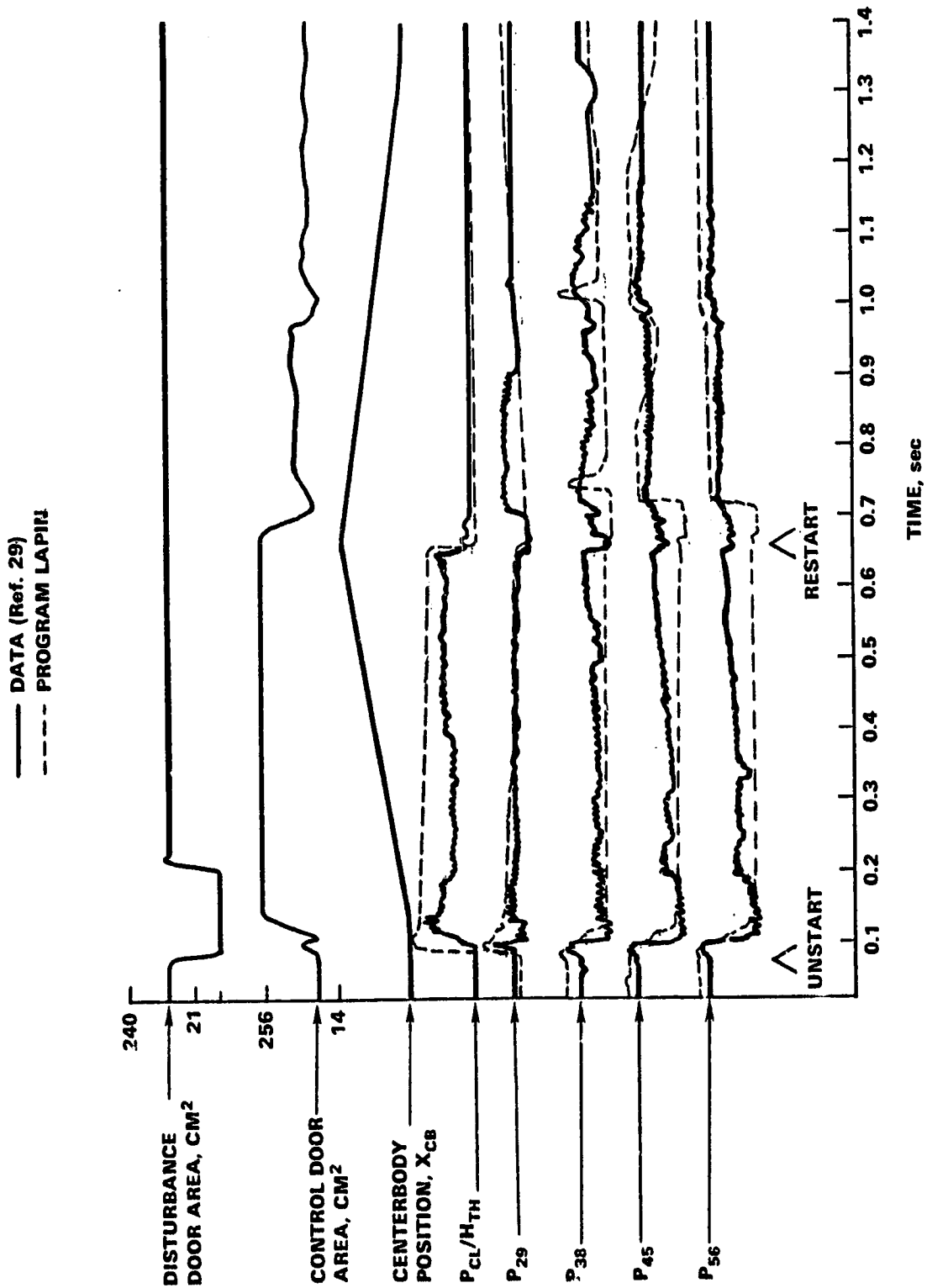


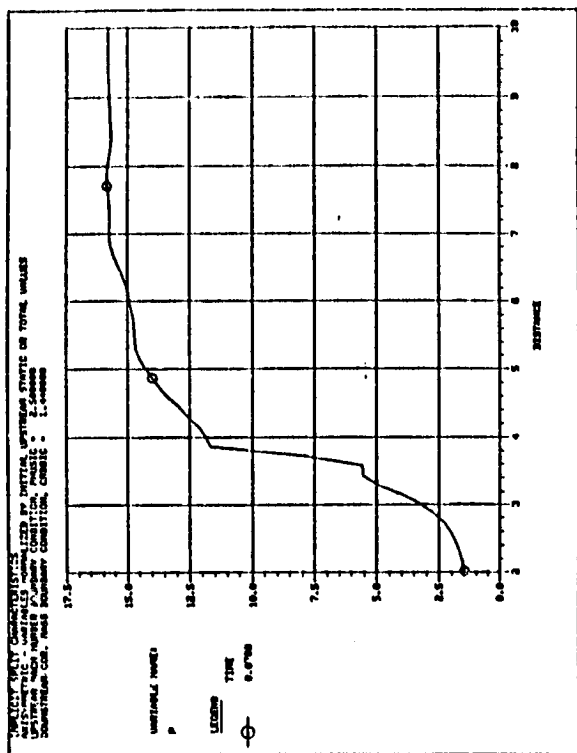
FIGURE 31. INLET UNSTART/RESTART HISTORY

In general, the present one-dimensional unsteady inviscid simulation agrees reasonably well with experiment. The disagreement shown in cowl lip pressure  $p_{CL}$  during unstart is due to viscous effects (flow separation caused by interaction of the unstarted normal shock with the centerbody boundary layer) influencing the "effective" area distribution of the inlet flow field upstream of the throat. The physical time for occurrence of both unstart and restart is accurately modeled by the simulation. After restart the inviscid simulation indicates some normal shock movement which is not supported by the experimental data. This movement is probably the result of viscous effects influencing shock location in the inlet diffuser through boundary-layer/shock interaction.

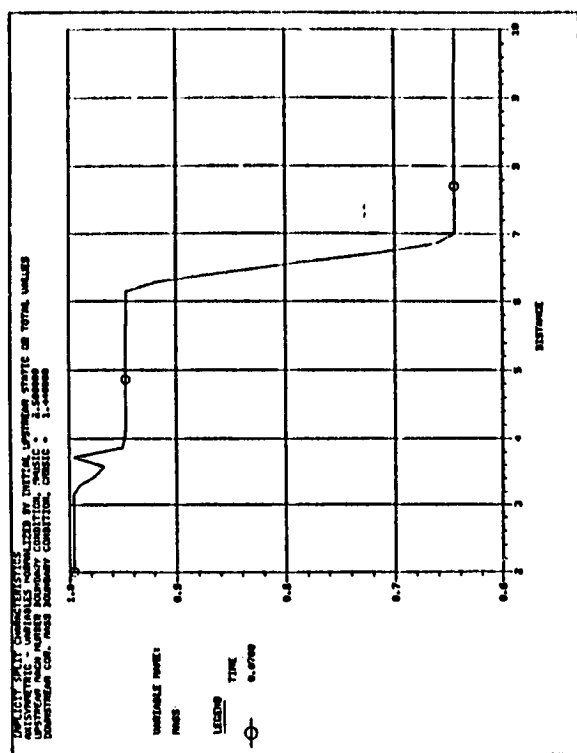
Given that the present one-dimensional unsteady inviscid model is a reasonably accurate simulation of supersonic inlet unstart/restart phenomena as shown above, it is now in order to examine the computational details of the inlet flow field. Presented in Fig. 32 are the inlet area, static pressure, Mach number, and mass flow distributions at a time of 0.07 seconds which is just prior to initiation of bypass door closure. It should be noted that the downstream area distribution reflects struct blockage effects; however, bypass plenum effects are not included in the area distribution as all bypass flow phenomena are modeled as discussed earlier. Further note that the normal shock is positioned in the throat region and maintained there by throat bleed. The large effect of bypass mass removal on downstream mass flow is strikingly apparent in Fig. 32.

Figure 33 shows the calculated details of the inlet unstart transient, which is extremely rapid (on the order of 0.01 to 0.02 seconds). Note the decrease in inlet diffuser static pressure following unstart; this decrease in pressure is the direct result of the sizable decrease (50 to 70 percent) in inlet mass flow due to unstart mass spillage over the cowl. Further note the negative Mach number and mass flow within the inlet at a time of 0.0997 seconds. This is a direct result of the strong unstart transient creating a hammershock-like flow which has sufficient shock speed "drag" to reverse the local flow behind the moving shock.

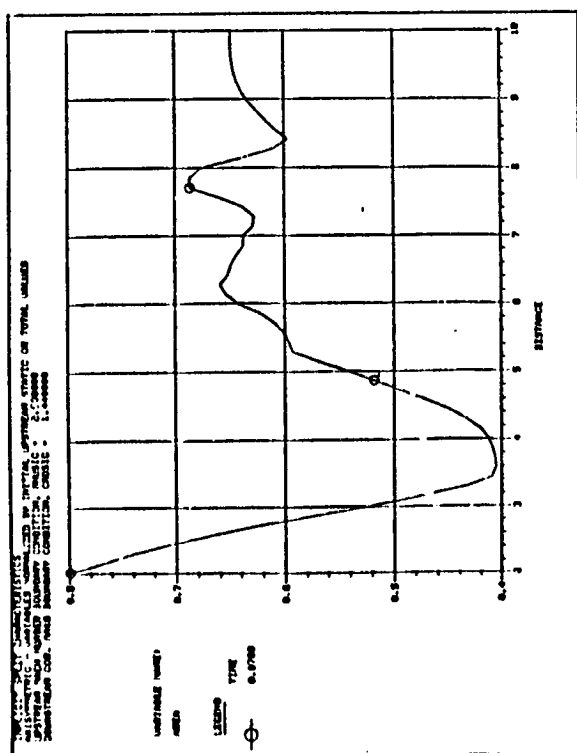
ONWARD FLOW OF FOUR QUALITY



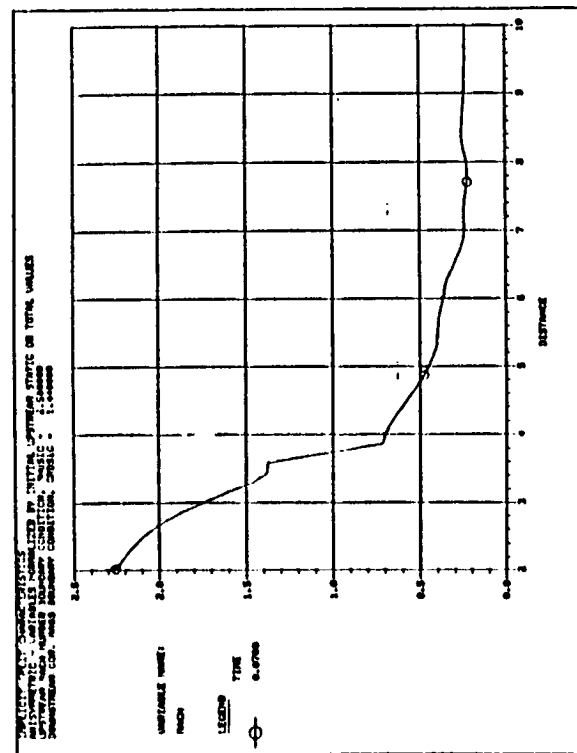
B. Pressure ratio,  $p/p_{\infty}$



D. MASS FLOW RATIO,  $\dot{m}/\dot{m}_{CAPTURE}$

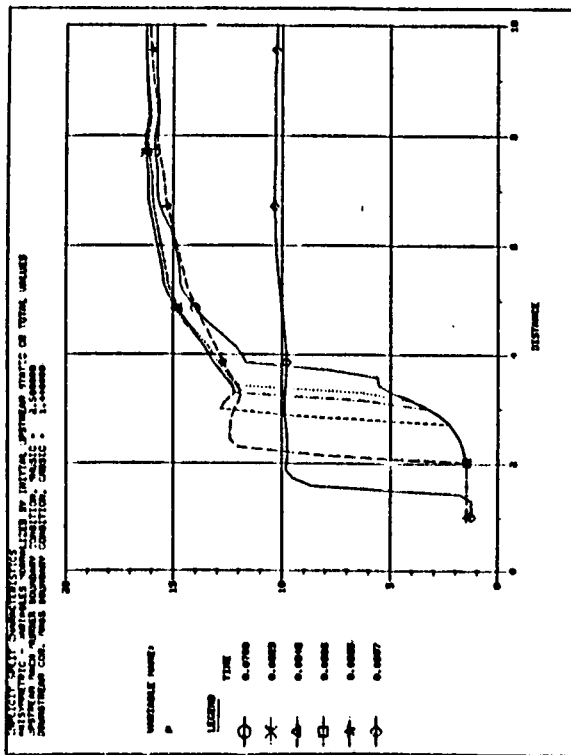


A. AREA RATIO,  $A/A_{CAPTURE}$

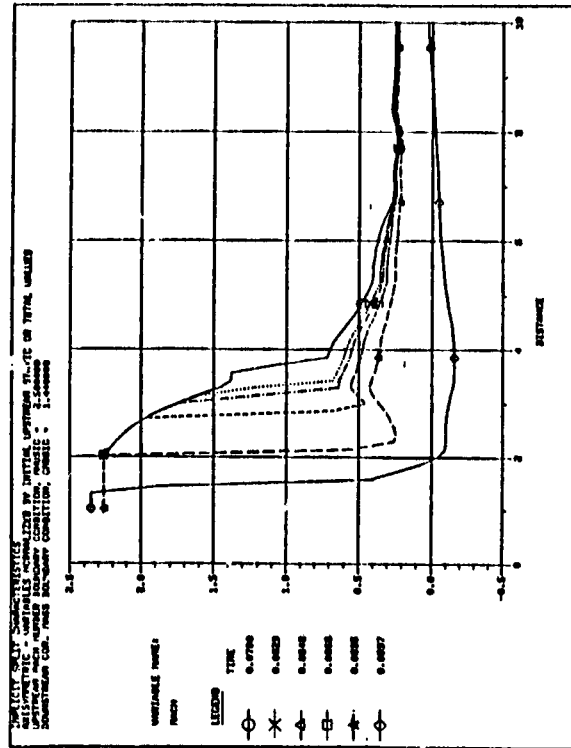


C. MACH NUMBER

FIGURE 23 INITIAL CONDITIONS AT TIME = 0.07 SECONDS

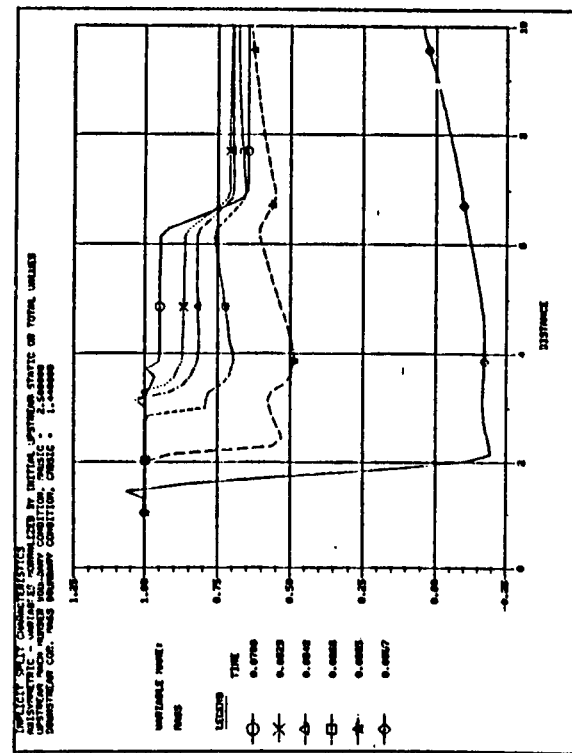


A. PRESSURE RATIO,  $p/p_{\infty}$



B. MACH NUMBER

ORIGINAL QUALITY  
 OF POOR QUALITY



C. MASS FLOW RATIO,  $\dot{m}/\dot{m}_{\text{CAPTURE}}$

FIGURE 33. UNSTART TRANSIENT BETWEEN TIME = 0.07 SECONDS  
 AND TIME = 0.0997 SECONDS

Centerbody translation effects are shown in Fig. 34 where the forward movement serves to increase the throat area and decrease the cowl capture area. This physical geometry change results in the flow choking at the throat with supersonic diffuser flow terminating through a normal shock; note the rearward and then forward movement of this shock reflecting the changing area distribution due to centerbody translation. The mass flow essentially stabilizes throughout the inlet, although the mass flow entering the inlet decreases.

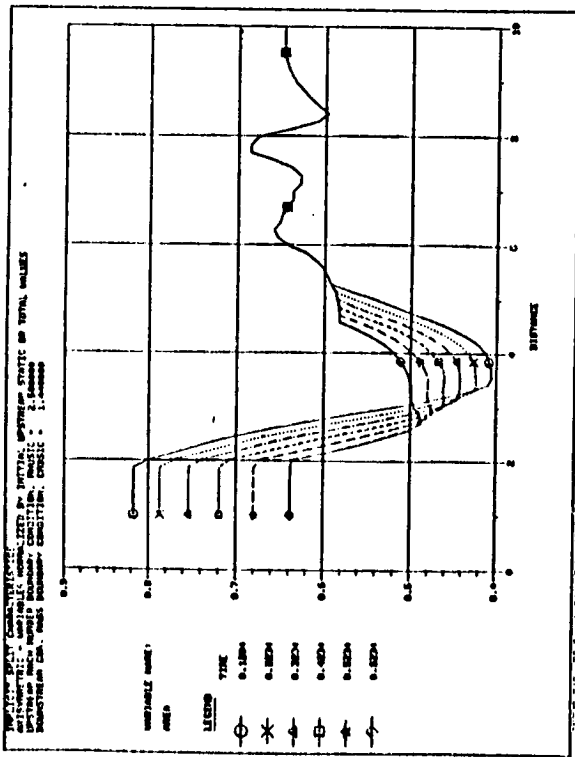
Details of inlet restart are given Fig. 35. The actual restart is the result of decreasing the mass flow entering the inlet until such a value is reached that can be passed through the (choked) throat area. When this occurs the unstart normal shock moves rapidly into the inlet, passes through the throat, and creates a terminal normal shock in the inlet diffuser.

With the inlet restarted, the centerbody is retracted as shown in Fig. 36 resulting in a decrease in throat area and an increase in capture area. This movement results in some fore and aft oscillations of the terminal normal shock as the mass flow through the inlet increases. At the last time shown (1.3951 seconds), the inlet is approaching a steady-state operating condition.

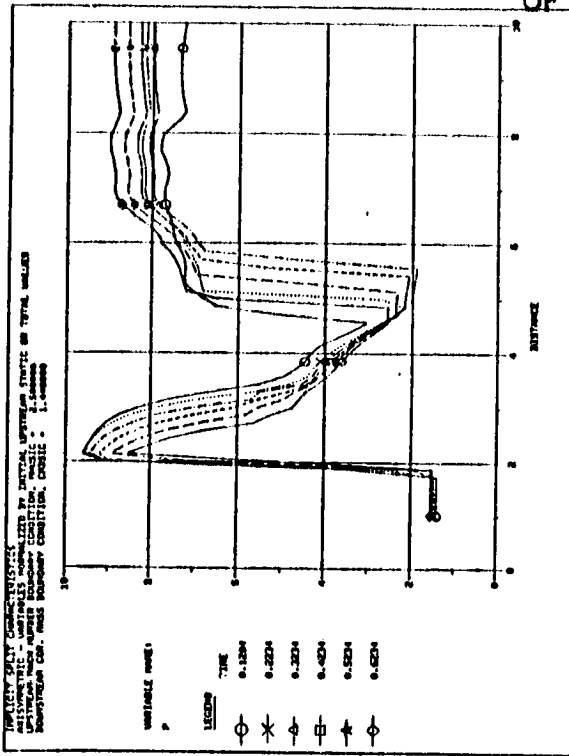
Temporal details of the present unstart/restart calculation are shown in Figures 37 through 39 for four axial locations (3.22, 3.60, 3.92, and 4.38) corresponding to locations where experimental pressure measurements were reported in Fig. 31. Note that these locations are in the throat region of the inlet under design conditions, i.e., no centerbody translation, as can be seen from reference to Fig. 32. With respect to the unstart/restart transient, it is to be remembered from the previously discussed results that inlet unstart occurred at a time of approximately 0.09 seconds with inlet restart at a time of approximately 0.65 seconds.

Details of the inlet area variation with time are shown in Fig. 37. Forward/rearward translation of the centerbody is apparent, with resulting increase/decrease of the throat area.

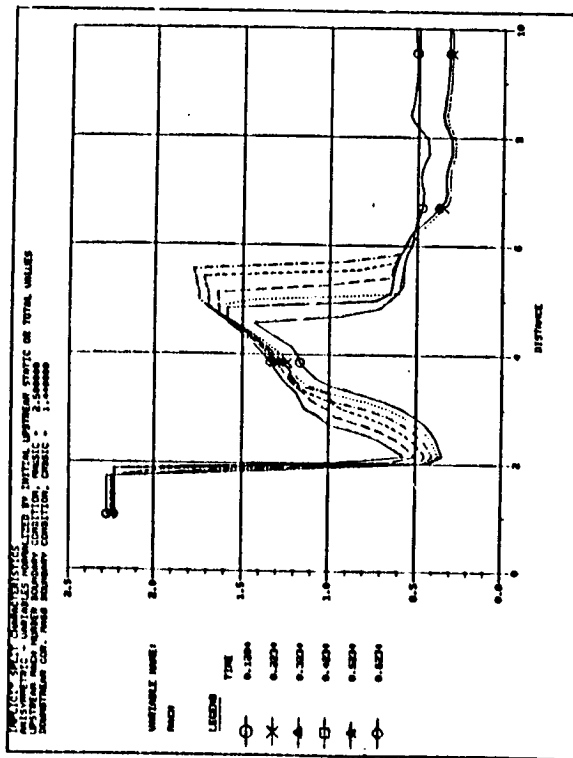
ORIGINAL DRAWING  
OF POOR QUALITY



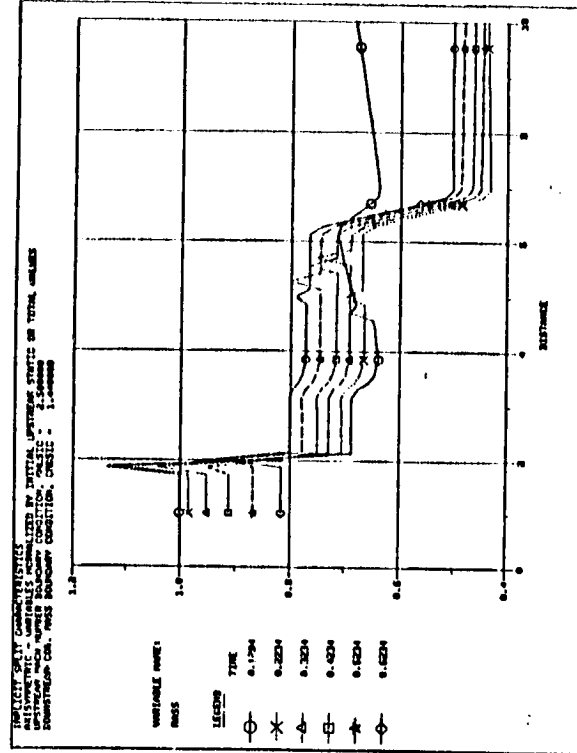
A. AREA RATIO,  $A/A_{CAPTURE}$



B. PRESSURE RATIO,  $p/p_{\infty}$

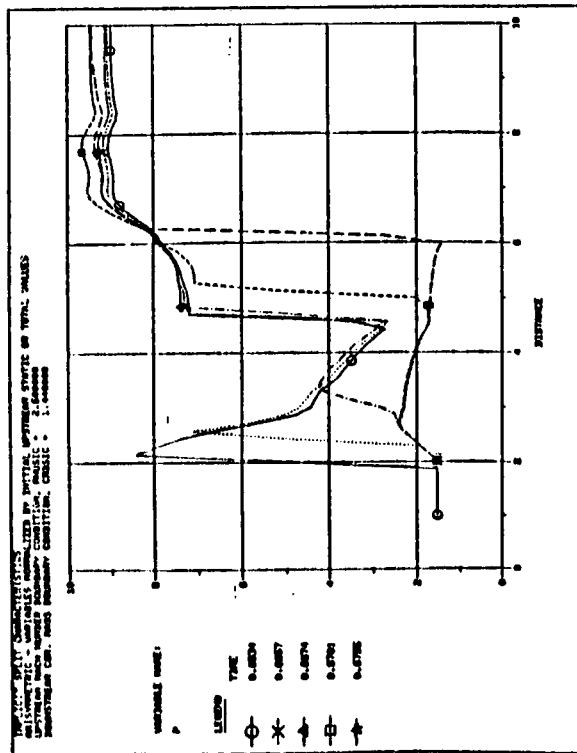


C. MACH NUMBER

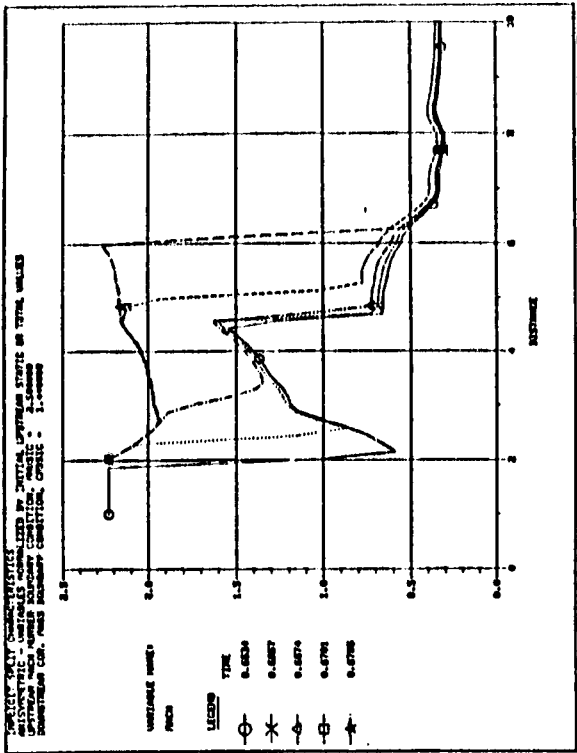


D. MASS FLOW RATIO,  $\dot{m}/\dot{m}_{CAPTURE}$

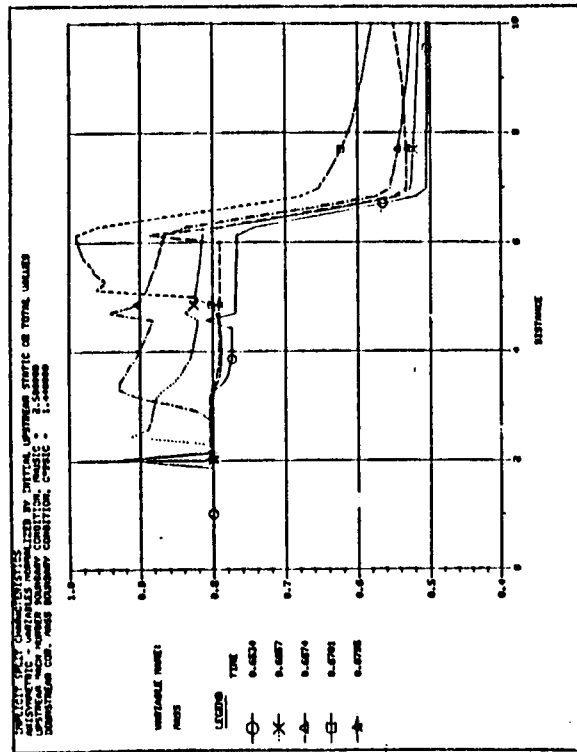
FIGURE 34. CENTERBODY FORWARD TRANSLATION BETWEEN  
TIME = 0.1204 SECONDS AND TIME = 0.6234 SECONDS



A. PRESSURE RATIO,  $p/p_{\infty}$



B. MACH NUMBER

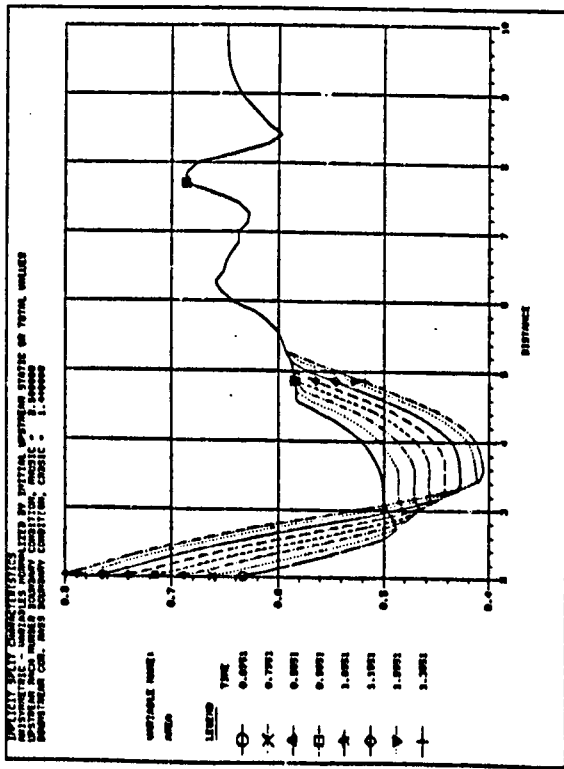


C. MASS FLOW RATIO,  $\dot{m}/\dot{m}_{\text{CAPTURE}}$

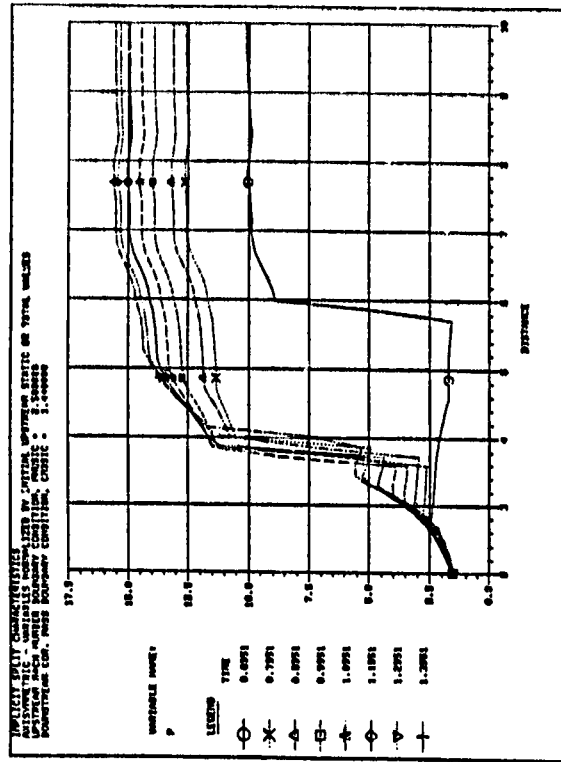
FIGURE 25 RESTART TRANSIENT BETWEEN TIME = 0.6534 SECONDS



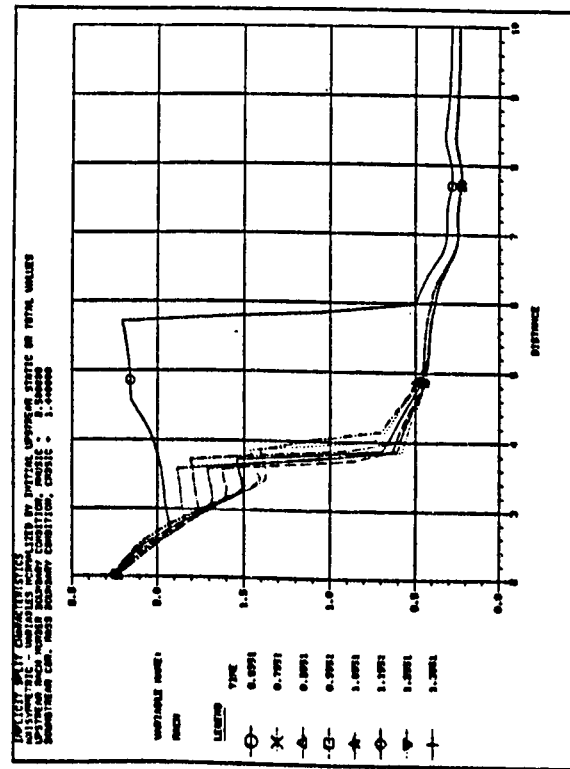
ORIGINAL DRAWING  
OF POOR QUALITY



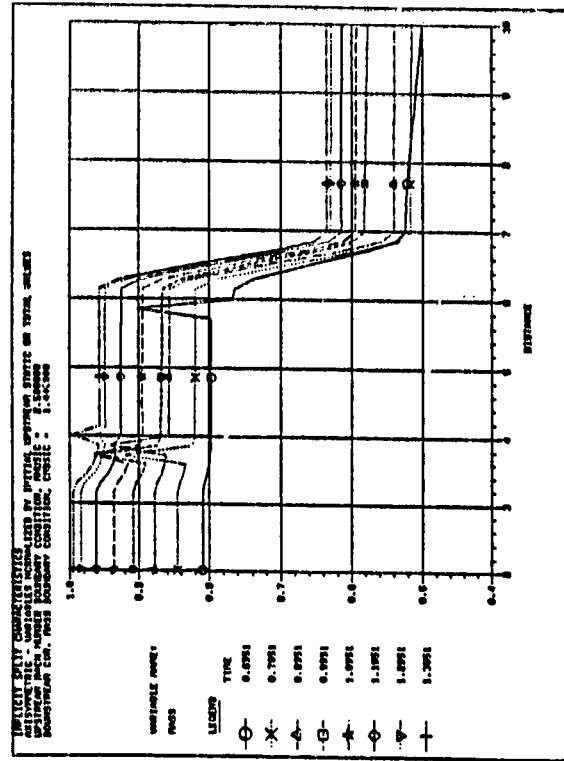
A. AREA RATIO, A/A<sub>CAPTURE</sub>



B. PRESSURE RATIO, p/p<sub>∞</sub>



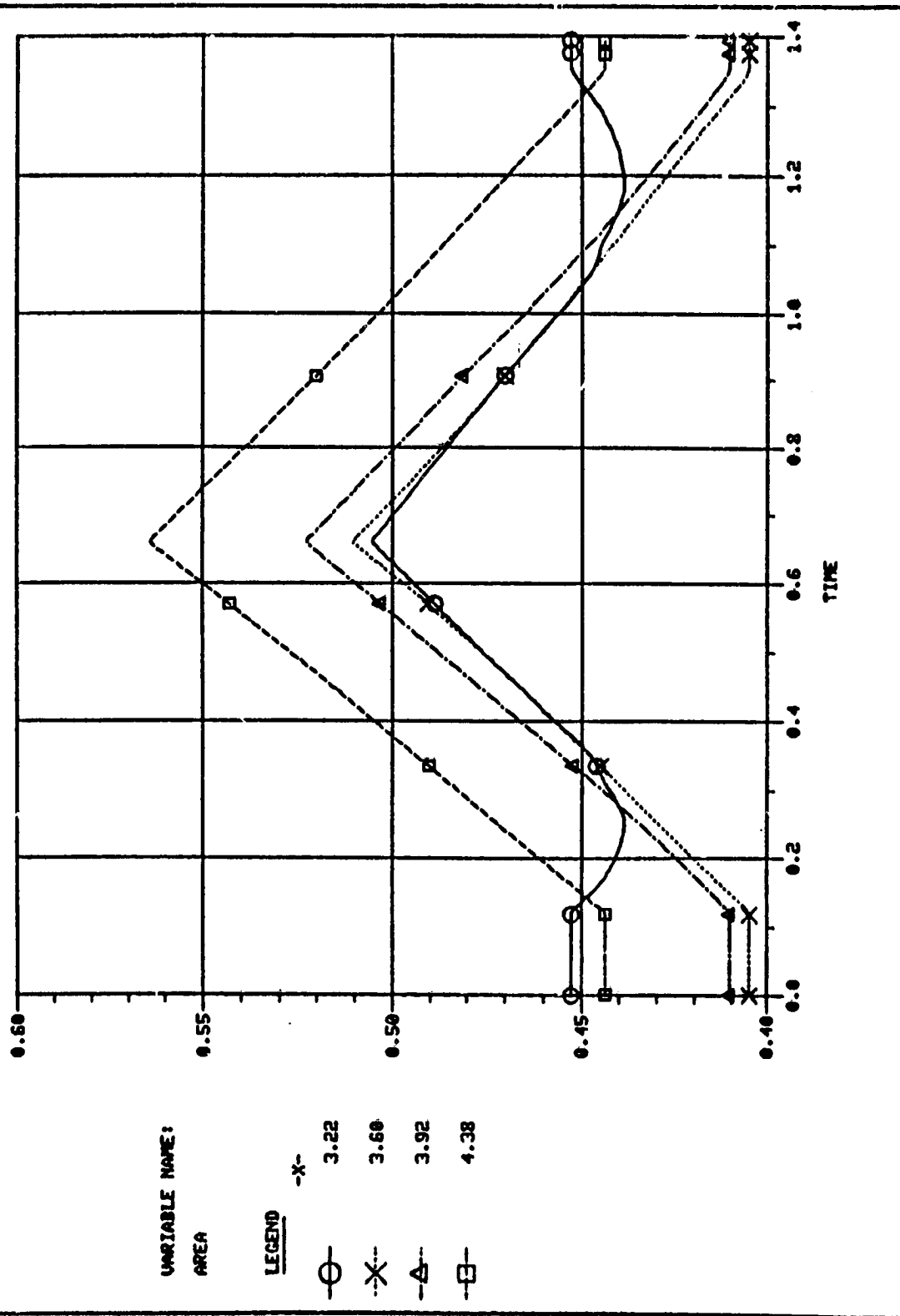
C. MACH NUMBER



D. MASS FLOW RATIO,  $\dot{m}/\dot{m}_{CAPTURE}$

FIGURE 36. CENTERBODY RETRACTION BETWEEN TIME = 0.6951 SECONDS  
AND TIME = 1.3951 SECONDS

IMPLICIT SPLIT CHARACTERISTICS  
 AXISYMMETRIC - VARIABLES NORMALIZED BY INITIAL UPSTREAM STATIC OR TOTAL VALUES  
 UPSTREAM MACH NUMBER BOUNDARY CONDITION, MACHIC = 2.500000  
 DOWNSTREAM COR. MASS BOUNDARY CONDITION, CMDSIC = 1.440000



VARIABLE NAME:

AREA

LEGEND

- 3.22
- × 3.60
- △ 3.92
- 4.38

FIGURE 37. TEMPORAL VARIATION OF AREA DISTRIBUTION  
 DURING UNSTART/RESTART

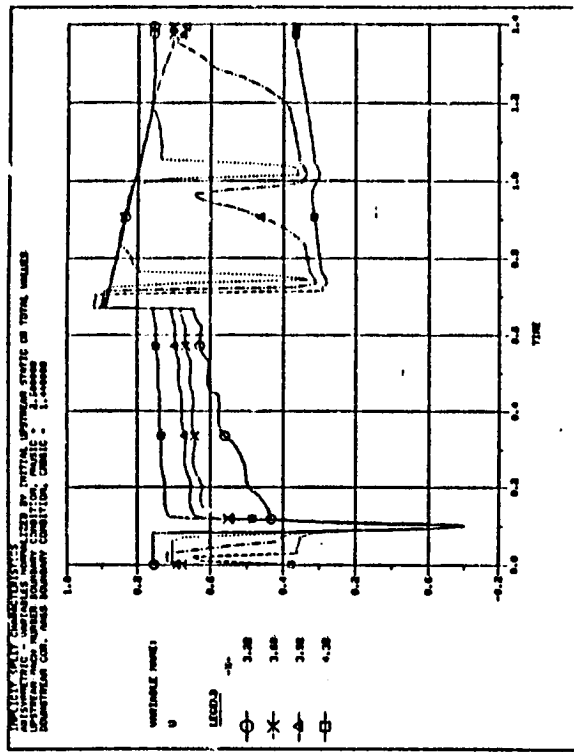
C2

Fluid dynamic details of the transient unstart/restart flow are given in Figs. 38 and 39. The transient variation in all the fluid dynamic variables during unstart (at a time of approximately 0.09 seconds) and during restart (at a time of approximately 0.65 seconds) are quite pronounced. In addition, the transient oscillation of the terminal normal shock near the throat region after restart (time greater than approximately 0.65 seconds) can be seen quite clearly in Fig. 39 for the Mach number.

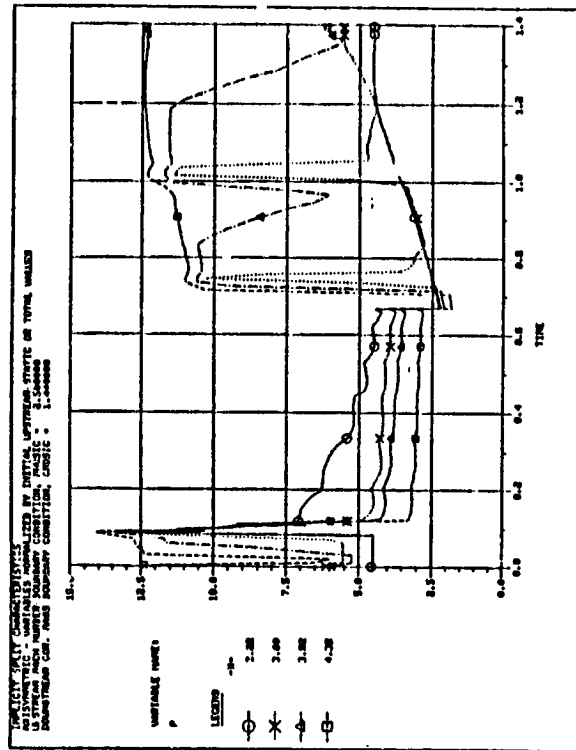
The above calculation was performed using a prescribed corrected mass flow exit plane boundary condition. A Courant number condition of approximately ten (10) was utilized for all started phases of the calculation with a Courant number of 0.90 utilized for all unstart and restart portions of the calculation where the normal shock moved rapidly. A total of 105 grid points was applied to discretize the flow field within the inlet itself; an additional seven (7) grid points were appended in front of the inlet for the unstart/restart phase. The "spike" which appears in the mass flow calculations presented earlier is due to the shock capturing nature of the numerical solution algorithm across strong normal shocks. A total of approximately 5,000 time steps was required to perform the complete transient calculation over a 1.40 second physical time interval with a corresponding computer CPU time requirement of approximately 50 minutes on a Digital Equipment Corporation VAX-11/780.

### 5.5 40-60 INLET DYNAMIC RESPONSE

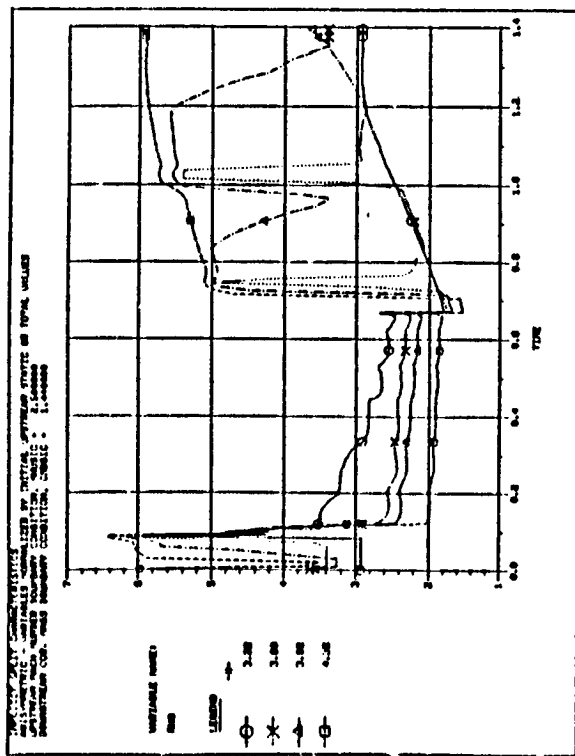
The experimental investigation of Ref. 32 was concerned with evaluation of the dynamic response characteristics of the 40-60 inlet configuration at a free-stream Mach number of 2.50. The inlet was coupled to a long cold pipe and subjected to sinusoidal bypass area disturbances as well as sinusoidal free-stream Mach number perturbations created via a gust plate. In the present section, frequency response parameters based upon Program LAPIN calculated results will be presented in comparison with the above discussed experimental results.



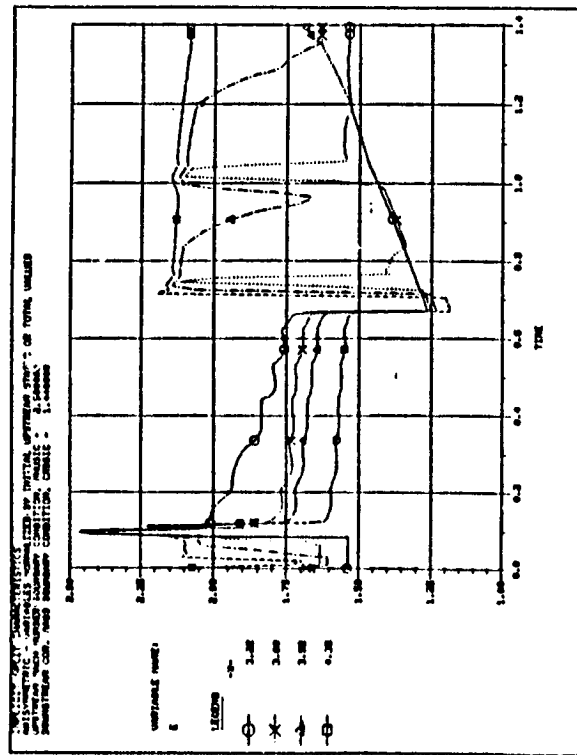
B. VELOCITY RATIO,  $u/V_\infty$



D. PRESSURE RATIO,  $p/p_\infty$



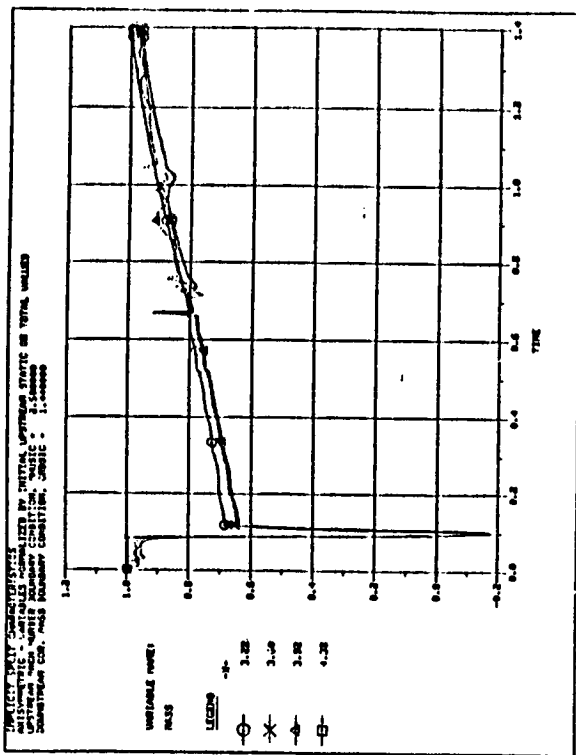
A. DENSITY RATIO,  $\rho/p_\infty$



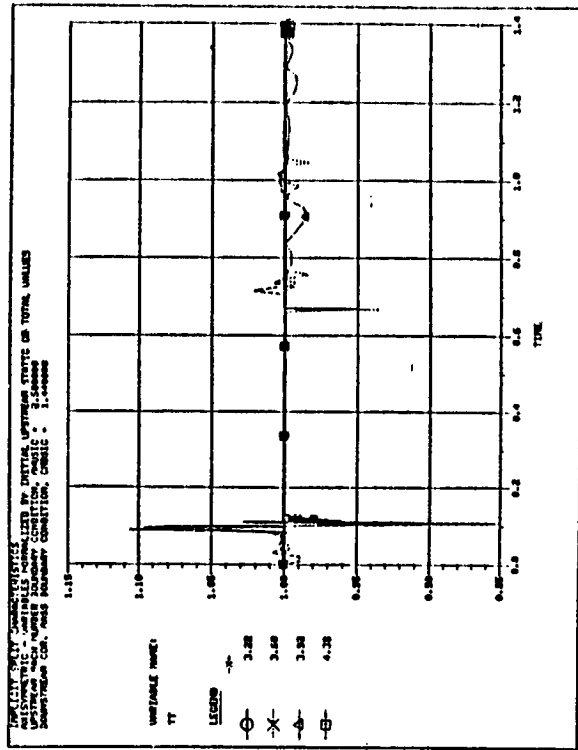
C. ENERGY RATIO,  $E/E_\infty$

FIGURE 38. TEMPORAL VARIATION OF FLOW VARIABLES

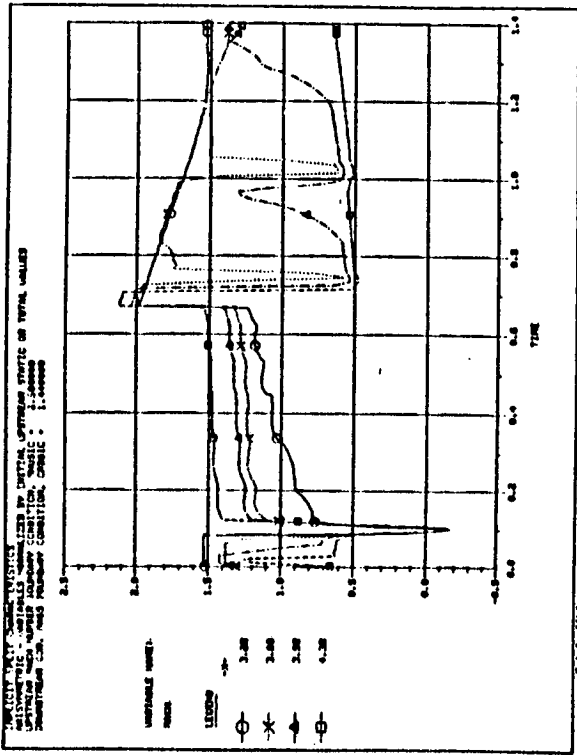
ORIGINAL  
OF POC...



A. MACH NUMBER



B. MASS FLOW RATIO,  $\dot{m}/\dot{m}_{CAPTURE}$



C. TOTAL PRESSURE RATIO,  $P_T/P_{T,\infty}$

D. TOTAL TEMPERATURE RATIO,  $T_T/T_{T,\infty}$

FIGURE 39. TEMPORAL VARIATION OF FLOW QUANTITIES DURING UNSTART/RESTART

Figure 40 shows the comparison of calculated versus experimental results for the frequency response parameters of amplitude ratio and phase shift at various locations in the inlet and cold pipe. The calculations have been performed for three values of sinusoidal bypass area disturbance frequencies, namely 30, 50, and 100 hertz. Shock position amplitude ratio results indicate that the Program LAPIN shock movement is more heavily damped than experimentally observed; this is probably due to the neglect of viscous effects in the LAPIN inviscid-only treatment. A notable feature of the comparison is the extreme resonance in the 40-50 hertz range exhibited by both the experimental data and the inviscid calculations.

Calculated frequency response characteristics of the 40-60 inlet, with long cold pipe to upstream Mach number sinusoidal oscillations are presented in Fig. 41. The calculations have been performed at a frequency of 10 hertz. Calculated pressure response at various locations in the inlet are in excellent agreement with experiment, both for magnitude and phase. The experimental shock damping (amplitude ratio) is once again underpredicted.

#### 5.6 60-40 INLET

The NASA LeRC 60-40 inlet is an axisymmetric mixed-compression inlet with 60 percent of the effective supersonic area contraction occurring externally and 40 percent supersonic area contraction occurring internally at the design free-stream Mach number of 2.50. The external supersonic compression is accomplished via a biconic centerbody configuration. Details of the 60-40 inlet configuration are given in Fig. 42. The inlet was equipped with a translating centerbody, throat region cowl and centerbody bleed, and overboard bypass doors. Pertinent details concerning experimental investigations of this inlet conducted in the NASA LeRC 10- by 10-foot Supersonic Wind Tunnel are contained in Ref. 34 through 37.

ORIGINAL QUALITY  
OF POOR QUALITY

○ DATA (Ref. 32)

● PROGRAM LAPIN

— SMALL PERTURBATION THEORY (Ref. 4)

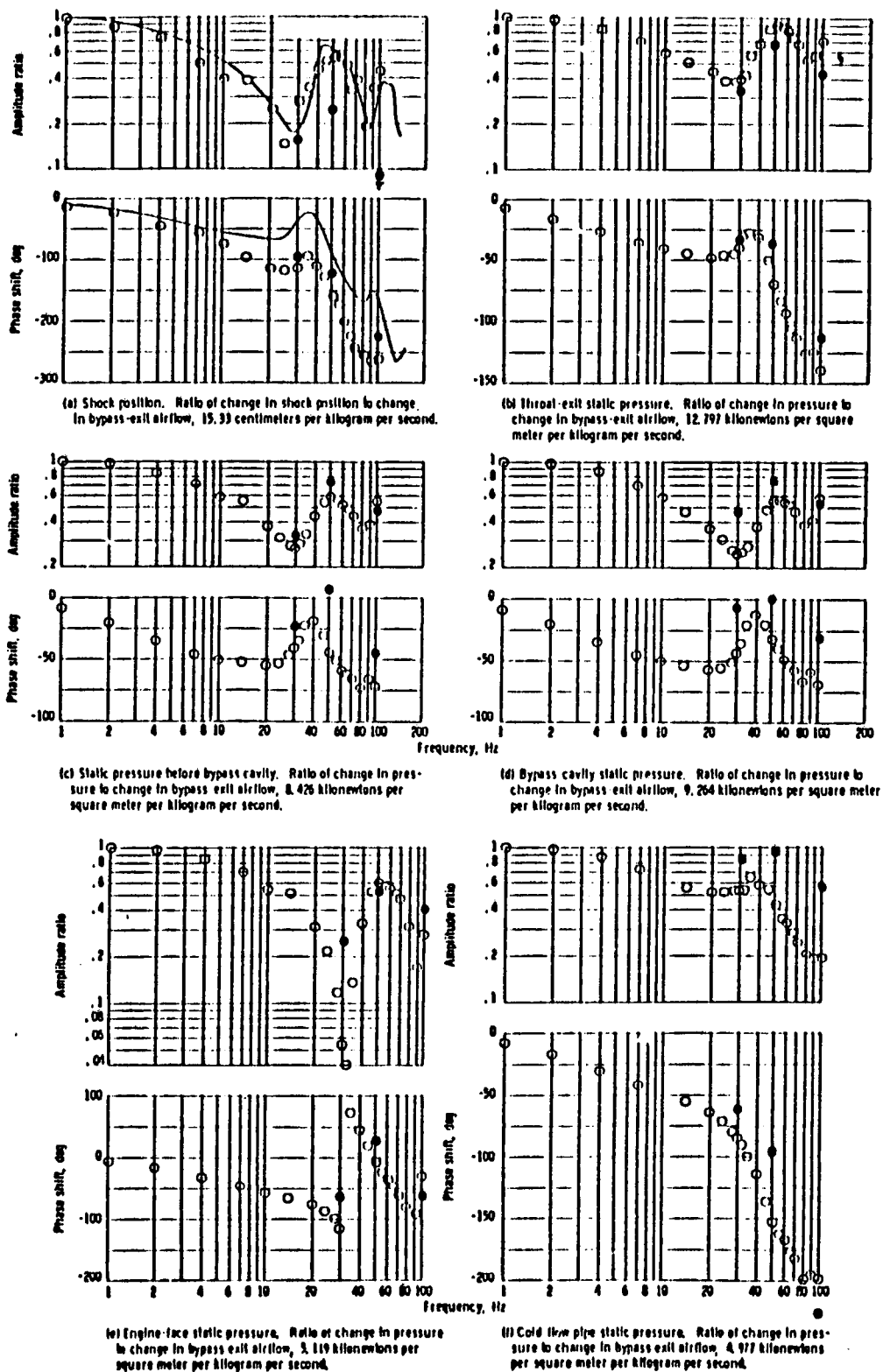
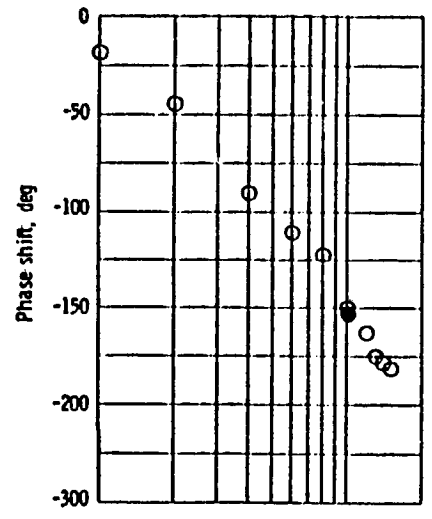
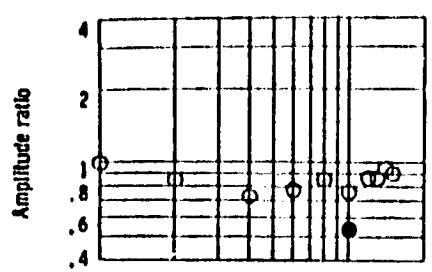
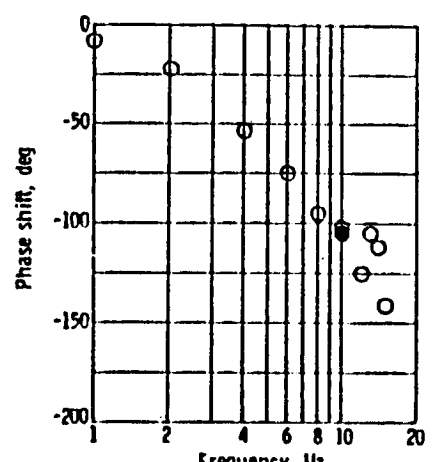
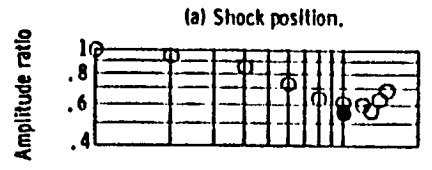


FIGURE 40. DYNAMIC RESPONSE OF INLET TO SYMMETRICAL INTERNAL DISTURBANCE



(a-2) Change in gust plate angle of attack,  $\pm \frac{1}{2}^\circ$ ; ratio of change in shock position to change in angle of attack, 7.7 centimeters per degree.

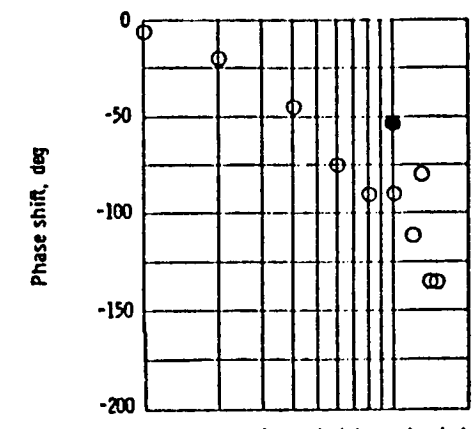
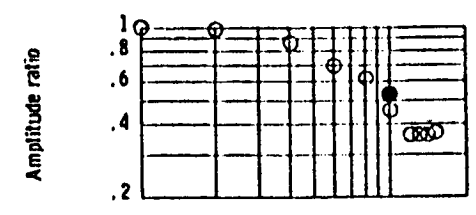


(b-2) Change in gust plate angle of attack,  $\pm \frac{1}{2}^\circ$ ; ratio of change in pressure to change in angle of attack, 2.872 kilonewtons per square meter per degree.

(a) Throat exit static pressure.

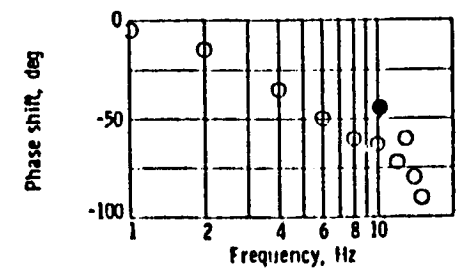
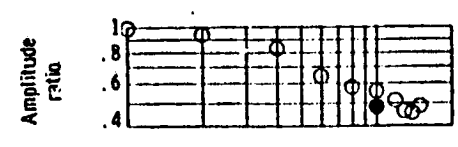
○ DATA (Ref. 32)  
● PROGRAM LAPIN

Change in Gust Plate Angle of Attack



(c-2) Change in gust plate angle of attack,  $\pm \frac{1}{2}^\circ$ ; ratio of change in pressure to change in angle of attack, 2.230 kilonewtons per square meter per degree.

(c) Bypass cavity static pressure.



(d-2) Change in gust plate angle of attack,  $\pm \frac{1}{2}^\circ$ ; ratio of change in pressure to change in angle of attack, 2.425 kilonewtons per square meter per degree.

(d) Engine face static pressure.

FIGURE 41. DYNAMIC RESPONSE OF INLET TO EXTERNAL DISTURBANCE



ORIGINAL DRAWING  
OF POOR QUALITY

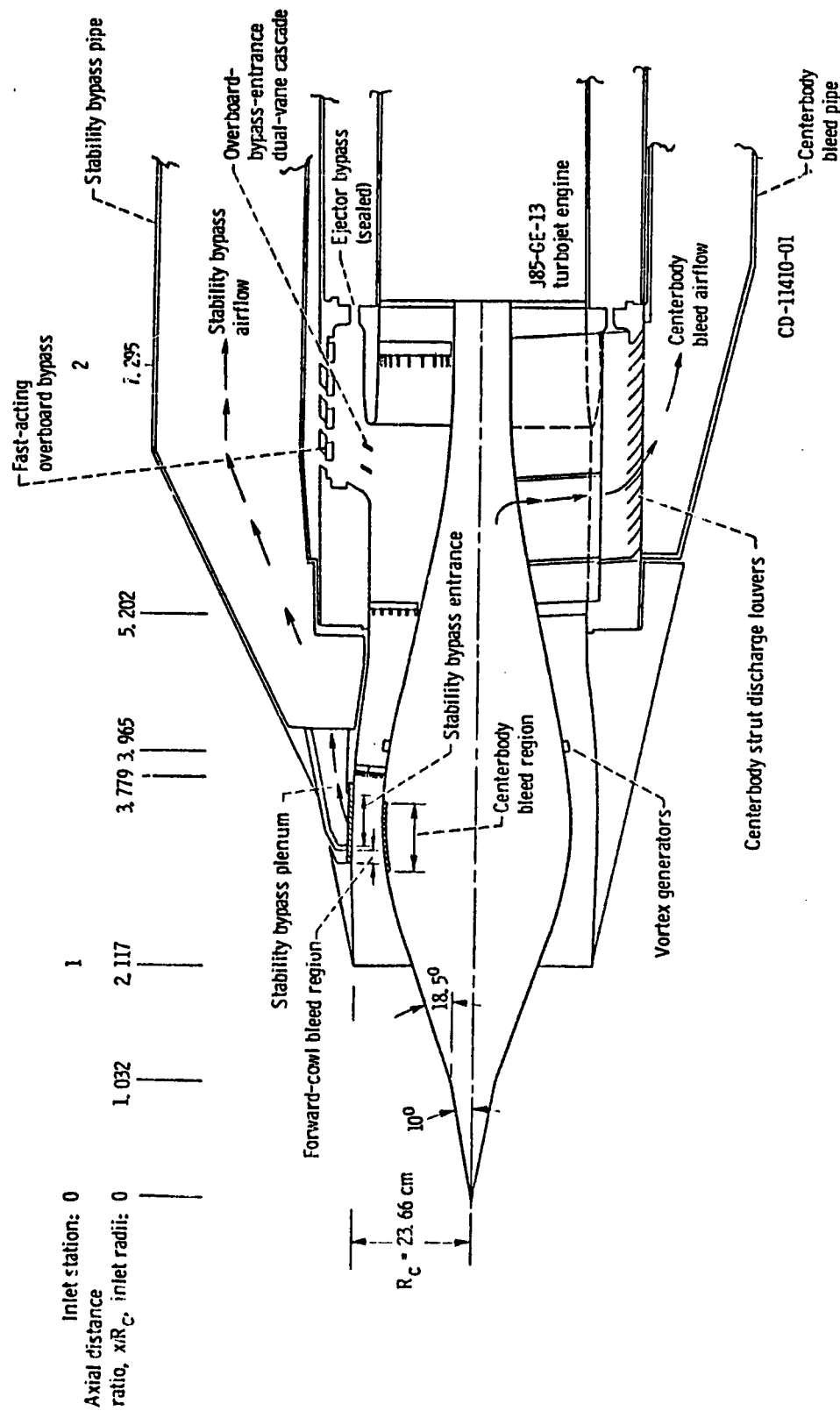


FIGURE 42. 60-40 INLET DETAILS

## 5.7 60-40 INLET STEADY-STATE PERFORMANCE

The present section will computationally examine the steady-state operation of the 60-40 axisymmetric mixed-compression inlet at a free-stream Mach number of 2.50. Experimental data for a porous bleed configuration reported in Ref. 37 will be used for comparison with calculated results. Details of the 60-40 inlet configuration have been previously given in Fig. 42.

Overall inlet performance in terms of total pressure recovery as a function of engine mass flow variation is shown in Fig. 43. The calculated total pressure recovery is in good agreement with the experimental data, both in distribution and magnitude. Also shown in Fig. 43 is the bleed plenum total pressure recovery as a function of throat bypass bleed mass flow ratio. The linear characteristics of bleed plenum total pressure recovery with respect to variation in throat bypass bleed mass flow is well predicted by the present inviscid bleed/bypass model.

Inlet static pressure distributions for various mass flow ratios are given in Fig. 44 for both the internal cowl and centerbody surfaces. As with the 40-60 inlet discussed previously, the calculated terminal normal shock is significantly downstream of the experimentally indicated location. As noted earlier, this discrepancy can be traced to the inviscid treatment of mass bleed effects without any allowance for viscous (boundary-layer) interaction. Irrespective of this, the calculated static pressure distribution is in excellent agreement with experiment in regions upstream of the bleed locations and downstream of the calculated terminal shock.

## 5.8 60-40 INLET TRANSIENT UNSTART LIMITS

Program LAPIN calculations of transient unstart limits for the 60-40 inlet with porous throat bypass were computed and compared to experimental data from Ref. 37. These results are shown in Fig. 45 for two bleed plenum volumes. It should be noted that the transient pulse was generated differently between experiment and simulation. During the experiment the bypass door opening was pulsed and then related to inlet corrected airflow through a steady-state correlation to obtain the stability index. In the case of the simulation, the corrected airflow

ORIGINAL  
OF POOR QUALITY

□ DATA (Ref. 37) FOR CONFIGURATION NF  
+ PROGRAM LAPIN

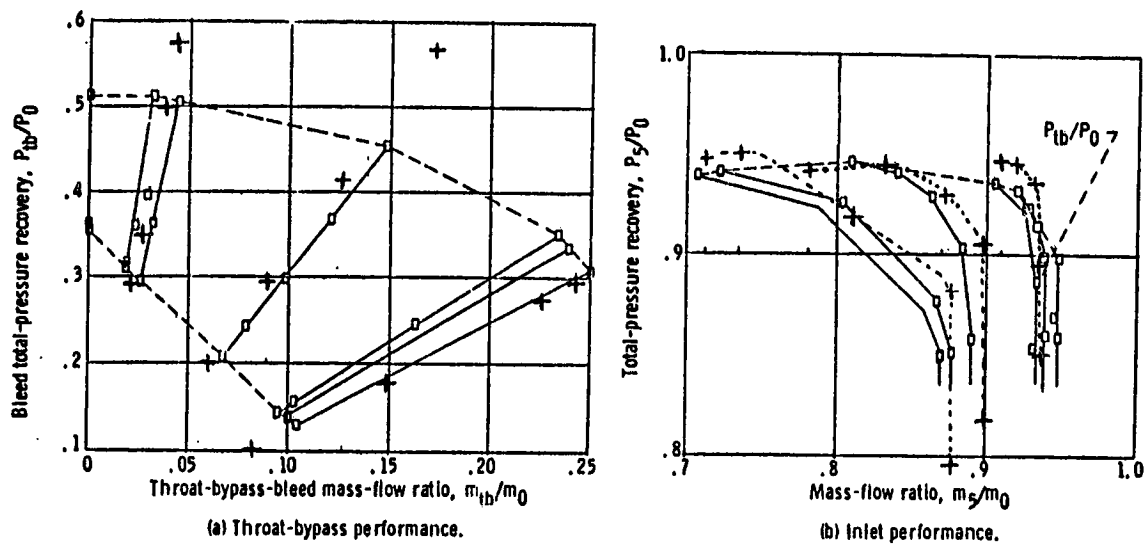


FIGURE 43. OVERALL PERFORMANCE OF THE 60-40 INLET WITH POROUS BLEED

# NASA L<sub>ERC</sub> 60 - 40 INLET

SYMBOLS DATA (Ref. 37)

..... PROGRAM LAPIN

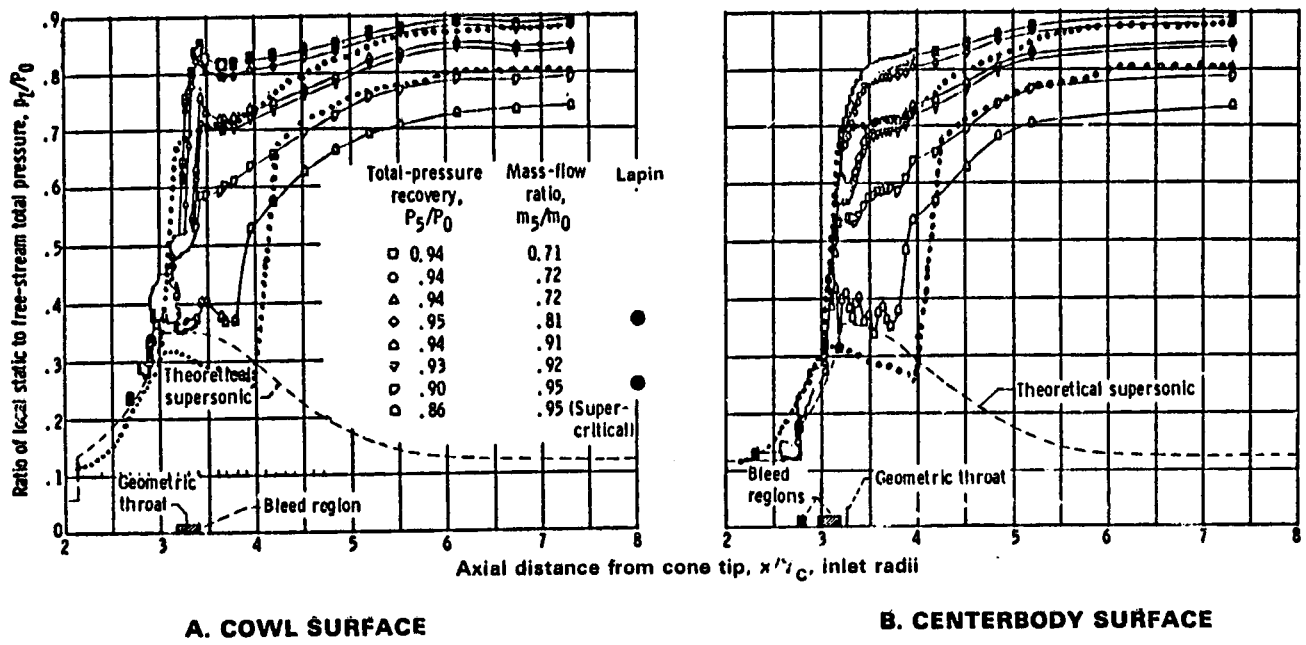


FIGURE 44. STATIC PRESSURE DISTRIBUTIONS

ORIGINAL PAPER  
OF POOR QUALITY

- ◆ DATA (Ref. 37) FOR CONFIGURATION NF  
● ◆ PROGRAM LAPIN

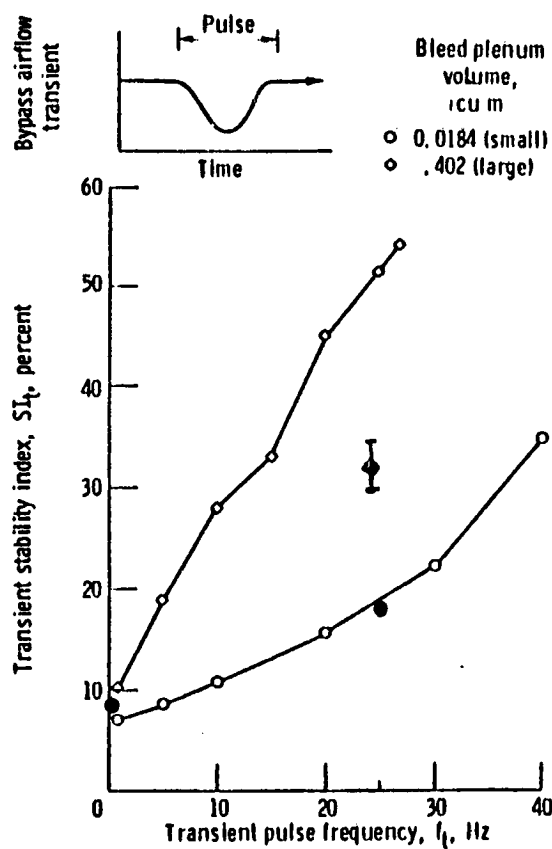


FIGURE 45. TRANSIENT UNSTART LIMITS  
WITH POROUS BLEED

was pulsed directly. Steady-state and low plenum volume results are in good agreement with experiment. The large plenum simulation is somewhat lower than experiment, with the difference suggesting that the transient pulse generation technique becomes more of a factor at the high airflow variations.

### 5.9 B-70 INLET

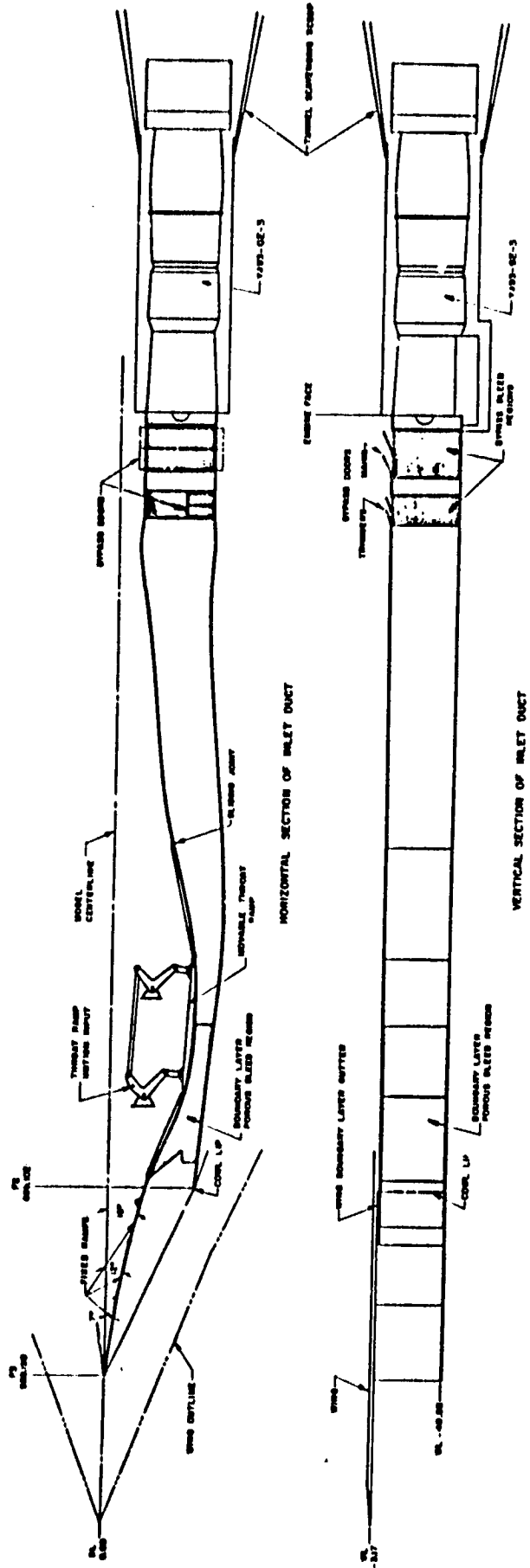
The B-70 inlet is a two-dimensional, external-internal compression inlet with bypass doors, variable throat area, throat bleed, and three external ramps. Details of the B-70 inlet are given in Fig. 46. Pertinent details concerning experimental investigation of this inlet in the AEDC 16-Foot Supersonic Wind Tunnel are given in Ref. 38.

### 5.10 B-70 INLET STEADY-STATE PERFORMANCE

The present section will computationally examine the steady-state operation of the B-70 two-dimensional inlet at a free-stream Mach number of 3.0. Experimental data reported in Ref. 38 will be used for comparison with calculated results. Details of the B-70 inlet configuration have been previously given in Fig. 46.

Figure 47 presents a comparison of the calculated steady-state static pressure distribution relative to experimental measurements. As can be seen, the experimental terminal normal shock is located in the throat region while the calculated normal shock is located downstream of the throat. In addition, the experimental pressure level is some 7% higher than the calculation downstream of the normal shock. These results are related in trend with the axisymmetric 40-60 inlet results reported earlier in this report and reflect the strong influence of viscous (boundary-layer) interaction effects in the throat region and downstream which are not accounted for in the present inviscid calculation.

ORIGINAL  
OF PHOTO COPY



NOTE: MODEL, MODELING STATIONS ARE IN INCHES

0.577 SCALE MODEL OF THE LEFT INLET, B-70

FIGURE 46. B-70 INLET GEOMETRY

B-70 INLET  $M_\infty = 3.0$

○ DATA (Ref. 38)

— PROGRAM LAPIN

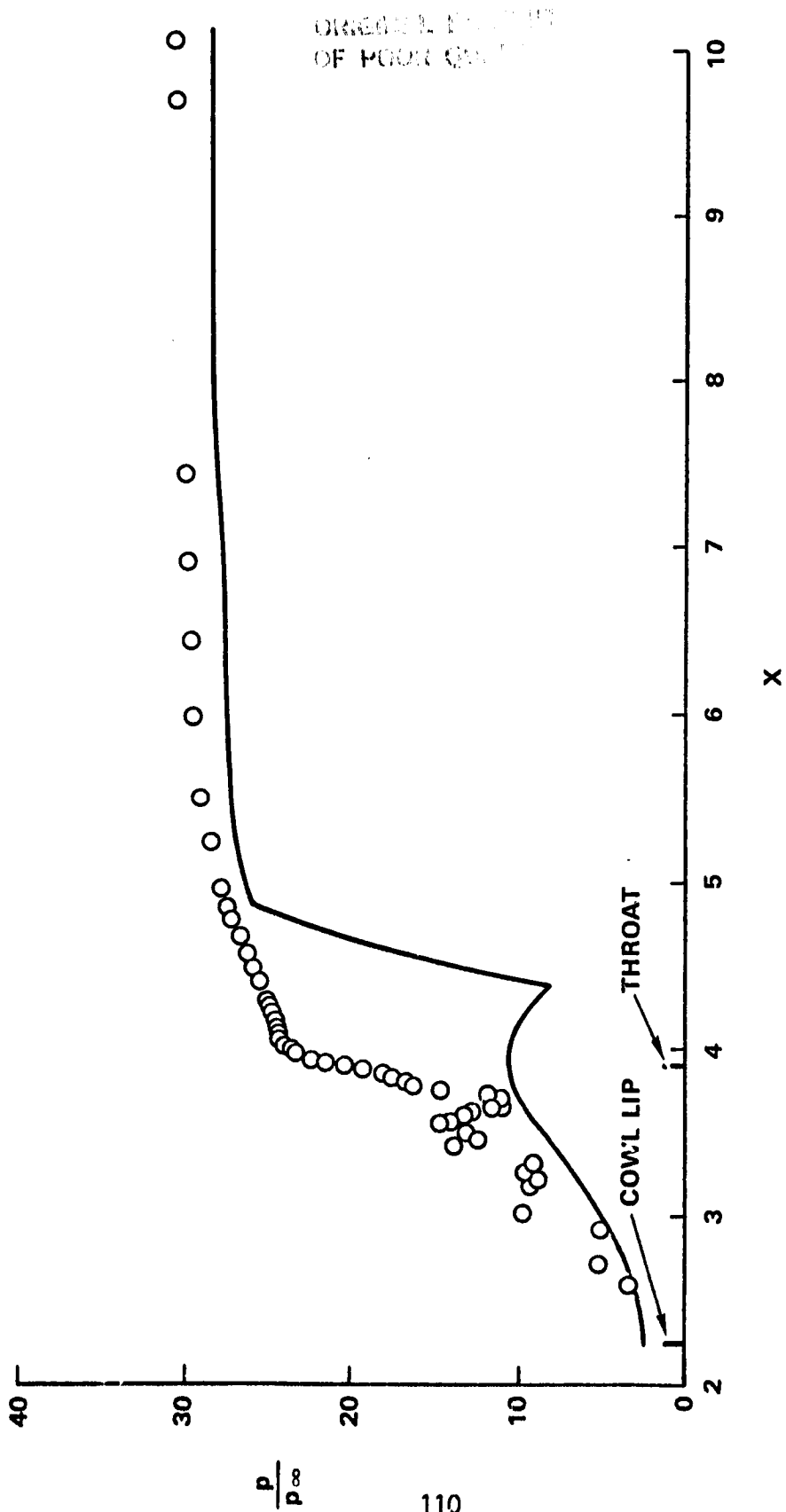


FIGURE 47. B-70 INLET STATIC PRESSURE DISTRIBUTION



## 6.0 CONCLUDING REMARKS

The results presented in this report indicate that the transient flow field in a supersonic mixed-compression inlet with large flow perturbations (hammershock, unstart/restart, etc.) can be reasonably well simulated via a quasi-one-dimensional inviscid approach using a shock capturing numerical solution algorithm. In order to further improve the applicability and accuracy of this approach, viscous boundary-layer effects and their interaction with the inviscid flow must be properly incorporated into the analysis.

Five different numerical algorithms have been utilized in the present work with a summary given in Table 2. For supersonic inlet applications with embedded moving shock waves, the split characteristics approach provides the highest fidelity numerical solution and is recommended for practical applications.

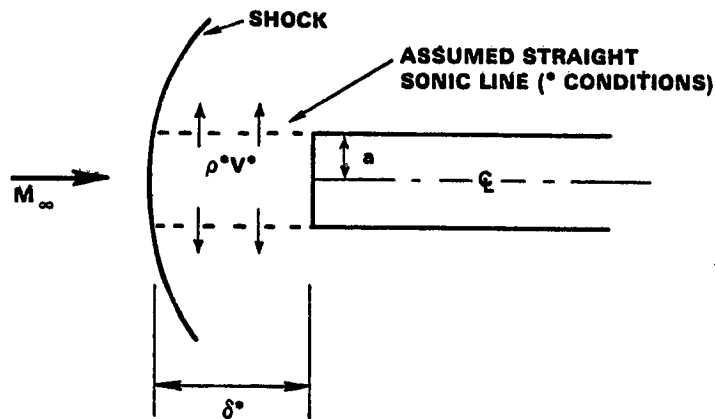
**TABLE 2  
NUMERICAL ALGORITHM SUMMARY**

METHOD	ALGORITHM TYPE	MAXIMUM COURANT NUMBER	DISSIPATION REQUIRED	RELATIVE* EXECUTION TIME	COMMENTS
EXPLICIT MacCORMACK	EXPLICIT	1	YES/NO	1	<ul style="list-style-type: none"> <li>• NO MATRIX INVERSION REQUIRED</li> <li>• EXTREMELY SIMPLE IN APPLICATION</li> <li>• NON-ROBUST FOR HAMMERSHOCK FLOWS</li> </ul>
BEAM WARMING	IMPLICIT	~3	YES	3	<ul style="list-style-type: none"> <li>• BLOCK TRI-DIAGONAL MATRIX INVERSION REQUIRED</li> <li>• RELATIVELY SIMPLE IN APPLICATION</li> <li>• NON-ROBUST FOR HAMMERSHOCK FLOWS</li> </ul>
HYBRID BEAM WARMING	IMPLICIT	~3	YES	3	<ul style="list-style-type: none"> <li>• BLOCK TRI-DIAGONAL MATRIX INVERSION REQUIRED</li> <li>• RELATIVELY SIMPLE IN APPLICATION</li> <li>• ROBUST FOR HAMMERSHOCK FLOWS</li> <li>• HAMMERSHOCK FLOWS CONTAIN SOLUTION NOISE</li> </ul>
SPLIT FLUX	IMPLICIT	~5	NO	4	<ul style="list-style-type: none"> <li>• BLOCK TRI-DIAGONAL MATRIX INVERSION REQUIRED</li> <li>• RELATIVELY DIFFICULT IN APPLICATION</li> <li>• ROBUST FOR HAMMERSHOCK FLOWS</li> <li>• CLEAN SOLUTIONS FOR ALL CLASSES OF FLOWS</li> <li>• COURANT NUMBERS UP TO 15 ARE POSSIBLE FOR SIMPLE FLOWS</li> </ul>
SPLIT CHARACTERISTICS	IMPLICIT	~10	NO	2	<ul style="list-style-type: none"> <li>• NO MATRIX INVERSION REQUIRED</li> <li>• RELATIVELY SIMPLE IN APPLICATION</li> <li>• ROBUST FOR HAMMERSHOCK FLOWS</li> <li>• HIGH FIDELITY SOLUTIONS FOR ALL FLOWS</li> <li>• COURANT NUMBERS UP TO 25 ARE POSSIBLE FOR SIMPLE FLOWS</li> </ul>

\*TOTAL CPU EXECUTION TIME RELATIVE TO EXPLICIT MacCORMACK METHOD

APPENDIX A  
Straight Sonic Line Correction Factor Derivation

Consider a two-dimensional (j=0) or axisymmetric (j=1) flat-faced body of half-height/radius a in a supersonic flow as shown below.

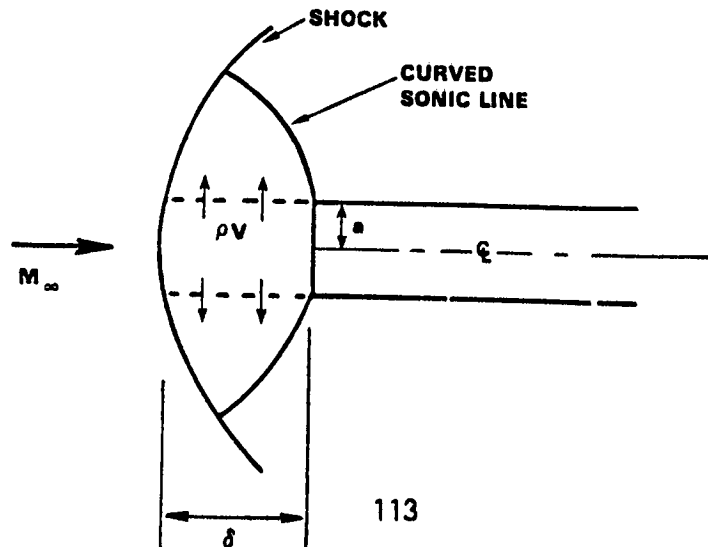


Under the assumption that the sonic line is straight as illustrated above, continuity considerations require that

$$\frac{\delta^*}{a} = \frac{1}{2j} \frac{\rho_\infty V_\infty}{\rho^* V^*} \quad (A-1)$$

where the \* indicates evaluation at sonic (M=1.0) conditions. The ratios  $\rho_\infty/\rho^*$  and  $V_\infty/V^*$  are easily determined from classical gasdynamics.

However, the actual sonic line is not straight but curved as shown below



Thus the actual flow crossing the dashed line is, in reality, not at sonic conditions and thus

$$\frac{\delta}{a} = \frac{1}{2} \frac{\rho_{\infty} V_{\infty}}{\rho V} \quad (\text{A-2})$$

where the mass flux  $\rho V$  crossing the dashed line is evaluated at the corresponding local conditions. Forming the ratio of Eq. (A-1) and (A-2) yields

$$\rho V = F \rho^* V^* \quad (\text{A-3})$$

where

$$F = \frac{\delta^*/a}{\delta/a} \quad (\text{A-4})$$

can be considered as a straight sonic line correction factor which, when multiplied by the corresponding straight sonic line mass flux  $\rho^* V^*$ , yields the actual mass flux  $\rho V$  crossing the dashed line shown above.

For a two-dimensional or axisymmetric flat-faced body in supersonic flow, the actual shock wave standoff distance  $\delta$  can be easily determined following Moeckel (Ref. 3) while the straight sonic line standoff distance  $\delta^*$  is given by Eq. (A-1). In this manner the straight sonic line correction factor  $F$  given by Eq. (A-4) becomes a function of free-stream Mach number only and is given in Fig. A-1 for both two-dimensional and axisymmetric bodies.

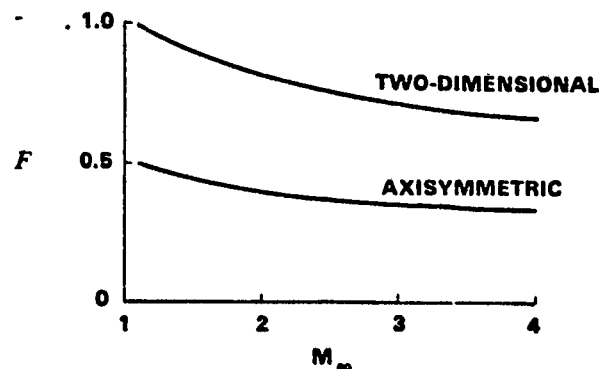
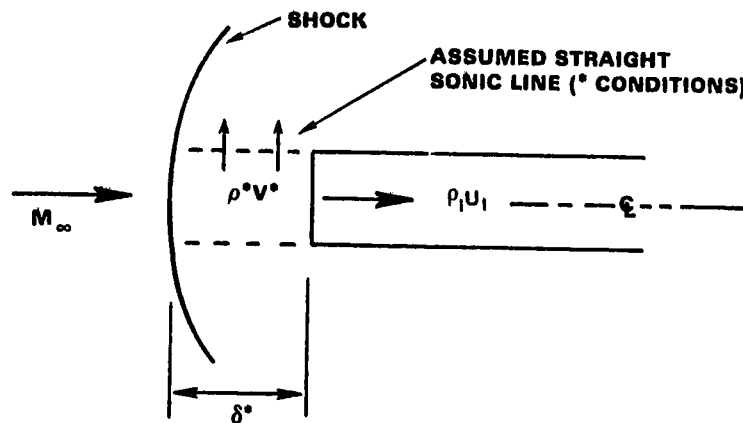


FIGURE A-1. STRAIGHT SONIC LINE CORRECTION FACTOR

ORIGINAL DOCUMENT  
OF POOR QUALITY

For the case of mass flow  $\rho_1 U_1$  into the flat-faced body as shown below



continuity considerations for the assumed straight sonic line require that

$$\frac{\delta^*}{a} = \frac{1}{2} \frac{\rho_\infty V_\infty}{\rho^* v^*} \left[ 1 - \frac{\rho_1 U_1}{\rho_\infty V_\infty} \right] \quad (\text{A-5})$$

In a similar manner for the actual flow crossing the dashed line

$$\frac{\delta}{a} = \frac{1}{2} \frac{\rho_\infty V_\infty}{\rho V} \left[ 1 - \frac{\rho_1 U_1}{\rho_\infty V_\infty} \right] \quad (\text{A-6})$$

Forming the ratio of Eq. (A-5) and (A-6) yields exactly the same results as Eq. (A-3) and (A-4) presented previously. The important point here is that the straight sonic line correction factor  $F$  is unaffected by mass flow through the body.

APPENDIX B  
SYMBOLS

A	Cross-sectional area; tridiagonal matrix coefficient
a	Speed of sound; body radius, geometry parameter in Fig. 7
B	Tridiagonal matrix coefficient
C	Tridiagonal matrix coefficient
$c_p$	Specific heat at constant pressure
$c_v$	Specific heat at constant volume
D	Diagonal matrix
d	Diagonal components of diagonal matrix
E	Total internal energy
e	Specific internal energy
F	Flux vector
$F_s$	Momentum equation source term
G	Right-hand-side vector
H	Total enthalpy
I	Identity matrix
J	Jacobian matrix
K	Flow coefficient
L	Length
M	Mach number
$M_s$	Continuity equation source term
p	Pressure
Q	Characteristic component; equivalent one-dimensional flux quantities
$Q_s$	Energy equation source term
R	Gas constant
r	Right-hand-side vector
S	Diagonalizing matrix
T	Temperature
t	Time
U	Solution vector
$U_p$	Primitive solution vector
$U_{ref}$	Reference velocity
u	Axial velocity
v	Velocity; normal velocity
v	volume

APPENDIX B  
SYMBOLS  
(continued)

$X, x$	Axial distance along centerline
$Y, y$	Normal distance from centerline
$Y_c$	Cowl radius
$\gamma$	Specific heat ratio
$\delta$	Shock stand-off distance
$\varepsilon$	Switching parameter
$\theta$	Local flow angle
$\Lambda$	Diagonalized Jacobian matrix
$\lambda$	Eigenvalue
$\xi$	Nondimensional axial distance
$\rho$	Density
$\tau$	Nondimensional time
$\psi$	Decomposition function; conical flow angle

Subscript

$c$	Cone surface
$C_p$	Conservative to primitive variables
$L$	Local
$p$	Plenum
$ref$	Reference
$s$	Shock
$T, O$	Total
$1, 2$	State ahead of and behind shock (scalar)
$1, 2, 3$	Mass, momentum, energy (vector)
$\infty$	Free-stream

Superscript

*	Sonic; known constraint value
+	Positive characteristic value
-	Negative characteristic value
~	Dimensional variable; Runge-Kutta predictor value
$\hat{\phantom{x}}$	Nondimensional variable; factored solution variable
$\vec{\phantom{x}}$	Vector quantity

APPENDIX B  
SYMBOLS  
(concluded)

Mathematical Operators

- |            |  |
|------------|--|
| $\nabla$   | Backward difference spatial operator         |
| $\Delta$   | Forward difference spatial operator          |
| $\delta^4$ | Fourth-order dissipation difference operator |



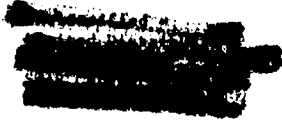
## REFERENCES

1. Martin, A. W., "Propulsion System Dynamic Simulation Theory and Equations," NASA CR-928, March 1968.
2. Amin, N. F. and Hall, G. R., "Supersonic Inlet Investigation. Volume II. Air Induction System Dynamic Simulation Model," AFFDL-TR-71-121, Volume II, September 1971.
3. Moeckel, W. E., "Approximate Method for Predicting Form and Location of Detached Shock Waves Ahead of Plane or Axially Symmetric Bodies," NACA TN 1921, July 1949.
4. Willoh, R. G., "A Mathematical Analysis of Supersonic Inlet Dynamics," NASA TN D-4969, December 1968.
5. Wasserbauer, J. F. and Willoh, R. G., "Experimental and Analytical Investigation of the Dynamic Response of a Supersonic Mixed-Compression Inlet," NASA TM X-52441, 1968. See also AIAA Paper No. 68-651 presented at the AIAA 4th Propulsion Joint Specialist Conference, Cleveland, Ohio, June 1968.
6. Cole, G. L. and Willoh, R. G., "Analysis of the Dynamic Response of a Supersonic Inlet to Flow-Field Perturbations Upstream of the Normal Shock," NASA TN D-7839, January 1975.
7. Mays, R. A., "Inlet Dynamics and Compressor Surge," AIAA Paper No. 69-484 presented at the AIAA 5th Propulsion Joint Specialist Conference, U.S. Air Force Academy, Colorado, June 9-13, 1969. See also *Journal of Aircraft*, Volume 8, No. 4, April 1971, pp. 219-226.
8. Shapiro, A. H., *The Dynamics and Thermodynamics of Compressible Fluid Flow*, The Ronald Press Company, New York, 1954.
9. Zucrow, M. J. and Hoffman, J. D., *Gas Dynamics*, John Wiley and Sons, New York, 1977.
10. Anderson, D. A. and Rai, M. M., "The Use of Solution Adaptive Grids - in Solving Partial Differential Equations," *Numerical Grid Generation*, J. F. Thompson, Editor, Elsevier Science Publishing Company, Inc., 1982, pp. 317-338.
11. Beam, R. M. and Warming, R. F., "An Implicit Finite Difference Algorithm for Hyperbolic Systems in Conservation Law Form," *Journal of Computational Physics*, Volume 22, 1976, pp. 87-110.
12. Warming, R. F. and Beam, R. M., "On the Construction and Application of Implicit Factored Schemes for Conservation Laws," *SIAM-AMS Proceedings*, Volume 11, Symposium on Computational Fluid Dynamics, New York, April 16-17, 1977.

13. Thomas, P. D. and Lombard, C. K., "The Geometric Conservation Law - A Link Between Finite-Difference and Finite-Volume Methods of Flow Computation on Moving Grids," AIAA Paper 78-1208 presented at AIAA 11th Fluid and Plasma Dynamics Conference, Seattle, Washington, July 10-12, 1978.
14. Steger, Joseph L. and Warming, R. F., "Flux Vector Splitting of the Inviscid Gas Dynamic Equations with Application to Finite Difference Methods," NASA TM 78605, July 1979.
15. Reklis, R. P. and Thomas, P. D., "Shock Capturing Algorithm for the Navier Stokes Equations," AIAA Journal, Volume 20, No. 9, September 1982, pp. 1212-1218.
16. MacCormack, R. W., "The Effect of Viscosity in Hypervelocity Impact Cratering," AIAA Paper 69-354, Cincinnati, Ohio, 1969.
17. MacCormack, R. W., "A Numerical Method for Solving the Equations of Compressible Viscous Flow," AIAA Paper 81-0110 presented at the 19th Aerospace Sciences Meeting, St. Louis, Missouri, January 12-15, 1981.
18. Roe, P. L., "Approximate Riemann Solvers, Parameter Vectors, and Difference Schemes," Journal of Computational Physics, Volume 43, 1981, pp. 357-372.
19. White, M. E., "The Application of MacCormack's New Implicit Scheme to the Solution of Quasi-One-Dimensional Fluid Flows," Master of Science Thesis, University of Maryland, 1981. See also AIAA Paper 82-0992 presented at the AIAA/ASME 3rd Joint Thermophysics, Fluids, Plasma, and Heat Transfer Conference, St. Louis, Missouri, June 7-11, 1982.
20. Dennard, J. S., "A Transonic Investigation of the Mass-Flow and Pressure Recovery Characteristics of Several Types of Auxiliary Air Inlets," NACA RM L57B07, April 1957.
21. Syberg, J. and Hickcox, T. E., "Design of a Bleed System for a Mach 3.5 Inlet," NASA CR-2187, January 1973.
22. Rasmussen, M. L., "On Hypersonic Flow Past an Unyawed Cone," AIAA Journal, Volume 5, No. 8, August 1967, pp. 1495-1497.
23. Wittliff, C. E., "Correlation of Drag Coefficients for Sharp Cones," AIAA Journal, Volume 6, No. 7, July 1968, pp. 1430-1431.
24. Maslen, S. H., "Inviscid Hypersonic Flow Past Smooth Symmetric Bodies," AIAA Journal, Volume 2, No. 6, June 1964, pp. 1055-1061.
25. Hayes, W. D. and Probstein, R. F., Hypersonic Flow Theory, Academic Press, New York, 1959.

26. Inouye, M., Rakich, J. V., and Lomax, H., "A Description of Numerical Methods and Computer Programs for Two-Dimensional and Axisymmetric Flow Over Blunt-Nosed and Flared Bodies," NASA TN D-2970, August 1965.
27. Hall, N. A., Thermodynamics of Fluid Flow, Prentice-Hall, Inc., New York, 1951.
28. Owczarek, J. A., Fundamentals of Gas Dynamics, International Textbook Company, Scranton, Pennsylvania, 1964.
29. Cole, G. L., Neiner, G. H., and Crosby, M. J., "An Automatic Restart Control System for an Axisymmetric Mixed-Compression Inlet," NASA TN D-5590, December 1969.
30. Cubbison, R. W., Meleason, E. T., and Johnson, D. F., "Effect of Porous Bleed in a High-Performance Axisymmetric, Mixed-Compression Inlet at Mach 2.50," NASA TM X-1692, November 1968.
31. Cubbison, R. W., Meleason, E. T., and Johnson, D. F., "Performance Characteristics from Mach 2.58 to 1.98 of an Axisymmetric Mixed-Compression Inlet System With 60 Percent Internal Contraction," NASA TM X-1739, February 1969.
32. Wasserbauer, J. F., "Dynamic Responses of a Mach 2.5 Axisymmetric Inlet With Engine or Cold Pipe and Utilizing 60 Percent Supersonic Internal Area Contraction," NASA TN D-5338, July 1969.
33. Choby, D. A., Burstadt, P. L., and Calogeras, J. E., "Unstart and Stall Interactions Between a Turbojet Engine and an Axisymmetric Inlet With 60-Percent Internal-Area Contraction," NASA TM X-2192, March 1971.
34. Choby, D. A., "Tolerance of Mach 2.50 Axisymmetric Mixed-Compression Inlets to Upstream Flow Variations," NASA TM X-2433, January 1972.
35. Sanders, B. W. and Mitchell, G. A., "Increasing the Stable Operating Range of a Mach 2.5 Inlet," AIAA Paper No. 70-686 presented at the AIAA 6th Propulsion Joint Specialist Conference, San Diego, California, June 15-19, 1970. See also NASA TM X-52799, 1970.
36. Wasserbauer, J. F. and Choby, D. A., "Performance of a Biconic Inlet Designed for Mach 2.5 With Internal Distributed Compression and 40-Percent Internal Contraction," NASA TM X-2416, February 1972.
37. Sanders, B. W. and Mitchell, G. A., "Throat-Bypass Bleed Systems for Increasing the Stable Airflow Range of a Mach 2.50 Axisymmetric Inlet With 40-Percent Internal Contraction," NASA TM X-2779, May 1973.

38. Lowry, J. F. and Prunty, C. C., "Documentation of Wind Tunnel Data from the 0.577-Scale B-70 Inlet-Engine (YJ93-GE-3) Compatibility Test," AEDC-TDR-63-54, April 1963.

1. Report No. NASA CR 174676		2. Government Accession No.		3. Recipient's Catalog No.	
4. Title and Subtitle LARGE PERTURBATION FLOW FIELD ANALYSIS AND SIMULATION FOR SUPERSONIC INLETS FINAL REPORT				5. Report Date September 1984	
				6. Performing Organization Code	
7. Author(s) M.O. Varner, W.R. Martindale, W.J. Phares, K.R. Kneile, and J.C. Adams, Jr.				8. Performing Organization Report No.	
9. Performing Organization Name and Address Sverdrup Technology, Inc. 600 William Northern Blvd. Tullahoma, Tennessee 37388				10. Work Unit No.	
				11. Contract or Grant No. NAS3-23682	
12. Sponsoring Agency Name and Address National Aeronautics and Space Administration Washington, D.C. 20546				13. Type of Report and Period Covered Contractor Report	
				14. Sponsoring Agency Code 505-43-42	
15. Supplementary Notes Project Manager, Gary L. Cole, Aerodynamics and Engine Systems Division, NASA Lewis Research Center, Cleveland, Ohio					
16. Abstract An analysis technique for simulation of supersonic mixed-compression inlets with large flow field perturbations (hammershock, unstart/restart, etc.) is presented. The approach is based upon a quasi-one-dimensional inviscid unsteady formulation which includes engineering models of unstart/restart, bleed, bypass, and geometry effects. Numerical solution of the governing time-dependent equations of motion is accomplished through a shock-capturing finite-difference algorithm, of which five separate approaches are evaluated. Comparison with experimental supersonic wind tunnel data is presented to verify the present approach for a wide range of transient inlet flow conditions.					
17. Key Words (Suggested by Author(s)) Supersonic Inlets One Dimensional Flow Inviscid Flow Computational Fluid Dynamics Finite Difference Theory			18. Distribution Statement 		
19. Security Classif. (of this report) Unclassified		20. Security Classif. (of this page) Unclassified		21. No. of Pages 123	22. Price*